



POLITECNICO MILANO 1863

SCUOLA DI INGEGNERIA INDUSTRIALE E
DELL'INFORMAZIONE

Laurea Magistrale in ingegneria meccanica

Topological design, experimental characterization and
elasto-plastic modelling of micro-lattice structures for
orthopaedic implants

Supervisor: Prof. Stefano Foletti
Co-supervisor: Ing. Matteo Gavazzoni

Maurizio Zoia
899376

Academic year 2018/2019

Abstract

A literary review on micro-lattice structures for the design of orthopedic implants has been performed and two parameters, i.e. Young modulus (E) and pore size (p) (defined as the diameter of the biggest inscribed sphere inside the lattice domain) have been found crucial to avoid stress shielding the former and to promote bone ingrowth and vascularization the latter. Design intervals of those variables has been defined to ensure the above-mentioned properties (300-4000 MPa for ' E ' and 500-1000 μm for ' p ') and 3D printed via SLM using Ti6Al4V powder.

Among seven initial unit cell geometries, two of them (Diamond and Tetrahedron) have been selected on the basis of the overmentioned constraints on ' E ' and ' p '. For the numerical estimation of the elastic modulus, a homogenized approach has been used and proper PBC (Periodic Boundary Conditions) have been imposed to the boundary of a periodic micro-lattice unit volume representative of the infinite homogenized mean. Different ways to apply PBC has been studied for symmetric and non-symmetric structures. A Matlab code has been developed to calculate pore size of ideal and real geometry reconstructed from CT scan.

Static compression and tension tests have been conducted and the homogenized stress vs strain curves have been obtained with the aid of DIC (Digital Image Correlation). CT scans have been performed in order to evaluate the differences between real and ideal geometry.

Numerical elasto-plastic simulations under compression loading condition have been realized either on the ideal and real structures and the values of Young modulus, yield stress and pore size have been estimated and compared with experimental data. An attempt to substitute solid with beam elements thus saving computational time and enabling the modelling of big structures has been performed; even if it resulted promising, several open questions have been left for future developments.

A strong relationship has been observed between relative density and printing quality on one side and mechanical properties on the other side. With reference to Tetrahedron topology, an important deviation between as-designed and as-manufactured Young modulus and yield stress (nearly 50 %) is present because of poor geometry other than lower relative density (16.6 % ideal vs 14.5 % real). Nevertheless, real values of ' E ' and ' p ' of both cells shape still fall within the interval defined by the constraints relevant for the biomedical application.

With reference to the numerical compressive simulations, a difference, caused by boundary effects, between the elastic modulus of the periodic unit with PBC and the structures composed by a finite number of cells (like the models of the specimens) has been assessed and quantified for both cell topologies as a function of the cross-sectional area. These boundary effects are mainly due to the presence of free surfaces at the boundary of the specimens.

Regarding the non-linear regime, Buckling has been observed on Tetrahedron in compression tests; the same behavior has been predicted by numerical analysis. The observation, already present in literature, that one periodic unit cell with PBC is not enough to represent the infinite mean in non-linear regime in case of buckling has been confirmed. No buckling phenomena has been observed for Diamond cell.

Sommaro

Una ricerca legata all'applicazione di strutture micro-lattice finalizzata alla progettazione di protesi ossee è stata realizzata in letteratura e due parametri, ovvero modulo elastico (E) e dimensione di poro (p) sono risultati cruciali per evitare l'intorpidimento osseo il primo e per promuovere vascolarizzazione e ricrescita ossea il secondo. Gli intervalli di progettazione per garantire tali proprietà sono stati definiti (300-4000 MPa for ' E ' and 500-1000 μm for ' p ').

Partendo da sette celle unitarie candidate, due di loro (Tetraedro e Diamante) sono state selezionate sulla base della migliore compatibilità con ' E ' e ' p ' e stampate in 3D con la tecnica SLM usando polvere di Titanio Ti6Al4V.

Per la stima numerica del modulo elastico, un approccio di omogeneizzazione è stato applicato e opportune condizioni al contorno periodiche sono state imposte all'interfaccia di un volume unitario di micro-lattice in modo tale che esso sia rappresentativo del mezzo omogeneo infinito. Differenti modalità di applicazione delle PBC sono state studiate su strutture simmetriche e non. Un codice Matlab è stato sviluppato per calcolare la dimensione di poro sia della geometria ideale sia di quella reale ricostruita a partire dalla tomografia.

Test sperimentali a trazione e compressione sono stati condotti e le curve sforzi-deformazioni omogeneizzate sono state misurate tramite la tecnica DIC (Digital Image Correlation). Inoltre, le immagini tomografate sono state acquisite per valutare le differenze tra geometria reale ed ideale. Simulazioni numeriche con modello elasto-plastico sono state realizzate sia sulle strutture reali sia su quelle ricostruite a partire dalla tomografia e i valori di modulo elastico, dimensione di poro e carico di snervamento sono stati stimati e confrontati con i dati sperimentali. Un approccio per sostituire gli elementi solidi con i beam nei modelli ad elementi finiti è stato implementato per favorire la modellazione di geometrie computazionalmente onerose; sebbene esso sia promettente, diversi sono i punti aperti lasciati a sviluppi futuri.

Una forte dipendenza fra densità relativa e qualità di stampa da una parte e proprietà meccaniche dall'altra è stata osservata. Con riferimento alla geometria tetraedrica, un'importante differenza tra modulo elastico e snervamento reali ed ideali è presente (50 % circa) a causa di una non perfetta riuscita di stampa oltre che alla differenza delle densità relative (16.6 % ideale contro 14.5 % ideale). Ciononostante, i valori reali di modulo elastico e dimensione di poro di entrambe le geometrie rispettano ancora i vincoli rilevanti in ambito biomedico.

Con riferimento alle simulazioni numeriche, una differenza, causata da effetti di bordo, tra i moduli elastici della cella singola con PBC e di strutture composte da un numero finito di celle (come i modelli dei provini) è stata stimata e quantificata per entrambe le geometrie come funzione della dimensione di sezione. Tali effetti di bordo sono dovuti alla presenza di superfici libere alla periferia dei provini.

Per quanto riguarda il regime non lineare, la deformazione di tipo buckling è stata osservata sulla struttura tetraedrica nei test di compressione; lo stesso comportamento è stato previsto anche dalle analisi numeriche. In linea con studi precedenti, si è confermato che una singola unità periodica non è sufficiente per rappresentare il mezzo omogeneo infinito in campo non lineare in presenza di buckling. Nessun cedimento di tipo buckling è stato osservato sulla cella Diamante.

Table of content

List of figures.....	9
List of tables.....	11
1. Introduction.....	13
1.1 State of the art.....	13
1.1.1 Properties of bone.....	13
1.1.2 Brief historical remarks of orthopaedic implants and main features.....	15
1.1.3 Stress shielding and vascularisation.....	15
1.1.4 Micro-lattice unit cell geometries.....	17
1.1.5 Experimental characterisation of micro-lattice structures.....	18
1.1.6 Numerical characterisation of micro-lattice structures.....	19
2. Design and identification of micro-lattice topology for biomedical application .	23
2.1 CAD design and pore size computation.....	24
2.2 Young modulus evaluation.....	28
2.2.1 Periodic boundary conditions for symmetric structures.....	29
2.2.2 General Periodic boundary conditions.....	31
2.3 Results and selection of candidate structures to be printed.....	34
3. Compression and tension experimental tests on micro-lattice specimens.....	41
3.1 Geometry and preparation of testing specimens.....	41
3.1.1 Compression specimens.....	41
3.1.2 Tension specimens.....	42
3.2 Mechanical testing: set-up, measurement method and procedure.....	44
3.3 Results.....	45
3.3.1 Diamond.....	47
3.3.2 Tetrahedron.....	51
4. Numerical elastic and elasto-plastic analysis on ideal selected structures.....	57
3D Beam elements.....	58
Tetrahedral solid elements.....	58
4.1 Linear regime.....	59
4.1.1 Tetrahedron.....	59
4.1.2 Diamond.....	63
4.2 Non-linear regime.....	65
4.2.1 Tetrahedron.....	65
4.2.2 Diamond.....	67
5. Analysis of the real geometry.....	69
5.1 Real morphological properties.....	69
5.2 Real elasto-plastic mechanical properties.....	72
5.2.1 Tetrahedron.....	72
5.2.2 Diamond.....	74
6. Conclusions and future developments.....	77
Bibliography.....	79

List of figures

Figure 1-1: Cortical and cancellous bone	14
Figure 1-2: pore size image [5]	16
Figure 1-3: dense-in and dense-out scaffold configurations [10]	16
Figure 1-4: multilayer cylindrical scaffolds [6].....	17
Figure 1-5: examples of “sheet-based” TPMS cells (left) and “strut-based” cells (right)	17
Figure 1-6: Grasping solution for a tensile specimen; (a) is the initial configuration, (b) the modified configuration with varying density and (c) the resulting failure correctly far from the grasps [14].	18
Figure 1-7: Failure mode of BCC uniform (a), (b) and functionally graded (d), (e) micro-lattice scaffold [10]	19
Figure 1-8: Octet Truss (left) and Tetrahedron (right) cells [5].....	19
Figure 1-9: Example of design spaces realised by [17]; (a) for TET and (b) for Octet truss	20
Figure 1-10: structures compared in the work of [8].....	20
Figure 1-11: Rhombic dodecahedron (a) and diagonal (b) cells [12]	20
Figure 1-12: Example of bifurcation due to different buckling deformation modes	21
Figure 2-1: example of cubic cell: strut diameter (d) and strut length (L) are independent parameters..	23
Figure 2-2: the seven unit cell shapes taken for the initial step of design; in order: (a) dodecahedron, (b) diamond, (c) BCC, (d) tetrahedron, (e) FCC, (f) H45, (g) octet truss.	24
Figure 2-3: 2x2x2 base unit for FCC (a) and Tetrahedron (b)	24
Figure 2-4: Code lines to import slices and arrange the 3D voxel matrix.....	26
Figure 2-5: example of how the Matlab function ‘bwdist’ works: (a) is the input matrix and (b) is the output	26
Figure 2-6: Code lines for the generation of the sphere inside mat2	27
Figure 2-7: Visual output of the algorithm	28
Figure 2-8: comparison between close-cell configuration (a) and open-cell configuration (b) on a BCC cell	29
Figure 2-9: candidate structures with "open-strut" configuration	29
Figure 2-10: Reference cube.....	30
Figure 2-11: symmetric BC applied to a BCC structure taken as example.....	30
Figure 2-12: sets for the equation constraints: (a) shows the master node, (b1) all the slaves node; (b2) is a focus to see the missing node among the slaves	31
Figure 2-13: deformed shape of BCC and displacements in x-y (a) – (b) and x-z (c) planes	31
Figure 2-14: 2D example of the constraints applied by Homtools.....	32
Figure 2-15: Constraints and imposed displacement for general PBC.....	33
Figure 2-16: representation of the candidate structures on the E vs p chart.....	35
Figure 2-17: Linear regression of λ vs ϕ for Tetrahedron.....	36
Figure 2-18: Linear regression of λ vs E for Tetrahedron	36
Figure 2-19: Linear regression of λ vs ϕ for Diamond	37
Figure 2-20: Linear regression of λ vs E for Tetrahedron	37
Figure 2-21: Design area for Tetrahedron.....	38
Figure 2-22: Design area for Diamond	39
Figure 2-23: Loading direction for tetrahedron structure	40
Figure 3-1: Base units for building test specimens: TET (a) and Diamond (b)	41
Figure 3-2: Ideal compression specimens: DIA (a) and TET (b).....	42
Figure 3-3: Ideal tension specimens: DIA (a) and TET (b).	43
Figure 3-4: Real specimens: (a) Diamond compression, (b) Diamond tension, (c) TET compression, (d) TET tension.....	43
Figure 3-5: Set-up of the testing machine: (a) for compression, (b) for tension	44
Figure 3-6: Example of initial non-linear trend of compressive homogenised stress vs strain curve	45
Figure 3-7: Positioning of every strain gauge. (a) compressive Diamond; (b) tensile Diamond; (c) compressive TET; (d) tensile TET	46
Figure 3-8: homogenised average stress strain curves of diamond for each compressive test.....	47
Figure 3-9: Trend of Young modulus in compression for strain gauge from left to right.....	47
Figure 3-10: homogenised average stress strain curves of diamond for each tensile test.....	48

Figure 3-11: Trend of Young modulus in tension for strain gauge from left to right.....	48
Figure 3-12: Comparison between tensile and compressive tests: left (a) average Young modulus and right (b) average yield stress and UTS	49
Figure 3-13: Average tension and compression Diamond curves.....	50
Figure 3-14: compressive deformation of Diamond: (a) is the undeformed shape, (b) the deformed shape.....	50
Figure 3-15: tensile deformation of Diamond: (a) is the undeformed shape, (b) the deformed shape	51
Figure 3-16: Tensile homogenised average stress vs strain curves of TET	51
Figure 3-17: Trend of TET Young modulus in tension for strain gauge from left to right	52
Figure 3-18: tensile deformation of TET: (a) is the undeformed shape, (b) the deformed shape. The red area highlights the defected struts.	53
Figure 3-19: homogenised average stress strain curves of TET for each compressive test.....	53
Figure 3-20: Trend of TET Young modulus in compression for strain gauge from left to right.....	54
Figure 3-21: UCS and σ_y for TET compressive tests	54
Figure 3-22: compressive deformation of TET: (a) is the undeformed shape, (b) the deformed shape	55
Figure 4-1: Monotonic curve for data extrapolation [21]	57
Figure 4-2: Scheme of DOF of a 3D linear beam element.....	58
Figure 4-3: Ten node tetrahedral element	58
Figure 4-4: Picture of the 1/8 solid specimen for FE analysis.....	59
Figure 4-5: TET specimen with beam elements	60
Figure 4-6: Tetrahedron 2x2x2 RVE with beam elements	61
Figure 4-7: Specimen section of increasing dimensions: (a) 4x4, (b) 6x6, (c) 8x8, (d) 10x10, (e) 12x12 ...	62
Figure 4-8: Young modulus behaviour with increasing TET specimen section	62
Figure 4-9: Mistake in the coupling of Diamond structure with Homtools.....	63
Figure 4-10: Ideal Diamond specimens of different section dimensions: (a) 3x3, (b) 4x4, (c) 6x6 and (d) 7x7	64
Figure 4-11: Young modulus behaviour with increasing Diamond specimen section	64
Figure 4-12: TET specimen undergoes buckling; (a) with solid elements, (b) with beam elements	66
Figure 4-13: Different deformed TET shape between PBC for symmetric structures (a) and general PBC (b)	66
Figure 4-14: Effect of the RVE size on the non-linear part of TET homogenised stress vs strain curve	66
Figure 4-15: Comparison between general PBC and PBC for symmetric structures	67
Figure 4-16: Effect of the RVE size on the non-linear part of Diamond homogenised stress vs strain curve	68
Figure 4-17: Deformed shape of Diamond 1x (a), 2x (b) and 3x (c) periodic	68
Figure 5-1: Selected unit cells for real pore size computation from the complete section of TET (a) and Diamond (b).....	70
Figure 5-2: Tomography detail of TET compression specimen	71
Figure 5-3: Tomography detail of Diamond compression specimen	71
Figure 5-4: From the PNG (a) to the STL (b) of real TET.....	72
Figure 5-5: Real reconstructed TET 2x2x2 periodic unit.....	73
Figure 5-6: Numerical homogenised stress vs strain curve of the reconstructed real TET 2x2x2 RVE compared with compressive tests, ideal 2x2x2 RVE and ideal 1/8 compression specimen.....	74
Figure 5-7: Real reconstructed Diamond 'reduced' 7x7x7 specimen	74
Figure 5-8: Comparison between experimental compression Diamond with RVE and reconstructed 7x7x7 reduced specimen	75
Figure 6-1: Resume of the values of Young modulus and Pore size.....	77

List of tables

Table 1: properties of cortical bone.....	14
Table 2: properties of cancellous bone	14
Table 3: geometric properties of the candidate micro-lattice subjected to pore size and Young modulus analysis	25
Table 4: Results of the preliminary analysis	34
Table 5: Regression parameters for Tetrahedron	37
Table 6: Regression parameters of Diamond.....	38
Table 7: Design parameters for printing session.....	39
Table 8: Ideal relative density for compression specimens.....	42
Table 9: load path of compression tests.....	45
Table 10: load path of tension tests	45
Table 11: Resume of experimental values of Diamond averaged between each strain gauge.....	49
Table 12: Resume of experimental values averaged between each strain gauge of TET.....	55
Table 13: Monotonic mechanical properties of annealed Ti6Al4V	57
Table 14: Boundary effect on TET modelled with beams.....	62
Table 15: Boundary effect on Diamond modelled with solids	65
Table 16: Real relative density for compression specimens	69
Table 17: comparison between ideal and real morphological properties of TET and Diamond RVE.....	70
Table 18: Resume of TET results.....	73
Table 19: Resume of Diamond results	75

1. Introduction

The thesis work hereafter presented regards the topological and mechanical study of micro-lattice structures obtained by SLM (Selective Laser Melting) and made of Ti6Al4V for severely damaged bone replacement and it has been developed at the mechanical department of Politecnico di Milano in cooperation with Prof. Nima Shamsaei of Auburn university Alabama. The objective of this thesis work is to establish a starting point for the application of competences and experience of the research group of a mechanical department about the mechanical assessment of micro-lattice e structures to the biomedical field in order to design orthopaedic implants for the substitution of severely damaged bones. To this extent, this work is divided into two main parts: the first part comprises chapter 1 and chapter 2, the second part is composed by chapter 3, 4 and 5.

The aim of the first part is to carry out a literary review about the state of the art of the use of micro-lattice scaffold in biomedical field and understand which parameters are needed to make the implant suitable for bone substitution and which solutions have been figured out so far. What is more, in the first part, the problem of the pore size computation by means of a home-made code is fronted as well as the way PBC must be imposed to a small periodic unit to represent the homogenised infinite lattice mean for symmetric and non-symmetric geometries. The ultimate objective of the first part is to design suitable periodic unit cells lattice geometries suitable for the overmentioned biomedical application and perform the 3D printing of compression and tension specimens.

In the second part, compression and tension experiments for mechanical characterisation are carried out as well as the CT scans of compression samples for the analysis of real relative density and FE reconstruction of the real geometries. To understand how and if the specimen is able to predict the Young modulus of the homogenised infinite mean numerical models are established. Moreover, the study of how many periodic unit are needed to obtain an RVE (Representative volume element) of the infinite lattice either in linear and non-linear regime is made. Finally, numerical values of Young modulus, yield stress and pore size are computed on ideal and real reconstructed structures and compared with experiments.

1.1 State of the art

1.1.1 Properties of bone

Human bone has a hierarchical structure which goes from the macroscale to the sub-nanoscale. Although each level of such hierarchy performs important functions, it is purpose of this work to limit the attention to the macroscale, the same one of the orthopaedic implant.

At such level, a distinction between cortical or compact bone and cancellous or trabecular bone is made as it can be seen in Figure 1-1

Cortical bone is stiffer and is in charge of carrying loads, it stands at the periphery of the structure, it is highly anisotropic possessing higher mechanical properties in longitudinal rather than transversal direction, better in compression than tension [1].

Cancellous bone fills the inner part, it has high porosity and performs important biological functions since it contains bone marrow where red blood cells are produced[1].

As far as mechanical and geometrical properties go, values are affected mainly by bone type (for instance tibia is stiffer than femur) and age [2]. Below, some general ranges are shown according to [2] either for cortical (Table 1) and cancellous bone (Table 2):

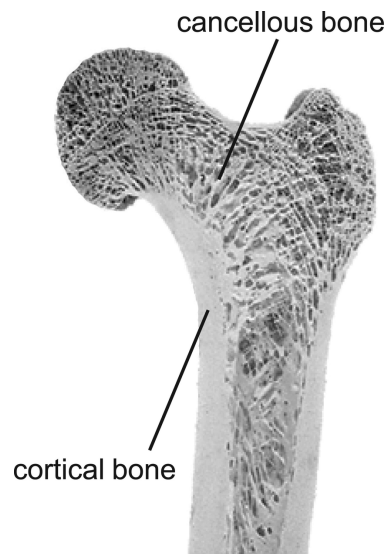


Figure 1-1: Cortical and cancellous bone

Cortical bone

E	15-28	GPa
Tensile YS	100-140	MPa
UTS	68-170	MPa
UCS	179-213	MPa
Density	$\cong 1.85$	$\frac{\text{g}}{\text{cm}^3}$
Porosity	3-5	%

Table 1: properties of cortical bone

Cancellous bone

E	0.02-0.83	GPa
Tensile YS	-	-
UTS	-	-
UCS	2.2-10.6	MPa
Density	$\cong 0.3$	$\frac{\text{g}}{\text{cm}^3}$
Porosity	50-90	%

Table 2: properties of cancellous bone

1.1.2 Brief historical remarks of orthopaedic implants and main features

The history of orthopaedic implants dates back to China around 2000 BCE with bamboo pegs to replace missing teeth and 1000 BCE in Egyptian society with similar pegs made by copper [3]. Looking to more recent years, in 1985, thanks to the discovery of antiseptics and X-ray radiology, metal implants and screws started to appear and between 1936-1950 bio-compatible solution such as Co-based and Ti-based were developed [3]. Today, most of the commercially available prosthesis for bone replacement are still made of full metal and, even if this is good from the load-bearing and durability point of view (component life up to 25 years[3]), they cannot achieve some important features which were recently pointed out, and that micro-lattice implants manufactured by 3D printing are able to.

The technical aspects that must be met by modern prosthesis can be summarized according to [4] in the following four points:

1. Form: scaffold should completely fill the bone defect cavity.
2. Function: scaffold needs to provide load-bearing properties.
3. Fixation: scaffold must provide an adequate interface and interconnection to the surrounding bone.
4. Formation: scaffold should promote new bone formation.

Whereas points 1 and 2 are already addressed also by full metal solutions, point 3 and 4 represent the new challenge of modern research.

Fixation can be achieved by avoiding the phenomenon of stress shielding, by means of an implant's Young Modulus lower or equal to the one of real bone.

Formation instead, means to promote a biological activity in terms of vascularisation and bone tissue regeneration and it is enhanced by providing a certain porosity and pore size to the implant.

1.1.3 Stress shielding and vascularisation

Stress shielding involves bone resorption and bone density reduction caused by a drop of the usual level of stress which human tissue is normally subjected to and can bring to the failure of the implant. Said phenomenon occurs, for example, in full metal prosthesis since they carry most of the load leaving human bone in a condition of decreased physiologic loading. Common full metal implants like Co-Cr-Mo or Ti6Al4V have a stiffness of 210 GPa and 110 GPa respectively, much higher than the one of human bone [3] thus causing this type of problem (see Table 1 and Table 2 for human bone properties). Because elastic properties of micro-lattice scaffolds are much lower than the one of the original material from which they are made, they are a successful solution to the problem.

On the other end, formation within the prosthesis is agreed to be a crucial function to be addressed. Vascularization and cell seeding would reconstruct new bone all around and through the implant so that it acts as a bridge for new bone tissue generation.

Pore size and porosity are the two geometrical parameters to select in order to make such biological activity successful [5], [6].

Porosity is defined as one minus the ratio between the volume of the real unit (V_u) cell and the one of a cube having the same unit length (V_{cube}):

$$P^* = \left(1 - \frac{V_u}{V_{cube}}\right) 100$$

Pore size is the radius of the largest inscribed sphere into the lattice medium [5]. (Figure 1-2)

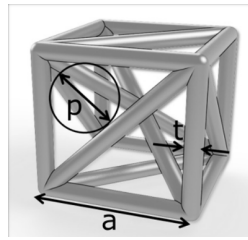


Figure 1-2: pore size image [5]

Several methods can be found in literature to measure pore size:

Bobbert et al. [7] acquired images from a real lattice specimen with micro-CT scanner, 2D slices of the structure were reconstructed using the software Analyse 11.0 and finally the Fiji plugin Bonj was used for 3D computation of morphological features (pore size was determined by means of the “thickness” option). A similar approach is adopted in [8] where the software VGstudiomax is adopted. A slightly different possibility is based on the development of an algorithm acting on voxel images and capable of measuring pore size as described in [9].

According to [5] porosity over 50 % and pore size between 50 and 800 μm are required, similar values are also suggested by [6] (pore size between 100 and 900 μm). In the work of Du Plessis [8] micro-lattice structures with different geometry of the unit cell were investigated and structures with dual pore size like the octet are considered to be interesting since big pores enhance vascularization and small pores enhance cell seeding. What is more, another important feature associated to pore size is its progressively increase/reduction from the core out to the periphery of the prosthesis (the so called dense-in or dense-out configuration Figure 1-3). Ezgi Onal et al. [10] discovered, out of in vitro test on BCC porous scaffolds, that a varying dense-in pore size is more beneficial for cell seeding and proliferation than dense-out porosity; as a matter of fact, after 7 days of test, the dense-out structure started to occlude vascularization which develops from outside to inside.

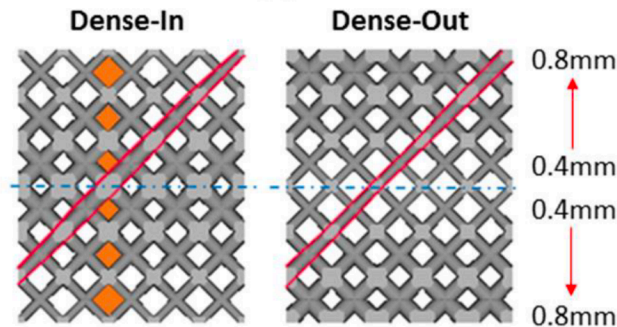


Figure 1-3: dense-in and dense-out scaffold configurations [10]

The work of [6] proposes, instead, cylindrical multilayer configurations with increasing pore size from the external to the internal (Figure 1-4) in order to mimic the structure of real bone (especially for long bones like femur); the stress strain curves in the post-plateau region show a lower degree of fluctuations resulting in a higher ductility and higher capacity to absorb energy which is beneficial for orthopaedic applications.

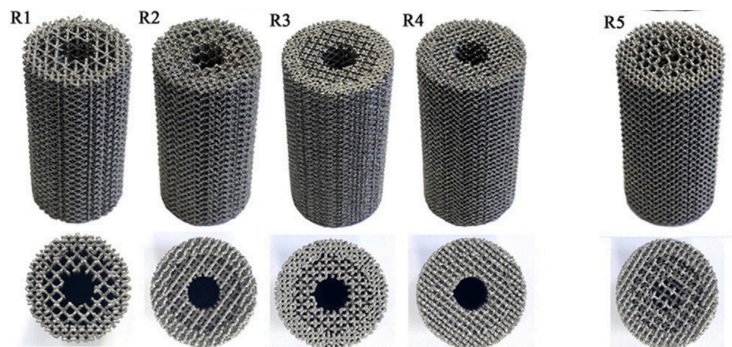


Figure 1-4: multilayer cylindric scaffolds [6]

To obtain porous structures with such a small value of pore size and such a complex internal shape, conventional manufacturing techniques cannot be applied, and additive manufacturing is the only solution up to date.

Two similar 3D printing procedures are mainly used: Selective Laser melting (SLM) and Electron beam melting (EBM) because of their good controllability and higher precision if compared to other fabrication methods like direct deposition and three-dimensional printing [11]. Both technologies progressively build up the component layer by layer through the melting and consequent solidification of metallic powder which is added at each step; while the former provides energy from a laser, the latter employs a high-energy beam of electrons.

Some of the disadvantages and issues of AM are related to the energy and time consumption (a 3D printing session is still quite slow and unsuitable for mass production), to the surface quality and the need of performing some post processing and to the dependency of the mechanical properties with the printing direction.

1.1.4 Micro-lattice unit cell geometries

A lattice structure is made by a subsequent repetition, either by a mirror or a pattern, of a single periodic unit cell, namely a 3D structure of any shape contained inside a cube of a certain side length “L”. As far as design goes, an important distinction can be made between two different ways of conceiving a cell: the so called “strut-based” and “sheet-based” configurations (Figure 1-5). The former is composed by a combination of beam-like structures called struts all connected to each other, the latter is featured by a smooth and continuous attachment of sheets of material. Among sheet-based solutions, triply based minimal surfaces, (TBMS) (minimal surfaces with “translational symmetries in three independent directions”) [7] are the most utilised ones.

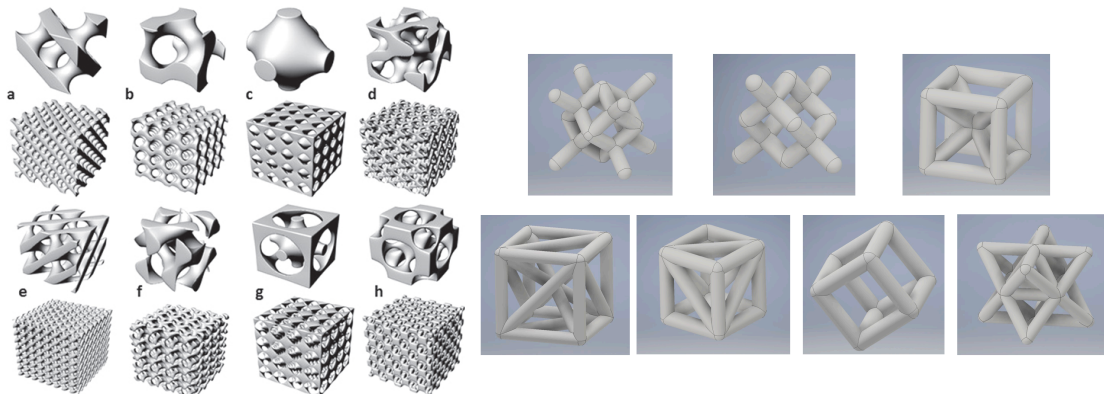


Figure 1-5: examples of “sheet-based” TPMS cells (left) and “strut-based” cells (right)

Several different geometries and dimensions are proposed in literature leading to a quite wide variety of possible solutions to be selected for design. An exhaustive state of the art review summary about static compressive mechanical properties of various strut-based geometries is reported by [2]. The key aspect to meet is the contemporary cohesion of mechanical properties, cell seeding and vascularization and manufacturability, all of them being controlled by contrasting variables; for instance, to an increase of strength, that can be obtained by choosing higher dimensions of struts, follows a decrease of pore size and porosity which might be detrimental for cell seeding and might bring about manufacturing issues. Regarding the matching of mechanical properties with human bone, the approach is not univocal in the sense that either the correspondence with cortical or cancellous bone properties or a halfway compromise can be found in literature. To make an example, the structures studied in the work of [12] emulates cortical bone while in the work of [7] results are more close to trabecular bone.

Although sheet-based lattice seems promising for biomedical application, they owns more issues from the manufacturing point of view because of their small thickness and continuously changing orientation which involves the need of much more support material [7].

Talking about strut-based structures, two relevant families can be defined according to their deformation behaviour: bending-dominated and stretch-dominated.

Bending-dominated possess struts which tend to bend under compressive loading resulting in shear failure whereas stretch-dominated are stiffer and fail in a layer-by-layer mechanism. According to the Maxwell criterion [13] the following rule is suggested to make a prior distinction among the two:

$$\text{Being: } M = b - 3j + 6$$

b = number of struts of the cell;

j = number of joints of the cell;

if $M < 0$ the structure is bending-dominated

if $M \cong 0$ the structure is stretch-dominated

if $M > 0$ the structure is over rigid

A stretch-dominated structure is generally preferred since it is able to better distribute the load.

1.1.5 Experimental characterisation of micro-lattice structures

The analysis of mechanical properties is carried out either by experimental tests and FE numerical simulations. All the references that will be cited make use of Ti6Al4V that is a common material employed for bone replacement thank to its biocompatibility. The compressive test is the most common one; up to date, tensile tests are not diffused due to the problem of designing a proper gripping on the specimen that prevents localised failure near the gripping itself, a possible solution is proposed by [14] where struts own increasing density close to the grasps so to increase the stiffness of that area and enhance failure at the middle of the sample as shown in Figure 1-6.

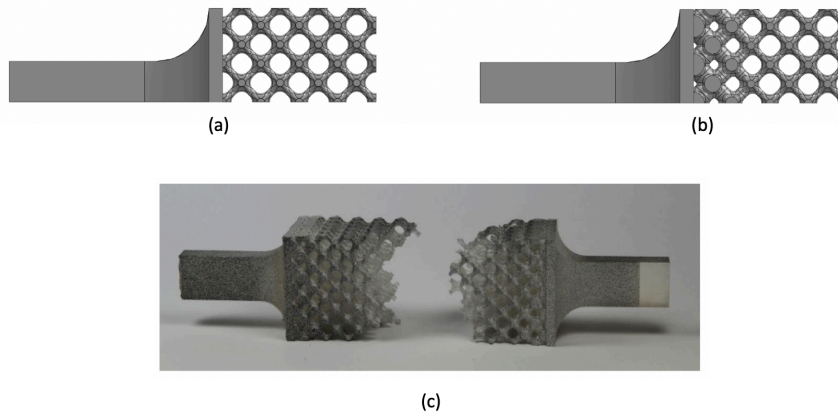


Figure 1-6: Grasping solution for a tensile specimen; (a) is the initial configuration, (b) the modified configuration with varying density and (c) the resulting failure correctly far from the grasps [14]

In general, tests on metamaterials are more difficult to be performed than for conventional ones since no extensometers can be put and the use of DIC (Digital Image Correlation) to map strains is suggested. An example of compression test set up which makes use of DIC is discussed in the work of Fei Liu et al. [15] on Diamond structures of varying struts diameter and fillet radius between each strut. For the obtainment of the stress vs strain curve, a homogenised approach has been adopted, namely the load has been divided times the cross-section area (the one of a square) and the displacement times the vertical length of the specimen. A similar method for compression tests has been implemented by Ezgi Onal et al. [10], in this case uniform and functionally graded BCC structures with varying densities and have been tested featuring the uniform micro-lattice a 45 band failure and the functionally graded a layer-by-layer crush initiating at the weakest struts (Figure 1-7).

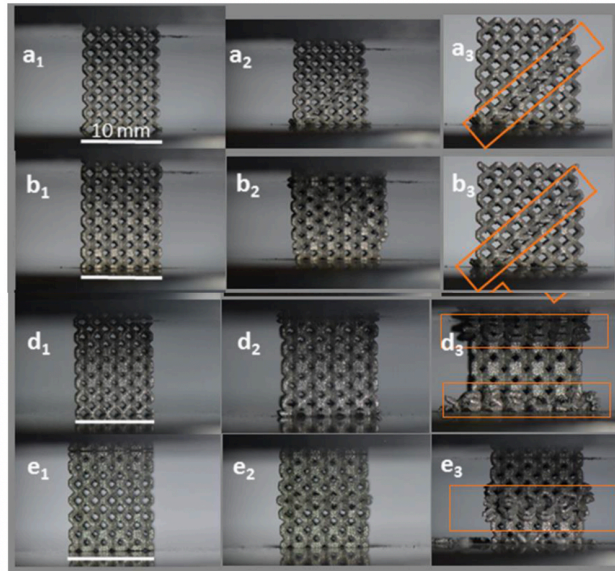


Figure 1-7: Failure mode of BCC uniform (a), (b) and functionally graded (d), (e) micro-lattice scaffold [10]

As far as fatigue properties go, S. Amin Yavary et al. [16] investigated the fatigue properties of diamond, cube and truncated cuboctahedron micro-lattice finding a correlation between porosity and fatigue strength (the higher is porosity, the poorer is fatigue response) as well as the matching, for each cell type, of the normalised fatigue curves for different porosities respect to the yield stress of a single curve suggesting therefore a direct dependency between static and fatigue properties. Talking about TBMS, according to [7], four TPMS (primitive, I-WP, gyroid and diamond) have been printed via SLM to carry out either fatigue and static compressive tests. Results show Young Modulus in the range of trabecular bone (3.8–6.4 GPa) and good fatigue properties for the I-WP, gyroid and diamond structures (shapes are shown in Figure 1-10) with life up to 7×10^5 cycles.

1.1.6 Numerical characterisation of micro-lattice structures

The comparison between experimental and numerical properties is sometimes present, and it is extremely important since it establishes and validates models that can easily and rapidly predict the behaviour of the real component. In two subsequent papers edited by Pasini et al. [5], [17] two strut-based structures namely Tetrahedron and Octet truss are investigated (Figure 1-8). A particular effort is devoted to the realisation of design maps able to correlate and compare Young modulus, yield stress, strut thickness, porosity and pore size of as-design and as-manufactured lattice, showing the relative errors of each overmentioned variable between the real and the ideal cell; those design maps are reported in Figure 1-9. The numerical models established make use of AH (asymptotic homogenisation), which replaces the micro-lattice with a representative full solid volume, to get the elastic properties (E) and, a reduced volume respect to the real specimens, to obtain yield stress with elasto-plastic material properties. The results are such that as-manufactured mechanical properties are lower than as-designed one owing to the former's lower relative density.

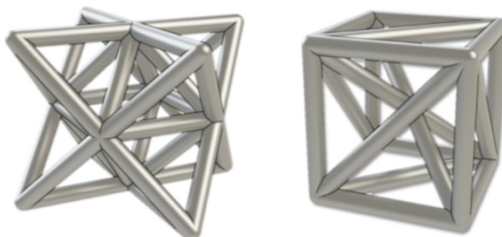


Figure 1-8: Octet Truss (left) and Tetrahedron (right) cells [5]

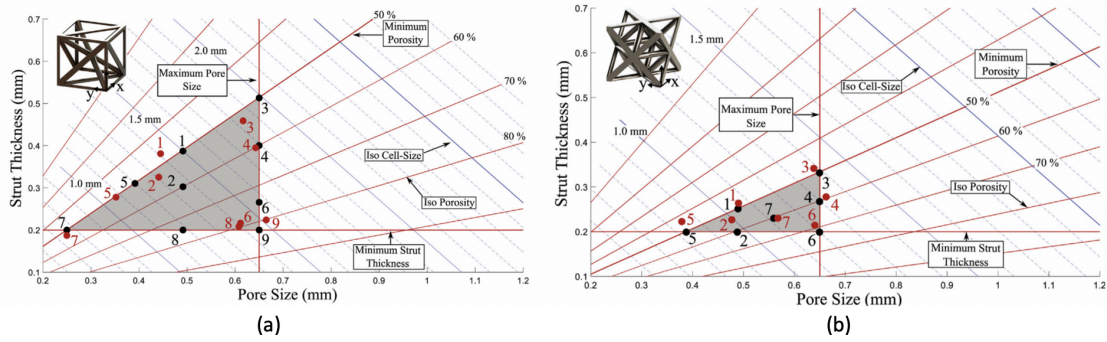


Figure 1-9: Example of design spaces realised by [17]; (a) for TET and (b) for Octet truss

In the work of Du Plessis et al. [8], strut-based and TBMS sheet-based structures are compared from a numerical point of view, with static compressive simulations (Figure 1-10) involving linear elastic models. Being the linear elastic model not excessively expensive from a computational point of view, the entire lattice specimen is modelled. The most relevant conclusion is that TPMS structures have lower value of Von Mises stress and so they can distribute better the load without relevant stress concentration regions: this could suggest also a longer fatigue life than strut-based systems.


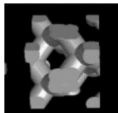
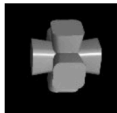

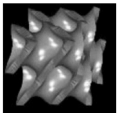
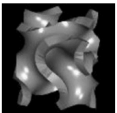
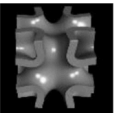
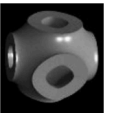
	Strut-based design			Minimal surface design				
	Rhombic dodecahedron	Diamond	G-struct	Octet	Diamond	Gyroid	I-WP	Primitive
								
		D-sb	G-sb	O-sb	D-ms	G-ms	I-ms	P-ms
Porosity, %		61	63	62	62	63	65	62
Strut/Sheet thickness, μm		491	651	288	157	188	152	250

Figure 1-10: structures compared in the work of [8]

Moving to strut-based scaffolds, a different work of Du Plessis [12] performs numerical static compressive tests on diagonal and rhombic dodecahedron lattice samples of 5x5x5 cubes (Figure 1-11). Once again simulations are linear elastic and performed on the entire specimen with the aim of computing the elastic modulus and locations of localised stress. Results show a good matching with cortical bone Young Modulus.

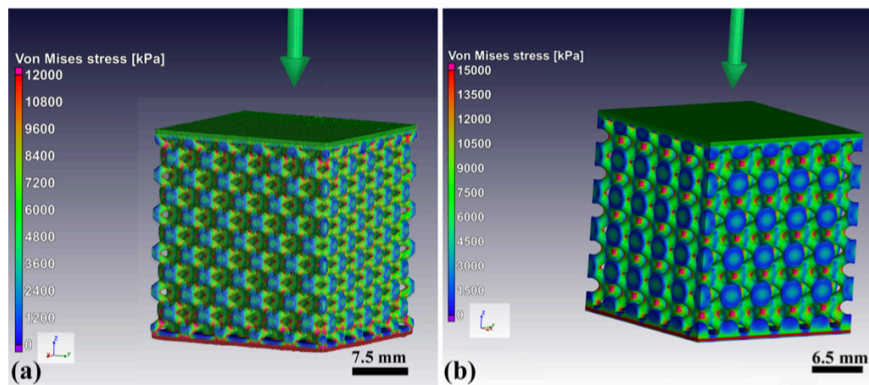


Figure 1-11: Rhombic dodecahedron (a) and diagonal (b) cells [12]

One of the aims of FE numerical modelling of ideal structures is the identification of a homogenized model involving a “small” sub-domain made of a certain number of unit cells representative of the infinite lattice mean (RVE) (Representative volume element). According to the definition provided in [18], RVE “consists in a limited region of the domain that contains the

main microstructural features of the material and responds as the infinite medium, if uniform strain, or stress, and boundary conditions are imposed". The question to be answered is: in which manner the size of the RVE influences the mechanical properties prediction in non-linear regime? With pertinence to this question, a study presented Vigliotti et al. [18] on 2D beam structures in non-linear regime, demonstrates that the size of the RVE is function of the cell type and can be higher than one after a bifurcation in the homogenised stress vs strain curve. Figure 1-12 shows that, in compression, a bifurcation occurs with the consequence that the 1X1 RVE is no more representative of the infinite lattice mean.

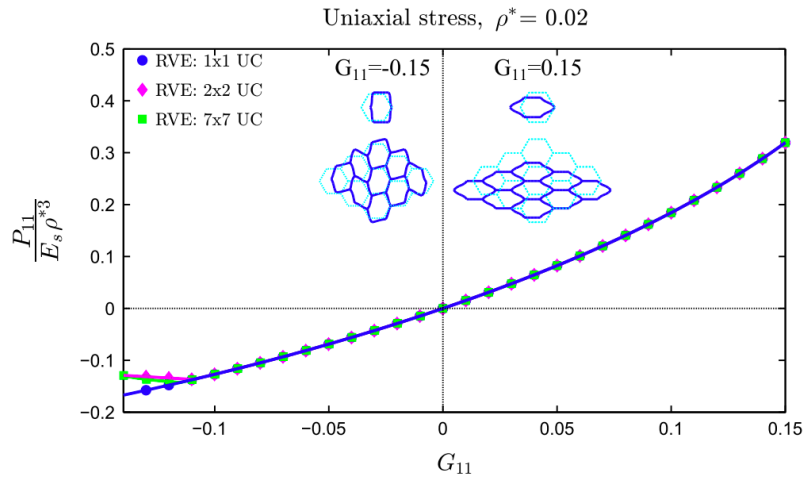


Figure 1-12: Example of bifurcation due to different bucking deformation modes

Bifurcations can occur, for example, for buckling deformation modes because the system tends to follow the buckling wave shape of lowest energy. Regarding the linear elastic behaviour only, a homogenisation Matlab code able to compute the homogenised elastic constants of infinite cellular materials based on FEM simulation is described in [19] and scripts are freely available. Another topic about numerical models has to do with the differences observed between the properties of the RVE (defined as above) and the ones of the specimen estimated by imposing boundary conditions able to replicate the real experiment. To this extent, looking at the results provided by Foletti et al. [20], the dimension of the specimen used for experimental mechanical tests influences its properties (in terms of E and σ_y) up to a certain size for which they are supposed to asymptotically tend to the value of the RVE, therefore, the design of a specimen with suitable size must be realised or at least one should be aware of the error committed respect to the properties of the infinite mean.

2. Design and identification of micro-lattice topology for biomedical application

The first part of the thesis work has the aim of designing two different micro-lattice specimens of the strut-base type with cylindrical struts, candidates for bone substitutions to be 3D printed via SLM using Ti6Al4V powder. The design of the cell involves either the choice of the shape and the choice of two independent geometrical parameters among: strut length, strut diameter, pore size and porosity.

To fix ideas, an example is made in Figure 2-1.

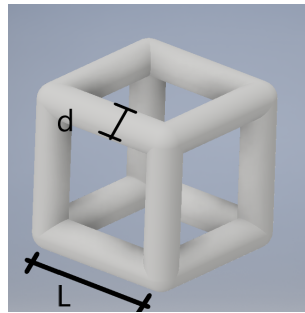


Figure 2-1: example of cubic cell: strut diameter (d) and strut length (L) are independent parameters

As it is possible to see from the figure, once a cell shape is selected (simple cubic shape is considered here for simplicity) other two parameters (strut diameter and strut length in this example) are enough to fully characterise the ideal micro-lattice either in terms of geometry and in terms of elastic properties. In other words, the definition of two parameters among E (Young Modulus), L (strut length), d (strut diameter), P (porosity) and p (pore size) characterises univocally an ideal unit cell of a certain geometry.

In order to orient the selection and the design for the printing session, prior decisions have been taken in terms of which independent variables to look at and in terms of which variables boundaries to consider.

As far as interesting variables goes, Young modulus, pore size, UTS (ultimate compressive stress) and σ_y summarise the main features of micro-lattice orthopaedic implants and material in general. In the preliminary design phase, particular attention is paid to E (Young modulus) and p (pore size) that control stress shielding the former and cell seeding and vascularization on the latter. These last have been chosen to build up a target design area onto an E vs p chart. Regarding the values, the interval between 500-1000 μm is taken for pore size in line with the values suggested in literature, while 500 MPa and 4000 MPa are the boundaries for Young modulus. The choice of E is dictated by different aspects: first of all, as mentioned in paragraph 1.1.4, the state of the art of micro-lattice prosthesis presented already the matching of cancellous bone properties as a possible alternative, in this condition, the structure has minor load bearing function but improved bone in-growth features with the aim of enabling a bone reconstruction all around; what is more, the increase of Young modulus is, in general terms, associated to a decrease of the micro-lattice porosity and pore size and consequent possible issues with SLM manufacturing; to conclude, such a design interval for E ensures the total avoidance of stress shielding which is one of the main reasons why micro-lattice prosthesis are built.

2.1 CAD design and pore size computation

Seven unit cell with different topology have been chosen as possible candidates for the printing session based on those structures that are more recurrent in literature. They are shown in Figure 2-2.

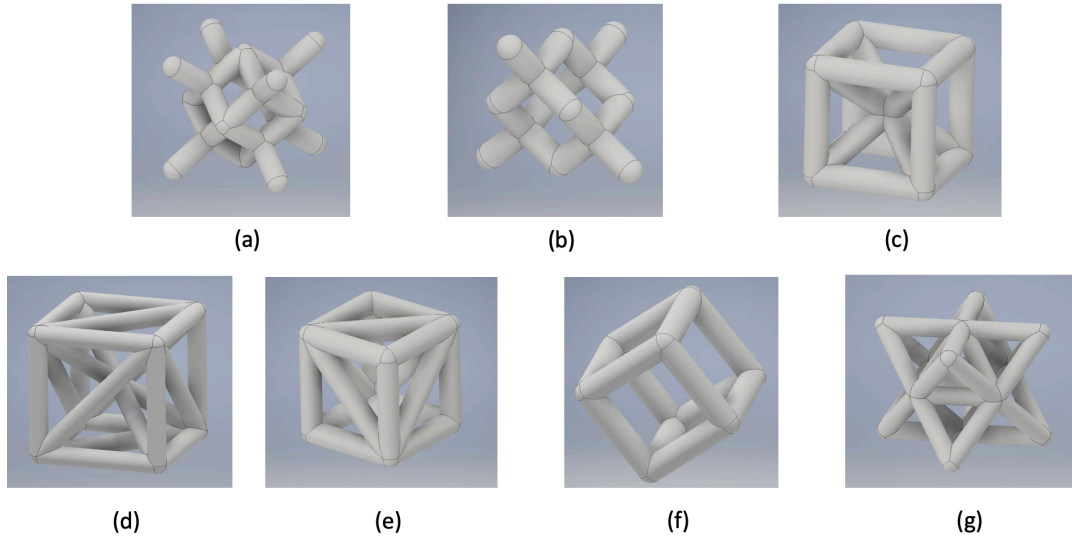


Figure 2-2: the seven unit cell shapes taken for the initial step of design; in order: (a) dodecahedron, (b) diamond, (c) BCC, (d) tetrahedron, (e) FCC, (f) H45, (g) octet truss.

Whereas structures (a), (c), (f) and (g) own three planes of geometric symmetry and form the lattice by either a symmetric or a periodic repetition of the unit cell without differences in the final shape, a clarification on the way the micro-lattice is obtained must be made for the remaining three geometries. Even if the base unit of (d) and (e) own three planes of symmetry, a $2 \times 2 \times 2$ configuration, realised with a mirror operation, is needed to get a structure for which the infinite lattice can be equally achieved with a mirror or pattern repetition. As a consequence, the micro-lattice reference unit becomes $2 \times 2 \times 2$ instead of $1 \times 1 \times 1$ for (d) and (e) (Figure 2-3).

Diamond is the only arrangement without planes of symmetry: therefore, the only manner to realise the infinite correctly shaped micro-lattice is by periodically repeating the unit cell with a pattern. This distinction on the building of the metamaterial is important because it affects the way BC (boundary conditions) must be imposed in the FE simulations to make the base unit representative of the infinite mean as it will be shown later.

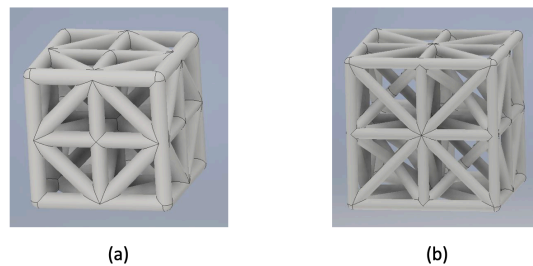


Figure 2-3: $2 \times 2 \times 2$ base unit for FCC (a) and Tetrahedron (b)

The initial design of the candidate cells consists in the selection of either strut length 'L' and strut diameter 'd'; the logic to set those values is mainly devoted to printability issues, to this extent, the reference intervals which have been considered are:

Strut diameter: $0.3 < d < 0.8$ mm

Strut length: $L > 1.2$ mm

Non-dimensional Strut length ($\lambda = \frac{L}{d}$): $4 < \lambda < 6.5$

The lower bound on 'd' is suggested by the common experience that, in the printing of micro-lattice samples, the precision would be to low and so the quality [5], the upper bound limits mainly the Young modulus which would otherwise get out of the target range set for this work. On the other end, the lower limit of 'L' guarantees that the pore size will not be too small as well as 'E' would not be too high.

Table 3 resumes all the selected geometrical parameters of the candidate micro-lattice.

structure	code	Strut diameter (d)	Strut length (L)	unit
BCC	0416	0.4	1.6	mm
	0418	0.4	1.8	mm
FCC	0415	0.4	1.5	mm
	0416	0.4	1.6	mm
	0418	0.4	1.8	mm
Tetrahedron	0416	0.4	1.6	mm
	0418	0.4	1.8	mm
	0420	0.4	2	mm
Diamond	0416	0.4	1.6	mm
	0418	0.4	1.8	mm
	0420	0.4	2	mm
H45	0416	0.4	1.6	mm
Octet truss	0424	0.4	2.4	mm
Dodecahedron	0416	0.4	1.6	mm
	0420	0.4	2	mm

Table 3: geometric properties of the candidate micro-lattice subjected to pore size and Young modulus analysis

The software Digimat by Dassault system has been used for the CAD modelling of the unit cells. Although it is normally used for the design and FE analysis of composite materials, Digimat offers also an easy and fast approach to design lattice strut-based structures with of the 'custom 3D' option. It is possible to define the coordinates of the nodes that connects two or more struts and join them with circular beams of a specified diameter. The units have been generated with the so called 'closed-strut' configuration (like the one of Figure 2-2). The CAD-designed scaffolds have been saved with Parasolid (X_T) format and imported to Autodesk Inventor to compute their porosity 'P'.

As previously mentioned, pore size (p) is defined as the maximum inscribed ball inside the micro-lattice and, based on such definition, no simple commands nor tools are available in traditional CAD software like Inventor to perform its evaluation. To overcome said issue, a simple Matlab code able to calculate pore size has been written. A complete description of its functioning is discussed below.

The code takes a 3D voxel matrix of 1 and 0 that represents the specific cell as input; 1 is associated to the presence of material, 0 is associated to a void. The operations to move from the ITP CAD model to the voxel matrix are the following:

1. Starting from the CAD model, transform the format from ITP to STL Inside Autodesk Inventor.
2. Import the STL format to Autodesk Netfabb and set its resolution; for all the cases a resolution of 10 μm has been assigned so that each element of the final matrix is representative for a cubic space of 10x10x10 μm
3. Export the STL format as slices: at the end of this operation, a stack of PNG images is stored into a file, each image representative of subsequent section of the original cell with the same resolution of 10 μm .
4. Import the slices to Matlab using the function 'uigetfile' and arrange them to create a cubic matrix with a for cycle; The lines of code to perform this operation are shown in Figure 2-4.

```
[file, path] = uigetfile('*.png', 'MultiSelect', 'on');

for ii = 1:length(file)
    temp=imread(file{ii});
    mat(:,:,ii) = temp(:,:,1);
end
```

Figure 2-4: Code lines to import slices and arrange the 3D voxel matrix

The variable 'mat' is a 3D voxel matrix in which numbers are on the usual scale 0-255, (0 for white region (void), 255 for black region (full) and different tonality of grey for all the numbers between). The images exported from Netfabb owns only black and white colours thus the values of the matrix are either 255 or 0. A final transformation turns 255 into 1 and the target matrix of 1 and 0 is created. This last operation could theoretically be avoided and is made only for stylistic reasons. The main part of the code, by means of three for cycles one inside the other, goes through, one by one, each point of the 'mat' matrix and creates, centred in each point, an inscribed sphere which is a possible candidate to be the maximum. Before entering into the for cycles, three auxiliary matrices are defined. They are called B_{xy} , B_{zy} and B_{xz} and are generated with a pre-defined Matlab function called 'bwdist'. The latter takes a 2D voxel matrix of 1 and 0 as input and gives back, for each pixel different than one, the distance from the nearest non-zero pixel; since 'bwdist' acts on a 2D matrix, the operation is repeated for each section of mat toward z direction to get B_{xy} , toward y direction for B_{xz} and toward x direction to get B_{zy} . Whenever 'bwdist' encounters a 1 it returns 0. Figure 2-5 provides a visual example of 'bwdist':

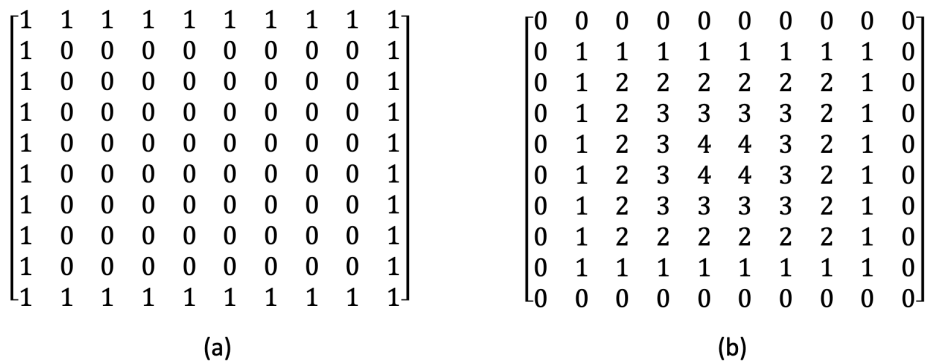


Figure 2-5: example of how the Matlab function 'bwdist' works: (a) is the input matrix and (b) is the output

Inside the system of three for cycles, at first, an initial trial value of the radius of a possible candidate inscribed sphere is defined equal to the minimum value among the one of the three matrices B_{xy} , B_{xz} and B_{zx} at the correspondent set of 3D coordinate; the name of the radius is 'val'. 'val' might be higher than the radius of an inscribed sphere, nevertheless, it is a reasonable value from which to start to look for the biggest inscribed sphere whose centre has the specific coordinates of each step.

mat_2 , a 3D matrix full of zeros with the same size of mat , is defined and a sphere of radius equal to 'val' is built inside.

For a generic iteration, jj , ii and zz is the set of coordinates representing the centre of the sphere whose initial radius is set equal to val (jj is associated to x , ii to y and zz to z in a cartesian reference system). The generation of the sphere is performed by stacking several circumferences in the x - y plane one after the other with increasing radius from planes $zz-val$ to zz and with decreasing radius from planes zz to $zz+val$. The part of script which constructs the sphere is reported in Figure 2-6.

```

for zzzz = zz-val:zz+val

    j_1 = jj + sqrt(val^2 - (zz - zzzz)^2);
    j_2 = jj - sqrt(val^2 - (zz - zzzz)^2);
    j_sup = ceil(max(j_1,j_2));
    j_inf = floor(min(j_1,j_2));

    for jjjj = j_inf:j_sup

        val_new = abs(j_sup) - abs(j_inf);
        i_1 = ii + sqrt(val_new^2 - (jj - jjjj)^2);
        i_2 = ii - sqrt(val_new^2 - (jj - jjjj)^2);
        i_sup = ceil(max(i_1,i_2));
        i_inf = floor(min(i_1,i_2));

        mat2(i_inf:i_sup,jjjj,zzzz) = 1;

    end
end

```

Figure 2-6: Code lines for the generation of the sphere inside mat_2

As it is possible to appreciate from Figure 2-6, the circumferences are numerically assembled by solving their equation thus obtaining the two points of intersections with either the x or y axis. Once the sphere of radius val is inserted into mat_2 , the former is multiplied times the original matrix mat with the point by point multiplication (each value of one matrix is multiplied times the value of the other matrix at the correspondent set of 3D coordinates). If the new matrix, generated by the product of mat and mat_2 , does not contain any value equal to 1, it means that no point of intersection exists between the sphere and the micro-lattice cell and so the quantity val can be directly saved into a vector called $D2$. Otherwise, in case one or more point of intersection are found, the sphere is not inscribed, and its radius must be decreased. The algorithm recognizes the coordinates of all the points of intersection applying the Matlab function 'ind2sub' and calculates the distances between the centre of the sphere and every point of intersection; the minimum among all distances is the radius of a new sphere that is the maximum inscribed sphere centred in the specific set of coordinates ii , jj , zz ; its value is saved inside $D2$.

At the end of the system of for cycles, after all the points have been investigated and all the possible candidate inscribed spheres have been built, the variable $D2$ contains the values of radius of all the overmentioned spheres. The maximum of $D2$ multiplied times two is finally the pore size p . Because the resolution is always set to $10\ \mu\text{m}$, the computed quantity is multiplied times ten in such a way that the unit of p becomes micro-meters. Indeed, the final multiplication factor can be adjusted for different resolutions of the input images stack. The algorithm is flexible and can be used also to evaluate the pore size of a real tomography; of course, the higher are resolution and micro-lattice size and the higher is the computational time. A final picture showing the visual output of the algorithm with the maximum inscribed sphere into a Tetrahedron cell (taken as example) is reported in Figure 2-7.

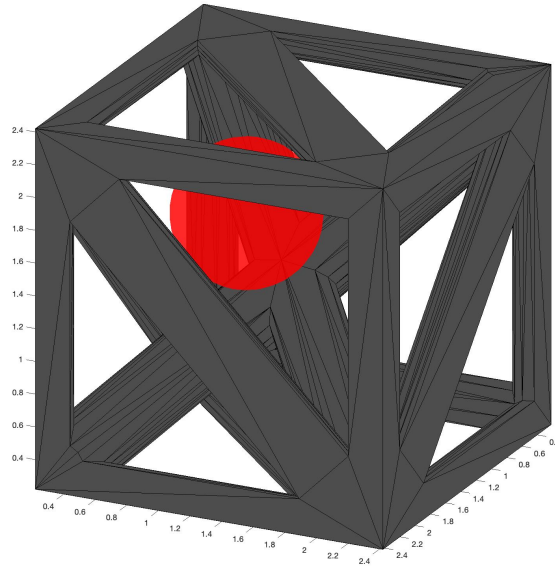


Figure 2-7: Visual output of the algorithm

2.2 Young modulus evaluation

Numerical linear Finite Element (FE) simulation have been carried out in compression to investigate the Young modulus of the micro-lattice units in Abaqus CAE and understand which candidates get closer to the target area on the E vs p chart. Because the models are linear, no difference in the results occurs between tension and compression and, therefore, only the latter load case is implemented. Even though the geometric parameters initially set for the cells will not necessarily be the ones of the final to be printed specimens, they are helpful to give an idea of the elastic stiffness of each geometry with similar dimensions in a range of good printability. The RVE approach has been followed in the sense that appropriate BC have been applied so that a single periodic unit cell is representative of the infinite metamaterial, as a matter of fact, is taken for granted that the size of the RVE doesn't affect the elastic modulus as stated in [18].

At this stage, an important distinction must be pointed out between those structures whose unit cell owns three planes of symmetries, and those who don't: only diamond in this case. The distinction affects the way BC must be defined in order to make the periodic unit representative of the infinite mean: periodic BC for symmetric structures in the first case (which impose planarity of the surfaces), general periodic BC for the second. General periodic BC are always correct but involve a much higher computational effort and are avoided when possible. Before making the focus and explaining the difference among the two BC types, those steps which are common to each analysis are described.

The first step regards the geometry to import in Abaqus: for a coherent homogenisation, it is mandatory to consider the so called open-strut configuration instead of the closed-strut one (Figure 2-8). The former implies half of the struts on the surfaces and one quarter of strut on the edges. Indeed, the imposing of symmetric BC in Abaqus would overestimate the stiffness (and all mechanical properties in general) in case of closed-strut leading to wrong results.

All the cells are cut in Inventor and exported into SAT format which is suitable to be read into Abaqus. A qualitative picture of those structures is shown in Figure 2-9.

Linear elastic material properties for Ti6Al4V have been set based on the parameters of a printed sample according to [21]: $E = 112000$ MPa and ν (Poisson ratio) = 0.34 and a solid homogeneous section has been defined and assigned. A static general step has been implemented and, for each analysis, a quadratic mesh of tetrahedral elements of 0.07 mm size has been used after performing a rapid convergence analysis between 0.08 0.07 and 0.06 on the BCC0418 (taken as sample and reported in Table 3) accepting a relative error lower than 1%.

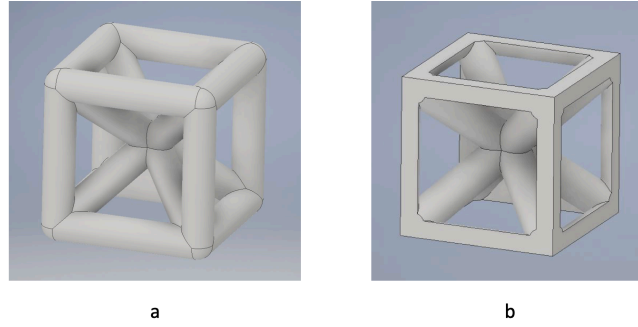


Figure 2-8: comparison between close-cell configuration (a) and open-cell configuration (b) on a BCC cell

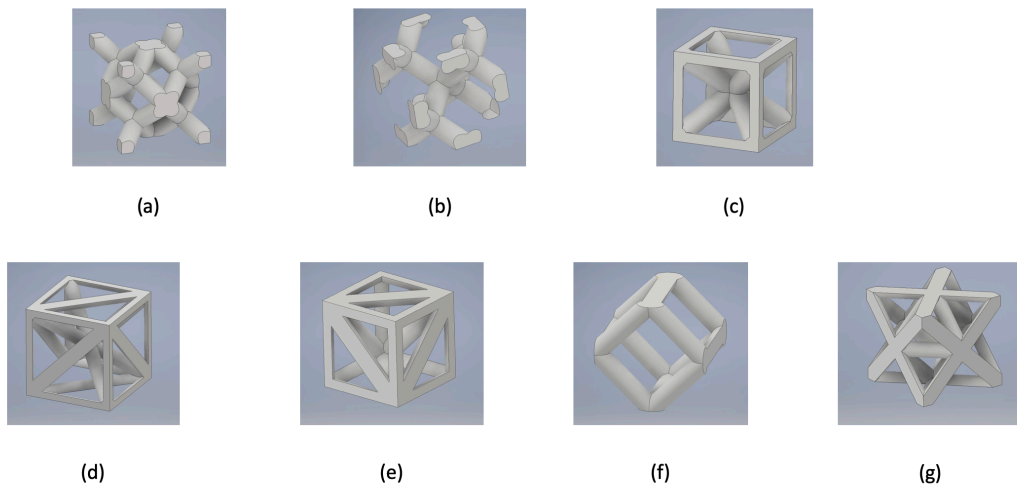


Figure 2-9: candidate structures with "open-strut" configuration

2.2.1 Periodic boundary conditions for symmetric structures

The periodic BC for symmetric structures constrain the cell faces so that they remain plane and always delimited by a parallelepiped while the cubic cell deforms. Considering the three planes passing through the centre of gravity of the cell and any couple of correspondent symmetric node respect to those planes, they get the same relative displacement. It is important to underline that these PBC work only for tensile and compressive load cases.

A successful homogenization can be achieved by imposing these BC to a single unit cell that owns three planes of symmetry (in general along the direction x-y-z of a cartesian reference unit) or to those structures that generate the lattice with mirror operations. Based on this consideration, a single 1x1x1 unit of (a), (c), (f), (g) is subjected to symmetric BC as well as a single 1x1x1 unit of (d) and (e). Once again, even though (d) and (e) are not symmetric respect to the three planes passing through their centre of gravity, they create the metamaterial with subsequent mirror operations, and this justifies the possibility of modelling a 1x1x1 sample only and save computational time.

To reproduce the planarity of the faces in Abaqus, with reference to the schematic cube of Figure 2-10, the displacements of the nodes on faces 3, 5 and 6 have been blocked in the out-of-plane direction (by setting equal to zero the linear displacement in the direction normal to the plane and the out-of-plane rotations) so for example, referring to x-y surface, $U_3 = 0$, $UR_1 = UR_2 = 0$. What is more, an interaction equation-type has been applied to faces 4 and 6. The interaction consists in imposing the displacements of a set of N 'slave' nodes equal to the one of a single 'master' node so that they all move on the same plane.

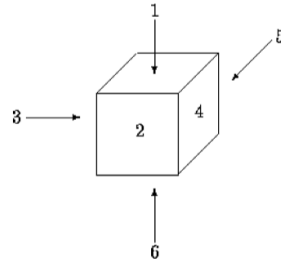


Figure 2-10: Reference cube

In symbols the equation looks like:

$$Ax_i + Bx_N = 0 \quad \text{with } i = 1, 2, \dots, N - 1$$

Where x_i and x_N are the vectors of the displacements of the i -th slave node and of the master node respectively and A and B are the two coefficient of the equation, 1 and -1 in this case so that finally:

$$x_i = x_N \quad \text{with } i = 1, 2, \dots, N - 1$$

For all the cases, a compressive deformation of 1% is applied to the upper surface (face 1). In Figure 2-11 an example of constraints and load is shown and Figure 2-12 visualises slave and master node for the interaction equation-type. The BCC is taken here as example, but the same procedure has been applied to all the structures suitable for symmetric BC.

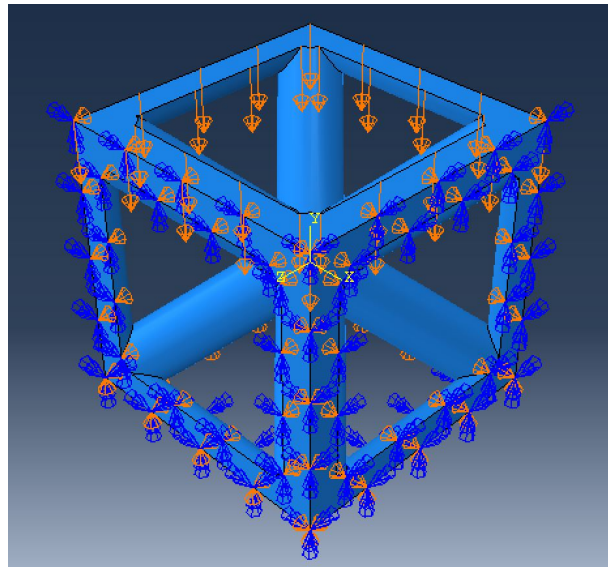


Figure 2-11: symmetric BC applied to a BCC structure taken as example

Finally, pictures of the deformed shape and of the displacement U_1 , U_2 , U_3 are shown in Figure 2-13. To compute the Young modulus, on surface 1, all the reaction forces in y direction (RF2) are saved and summed leading to the total force which is then divided times the area of a cube with a square equal to the strut length of the cell and the displacement of a single node in y (U_2) direction is saved and divided times the strut length L . The two quantities are combined and in the stress strain chart and E is derived. It is worth pointing out that by proceeding this way, the homogenised stress vs strain curve is obtained.

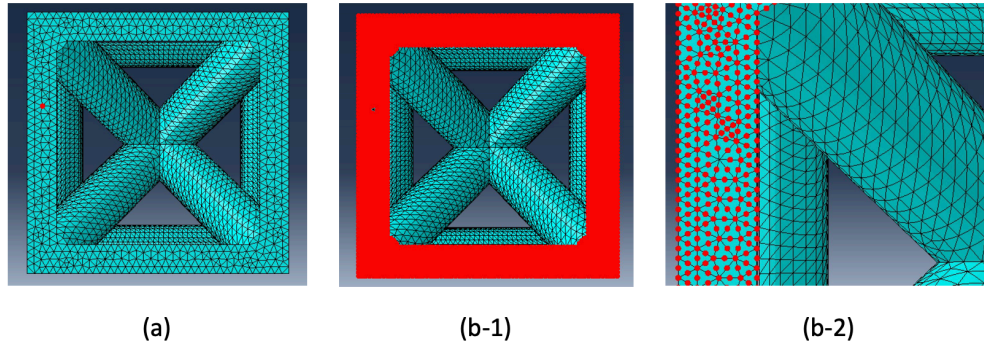


Figure 2-12: sets for the equation constraints: (a) shows the master node, (b1) all the slaves node; (b2) is a focus to see the missing node among the slaves

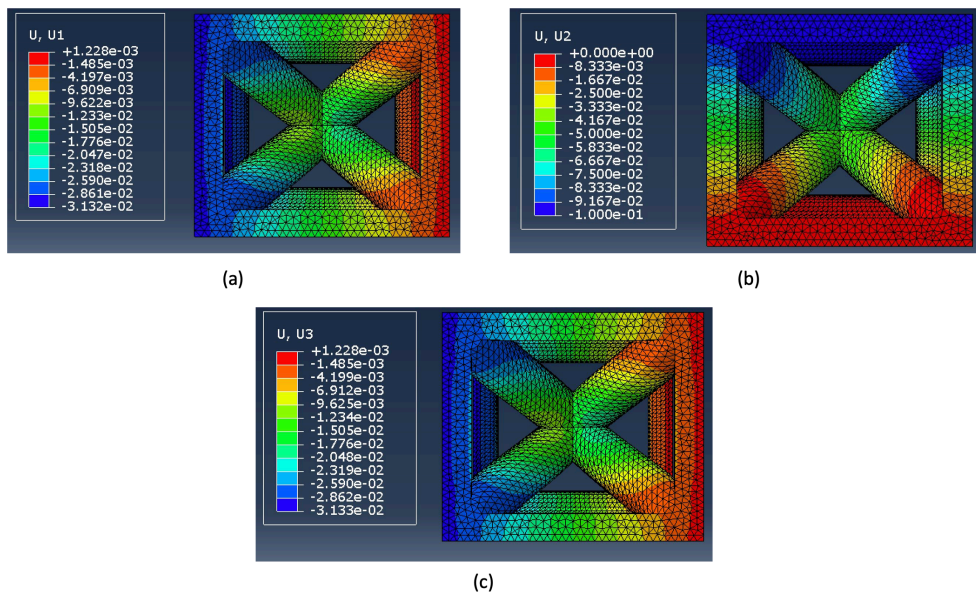


Figure 2-13: deformed shape of BCC and displacements in x-y (a) – (b) and x-z (c) planes

2.2.2 General Periodic boundary conditions

If a structure does not possess three planes of symmetry nor form the metamaterial by mirroring the base unit, the planarity of the boundary faces cannot be imposed to ensure periodicity because, for structures of this type, it is not granted that the deformation mode of the faces is planar but can assume any form. To solve this issue, periodic BC has been applied using the Abaqus plug-in Homtools [22] which can be freely downloaded from the net. Homtools is a homogenization toolbox based on a set of Python scripts that can be used, in general, to estimate the average mechanical response of a metamaterial by means of a FE applied on the periodic unit. Among the options Homtools offers, there is the so called periodic boundary condition (PBC) option which guarantees that the stress and strain are periodic within the metamaterial at the level of periodicity of the single cell. Given two opposite faces of the cubic unit, the PBC option applies a linear constraint to each couple of correspondent nodes so that their displacements are coupled. To understand what Homtools actually does, an example, simplified to the 2D case, is shown in Figure 2-14.

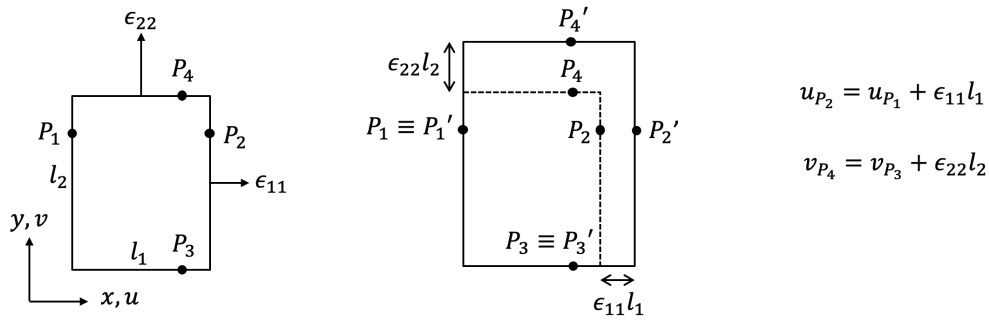


Figure 2-14: 2D example of the constraints applied by Homtools

The two quantities ϵ_{11} and ϵ_{22} owns to ϵ_{ij} , i.e. the macroscopic strain tensor and they are equal to the displacements of RP1 and RP2: ($u_{RP1} = \epsilon_{11}$ and $v_{RP2} = \epsilon_{22}$) two reference points that are appositely defined in Abaqus. To extend the approach to the 3D case, the strain ω referred to z direction is introduced and the reference point RP3 defined so that $w_{RP3} = \epsilon_{33}$. The mesh of opposite faces must be identical and to each node of a face must correspond a node on the opposite face in the same position. The realisation of identical mesh between each couple of faces is enhanced in Abaqus with the specific command 'create mesh pattern' in the edit menu. From a practical point of view, to apply the PBC, after creating the three reference points that represent the values of each line of the macroscopic strain tensor (RP1 the first line, RP2 the second and RP3 the third), plug-in/Homtools is selected in the interaction module. From the outstanding menu, the voice 'periodic boundary condition' is chosen and the window is filled with all the information required:

1. Selection of 'finite strain' option.
2. Editing of the 3 reference points.
3. Selection of the sets to be coupled (two opposite faces in this case).
4. Definition of the periodicity vector which indicates the distance between the nodes of the selected sets.

In the end, the coupling between two opposite faces is performed; of course, the same procedure must be repeated for the other two pair of surfaces.

As far as the application of loads and constraints goes, Figure 2-15 shows that they are attached directly to the reference points taking care that what Abaqus reads are strains and not displacements. To impose a compressive load along y direction, therefore, the following assignments are defined:

$$\begin{aligned} \text{RP1: } & v_{RP1} = 0 \quad w_{RP1} = 0 \\ \text{RP2: } & u_{RP2} = 0 \quad v_{RP1} = -0.01 \quad \omega_{RP1} = 0 \\ \text{RP3: } & u_{RP1} = 0 \quad v_{RP1} = 0 \end{aligned}$$

Finally, the displacements of one single node have been constrained to make the solution unique. As a matter of fact, the rigid translation of the structure is not fixed by the periodic conditions given by Homtools. Regarding to the preliminary analysis on the Young Modulus, only diamond (structure (b) of Figure 2-9) was subjected to these periodic BC since, from a geometric point of view, it is the only one not owning planes of symmetry nor leading to the metamaterial by mirrors.

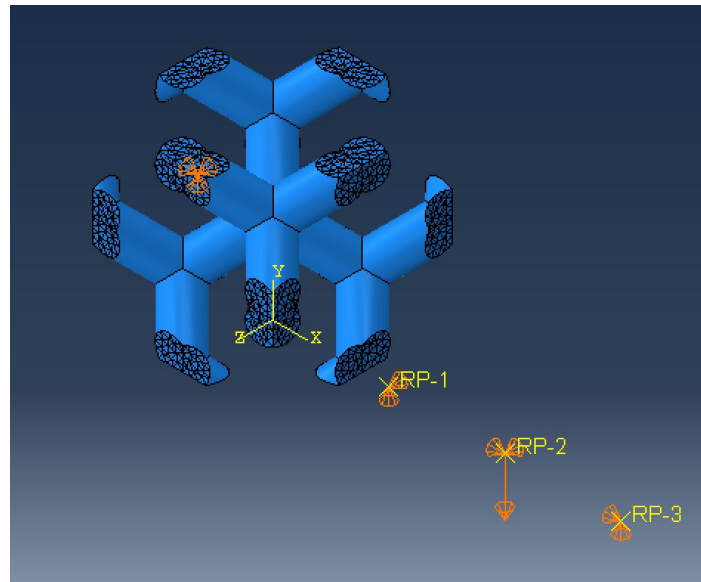


Figure 2-15: Constraints and imposed displacement for general PBC

2.3 Results and selection of candidate structures to be printed

For all the structures listed in Table 3, the measurement of pore size and the evaluation of Young modulus has been performed with the methods discussed qualitatively in 2.1 and 2.2. Table 4 resumes of the results of the preliminary analysis.

structure	Porosity (P^*)	Strut diameter (d)	Strut length (L)	Pore size (p)	Young modulus (E)
BCC0416	64.77 %	0.4 [mm]	1.6 [mm]	480 [μm]	11415 [MPa]
BCC0418	70.98 %	0.4 [mm]	1.8 [mm]	530 [μm]	8270 [MPa]
FCC0415	69.8 %	0.4 [mm]	1.5 [mm]	1080 [μm]	12605 [MPa]
FCC0416	72.9 %	0.4 [mm]	1.6 [mm]	1180 [μm]	10845 [MPa]
FCC0418	77.84 %	0.4 [mm]	1.8 [mm]	1380 [μm]	8879 [MPa]
Tetrahedron0416	61.38 %	0.4 [mm]	1.6 [mm]	540 [μm]	13339 [MPa]
Tetrahedron0418	68.53 %	0.4 [mm]	1.8 [mm]	620 [μm]	9713 [MPa]
Tetrahedron 0420	73.68 %	0.4 [mm]	2 [mm]	760 [μm]	7570 [MPa]
Diamond0416	73.65 %	0.4 [mm]	1.6 [mm]	900 [μm]	4582 [MPa]
Diamond0418	78.45 %	0.4 [mm]	1.8 [mm]	1060 [μm]	2932 [MPa]
Diamond0420	82.15 %	0.4 [mm]	2 [mm]	1220 [μm]	1223 [MPa]
H45041	71.4 %	0.4 [mm]	1 [mm]	980 [μm]	4128 [MPa]
H450416	87.4 %	0.4 mm]	1.6 [mm]	1580 [μm]	640 [MPa]
Octet0424	72.9 %	0.4 [mm]	2.4 [mm]	1260 [μm]	6485 [MPa]
Dodecahedron0416	53.34 %	0.4 [mm]	1.6 [mm]	800 [μm]	17801 [MPa]
Dodecahedron0420	68.23 %	0.4 [mm]	2 [mm]	1220 [μm]	6387 [MPa]

Table 4: Results of the preliminary analysis

Figure 2-16 shows the E vs p chart in which the candidate structures are compared with each other and with the target area highlighted in red. The fact that none of them falls within the area is not, at this stage, a problem since it was important to get qualitative information about which structures (at least two) can more easily match the desired values with a modification of L and d so to keep λ inside the interval specified in paragraph 2.1.

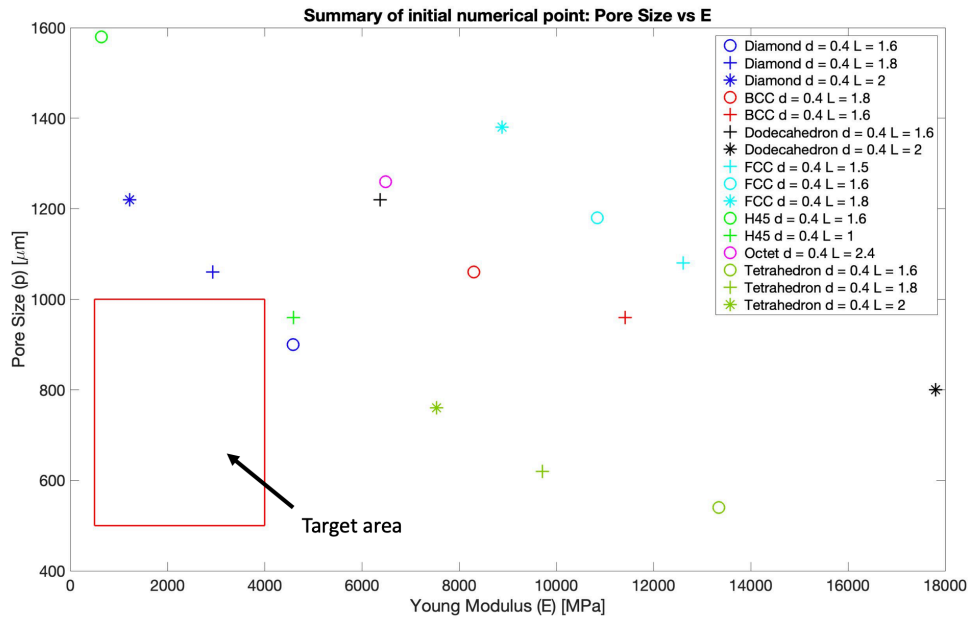


Figure 2-16: representation of the candidate structures on the E vs p chart

The way in which cells of the same geometry and different strut length are positioned on the chart, suggests, with a certain approximation, a linear dependency between E and p for all the structures for which more than one value was computed, at least in a limited range of λ . Respect to the red target area, three structures can be distinguished to be more promising than the others: Tetrahedron (c), diamond (b) and H45 (f). Since, from experience, H45 is highly anisotropic and does not work well under cut loading, the decision to focus on (c) and (b) has been taken.

As already stated at the beginning of chapter 2, two independent parameters rule the geometric and elastic properties of ideal micro-lattice materials of pre-defined unit cell shape; for this reason, it is convenient to define a new set of non-dimensional parameters to decrease the number of handling variables without losing generality. To this extent, the following entities has been introduced:

$$\text{Phi (Non-dimensional pore size): } \phi = \frac{p}{d}$$

$$\text{Lambda (non-dimensional strut length = slenderness): } \lambda = \frac{L}{d}$$

Because of the fact that λ and ϕ are independent, follows that E is fixed once one of the two is fixed. Making the hypothesis that Young modulus and pore size are linearly correlated, also λ and ϕ have this property because they are both obtained scaling p and L by the same parameter d. The Matlab function polyfit has been used to compute the coefficients of the linear regression between either λ vs E and λ vs ϕ for both tetrahedron and diamond giving as input the values of E and p of Table 4 with the addition, only for tetrahedron, of a new point whose values are: L = 2.2 mm, d = 0.37 mm, p = 869 μm , E = 5067 MPa. The reason for this late update for tetrahedron only is due to the fact that, whereas diamond suits almost perfectly the linear hypothesis, an extra point is helpful for tetrahedron to commit a lower mistake.

In symbols:

$$y = Ax + B$$

A and B are the two coefficients calculated, in general terms, by polyfit; results are shown in Table 5 and Table 6.

In Figure 2-17 and Figure 2-18 the linear regression of tetrahedron is shown either for λ vs E and λ vs ϕ . Among the two charts, it is possible to notice that the linear hypothesis for the non-dimensional pore size is more accurate than for the E; this is confirmed by the R^2 , given:

$$R^2 = 1 - \frac{\sum_{i=1}^n (y_i - \hat{y}_i)^2}{\sum_{i=1}^n (y_i - \bar{y})^2}$$

Where y_i is the i -th value of the fitting curve at the correspondent experimental point, \hat{y}_i the value of the i -th experimental point used for the regression and \bar{y} the mean of all the experimental values, it results: $R_{T,\phi}^2 = 0.9914$ and $R_{T,E}^2 = 0.9357$.

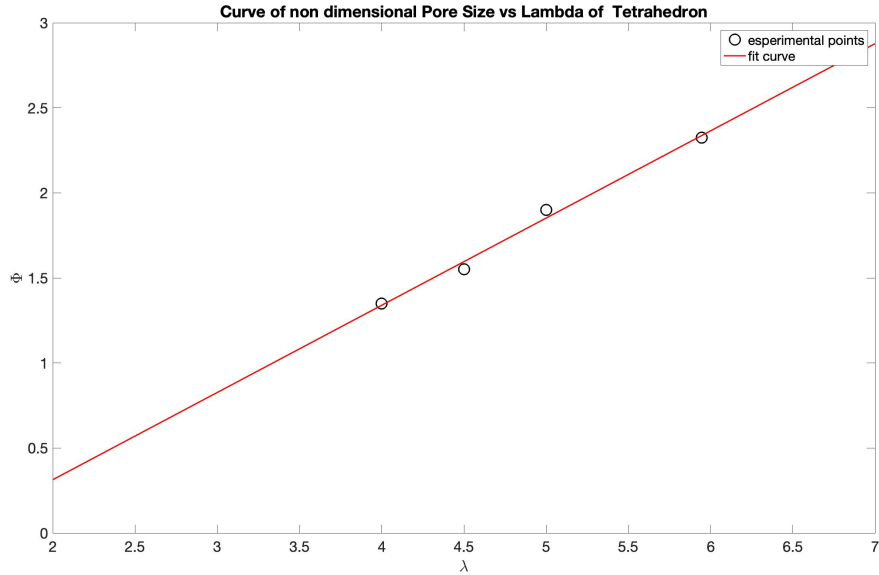


Figure 2-17: Linear regression of λ vs ϕ for Tetrahedron

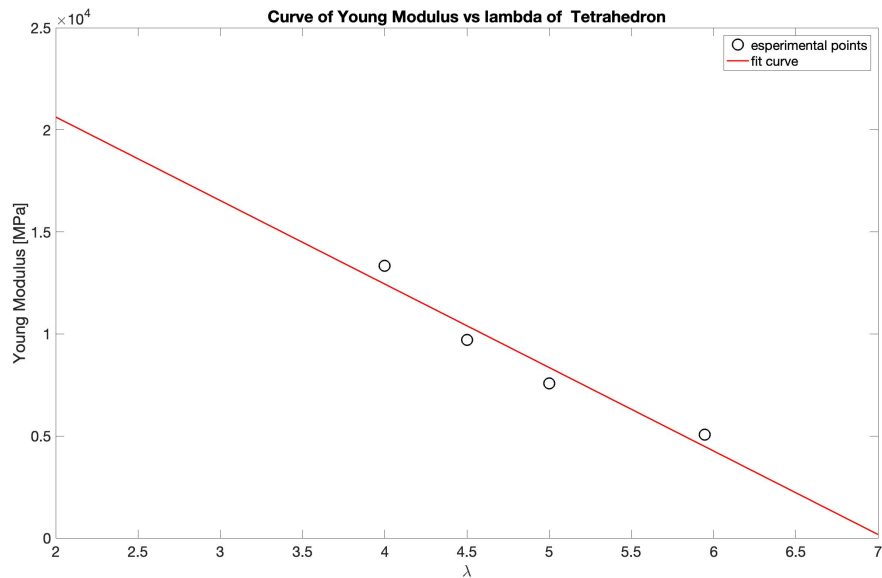


Figure 2-18: Linear regression of λ vs E for Tetrahedron

Tetrahedron				
Linear	A	B	unit	R^2
E vs λ	-4091	28810	[MPa]	0.9357
ϕ vs λ	0.5128	-0.7119	[μm]	0.9914

Table 5: Regression parameters for Tetrahedron

The two values are quite high but, since only four points has been given as input, the actual error committed might be higher. Nevertheless, the choice of a linear fitting has been made mainly to make the building of design areas on the ϕ vs E easier and to enhance a better visualisation. Anyway, an error is expected when using the linear regression to predict Young and pore size giving any values of d and L as input.

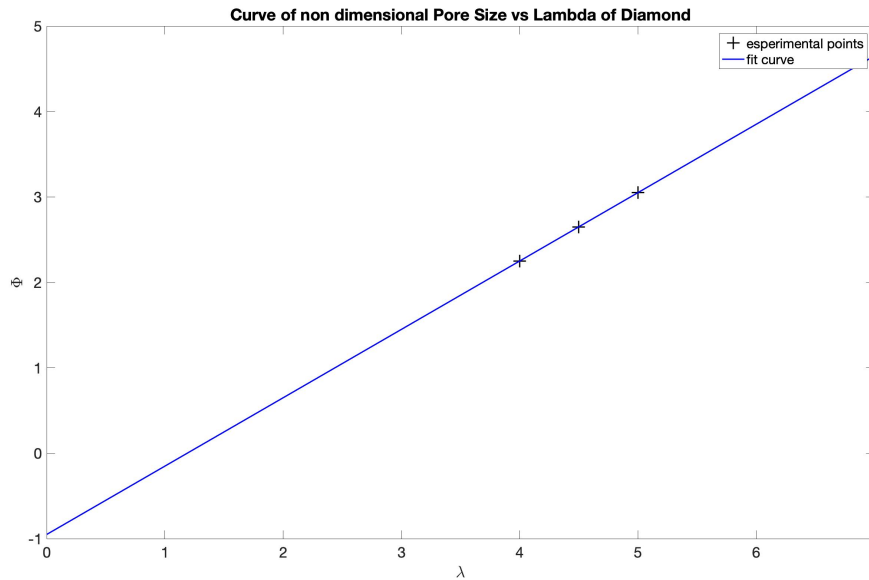


Figure 2-19: Linear regression of λ vs ϕ for Diamond

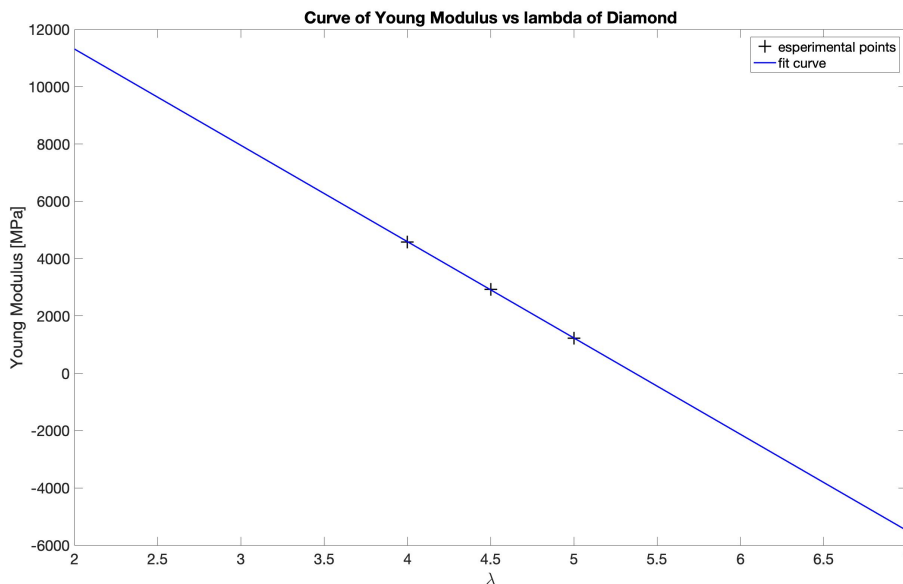


Figure 2-20: Linear regression of λ vs E for Tetrahedron

Figure 2-19 and Figure 2-20 reports the same the linear regressions for Diamond. The values of R^2 confirm the visual impression of the goodness of linear regression for diamond: $R_{D,\phi}^2 = 1$ and $R_{D,E}^2 = 0.999$. In this case, the fitting coefficients A and B can be used to predict pore size and Young modulus without expecting any errors.

Diamond				
Linear	A	B	unit	R^2
E vs λ	-3604	16872	[MPa]	0.999
ϕ vs λ	0.8	-0.95	[μm]	1

Table 6: Regression parameters of Diamond

Design areas, consistent with the constraints on d and L, have been built on the E vs p chart for both structures; said design areas have a trapezoidal shape whose boundaries are built as follow:

1. Right and left boundaries are based on limitations on the value of $\lambda = \frac{L}{d}$ which is linearly dependent to E ($1.5 < \lambda < 6.5$).
In symbols:

$$E_i = A\lambda_i + B \quad \text{where} \quad \lambda_i = \frac{L_i}{d_i} \quad \text{both } L_i \text{ and } d_i \text{ are imposed and so } E_i \text{ is defined,}$$

i is a generic index that enables λ varying between 1.5 and 6.5

2. Up and down boundaries are built by multiplying the curve ϕ times $d_{up} = 0.8$ and $d_{down} = 0.3$.
In symbols:

$$\phi_i = \frac{p_i}{d_i} = A\lambda + B$$

by setting different values of 'd' each specific line iso-d is created and represent how 'p_i' changes as a function of λ .

The parameters A and B are not always the same but change for the two different structures and for the two different charts according to Table 5 and Table 6.

The results are shown in Figure 2-21 for Tetrahedron and Figure 2-22 for Diamond. A similar approach to define design areas based on geometrical constraints has been applied in the work of [17].

DESIGN CURVE: Tetrahedron

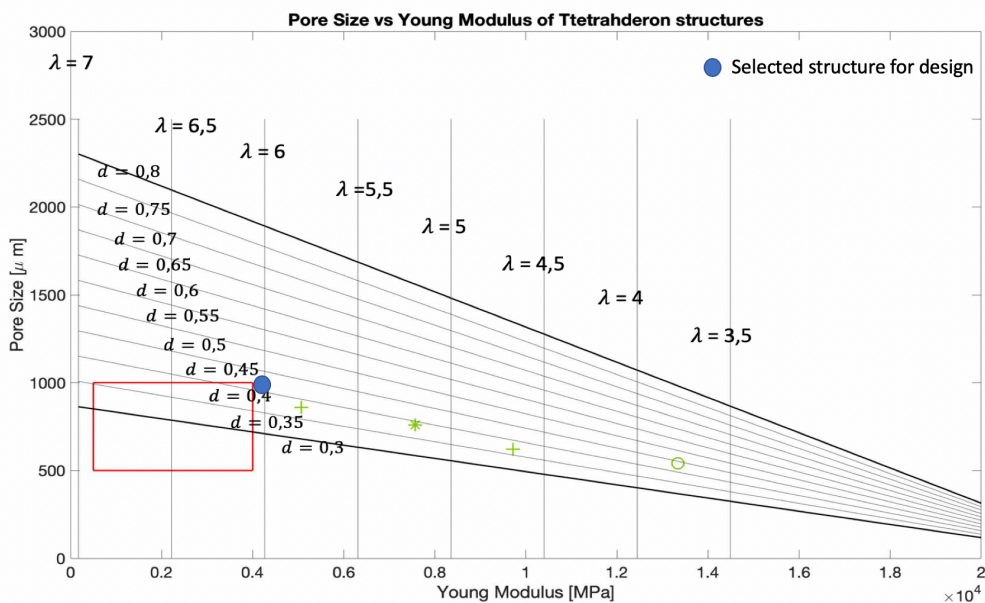


Figure 2-21: Design area for Tetrahedron

DESIGN CURVE: Diamond

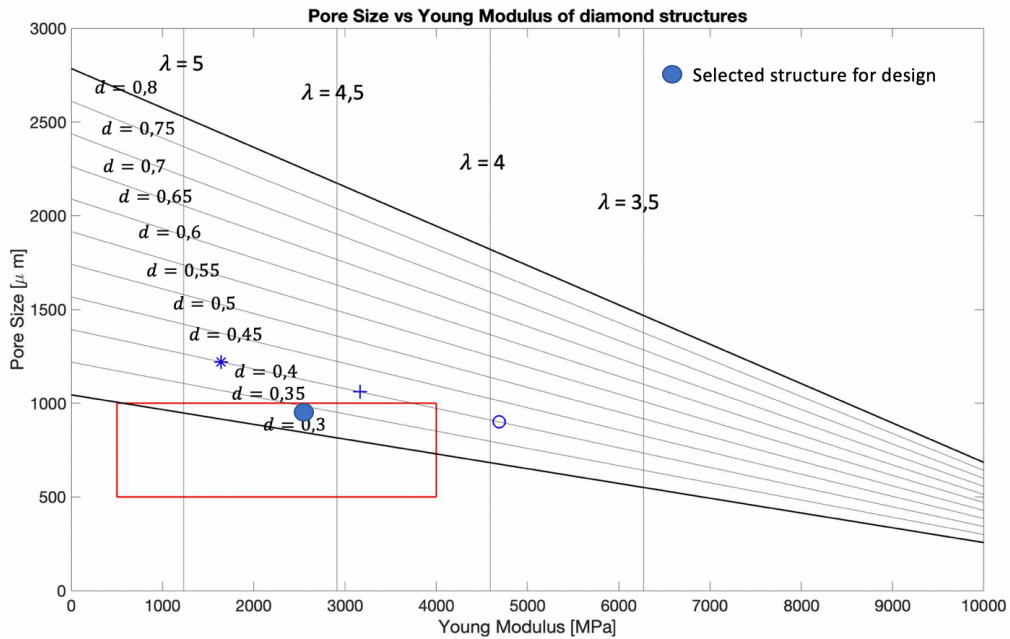


Figure 2-22: Design area for Diamond

For both geometries, as far as linear hypothesis is correct, an intersection between the red target area and the area delimited by d_{up} and d_{down} exists, thus demonstrating the presence of an infinite numbers of ideal geometrical combination suitable to match the required parameters. In the two charts of Figure 2-21 and Figure 2-22 the initial points used for the fitting are shown as well as the ones of the selected cells.

structure	Selected d [mm]	Selected L [mm]	Predicted E [MPa]	Numerical E [MPa]	Error E %	Predicted p [μm]	Numerical p [μm]	Error p %
Tetrahedron	0.33	2.145	2218	4185	47	865	980	11.7
Diamond	0.33	1.55	2565	2565	0	926	920	0.65

Table 7: Design parameters for printing session

Table 7 finally contains the selected values of d and L and the predicted associated elastic modulus and pore size faithful to linear hypothesis.

As far as E is concerned, whereas the estimation is good for Diamond structure, a considerable error is committed for Tetrahedron; a second order fitting for the curve E vs λ might decrease the mistake committed. Anyway, the numerical value on the Young modulus of Tetrahedron is accepted even if slightly higher than 4000 MPa because the discrepancy is very small.

Regarding Tetrahedron structure, a clarification must be done in the sense that the geometry is not orthotropic and, more in detail, the Elastic stiffness along the directions 'y' and 'z' are different from the one along direction 'x' (see Figure 2-23). From a quantitative point of view, it results: $E_y = E_z = 4185$ MPa, $E_x = 4206$ MPa. Direction y is the one significative for the experimental tests and numerical simulations.

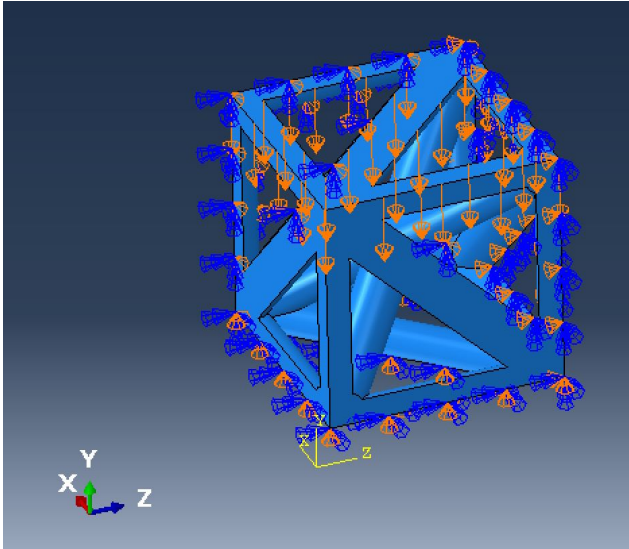


Figure 2-23: Loading direction for tetrahedron structure

3. Compression and tension experimental tests on micro-lattice specimens

The two structures selected and discussed in chapter 2 (Tetrahedron = TET and Diamond = DIA) have been used to design four types of specimens for experimental tests: for each geometry one in compression and one in tension. The two unit cells used to generate the specimens are depicted in Figure 3-1.

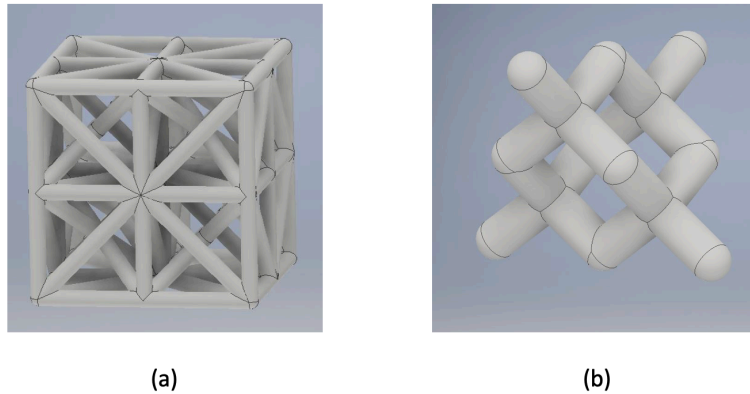


Figure 3-1: Base units for building test specimens: TET (a) and Diamond (b)

3.1 Geometry and preparation of testing specimens

The building of specimens has been realised in Autodesk Inventor; the CAD models has been saved in STL format and sent to Auburn university Alabama for 3D printing with Ti6Al4V powder.

3.1.1 Compression specimens

Compression specimens have been obtained through a geometric pattern leading to the definition of structures with parallelepiped shape and aspect ratio $A = 3$; with:

$$A = \frac{N_{cell,width}}{N_{cell,height}}$$

For Diamond, a 7x7x21 specimen from 1x1x1 periodic unit cell has been built; for TET a 3x3x9 specimen has been constructed from the 2x2x2 unit. Moreover, the upper and lower faces in contact with the plates of the compression machine have been provided with skins of 0.8 mm height to improve the contact and to enhance a better and more homogeneous load distribution to the cells. The two 'ready-to-print' compression specimens are shown in Figure 3-2.

The surfaces of the skins of the real manufactured specimens has been polished to obtain smoother supports and, before being tested, the sides oriented toward the cameras of DIC (Digital

Image Correlation) have been painted with subsequent tonalities of white and black to get a random grey scaled colour distribution needed from DIC to build the speckle. Throughout the manufacturing process, the way in which powder particles are deposited, generally has an impact on the real specimen relative density (ρ_{real}^*) compared to the ideal one, with:

$$\rho^* = \frac{V_u}{V_{cube}} \times 100$$

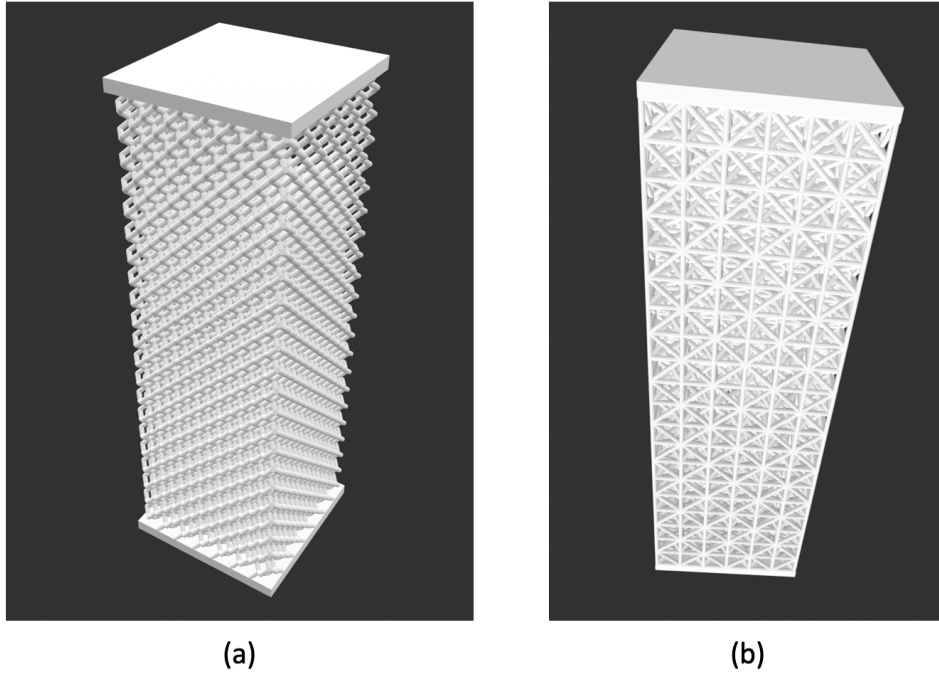


Figure 3-2: Ideal compression specimens: DIA (a) and TET (b).

Structure	Ideal relative density [ρ^*]
DIA	20 %
TET	16.6 %

Table 8: Ideal relative density for compression specimens

3.1.2 Tension specimens

Specimens for tensile tests need to be equipped with a grasping system to perform the mounting on the testing machine and, in doing so, particular care must be taken to avoid that failure occurs at the transition area between gripping and lattice in which stress concentration is likely to occur thus leading to incorrect estimation of the mechanical properties. As pointed out in a previous thesis work carried out at Politecnico di Milano [23], in accordance with the outcome of [14], a possible solution is to increase progressively the strut cross section of cells close to the grasps so to realise a stiffer section and prevent localised failures. The overmentioned approach has been adopted for the current tension specimens.

Both Diamond and TET probes are featured by a central cube of 7x7x7 and 3x3x3 cells respectively with the nominal dimensions presented in paragraph 2.3 and two additional rows in both vertical directions with progressively increasing struts dimensions. These last struts are featured by elliptical sections built via sweep command.

To get them ready for the tests, also tension specimens are painted to obtain the speckle. The two specimens are displayed in Figure 3-3.

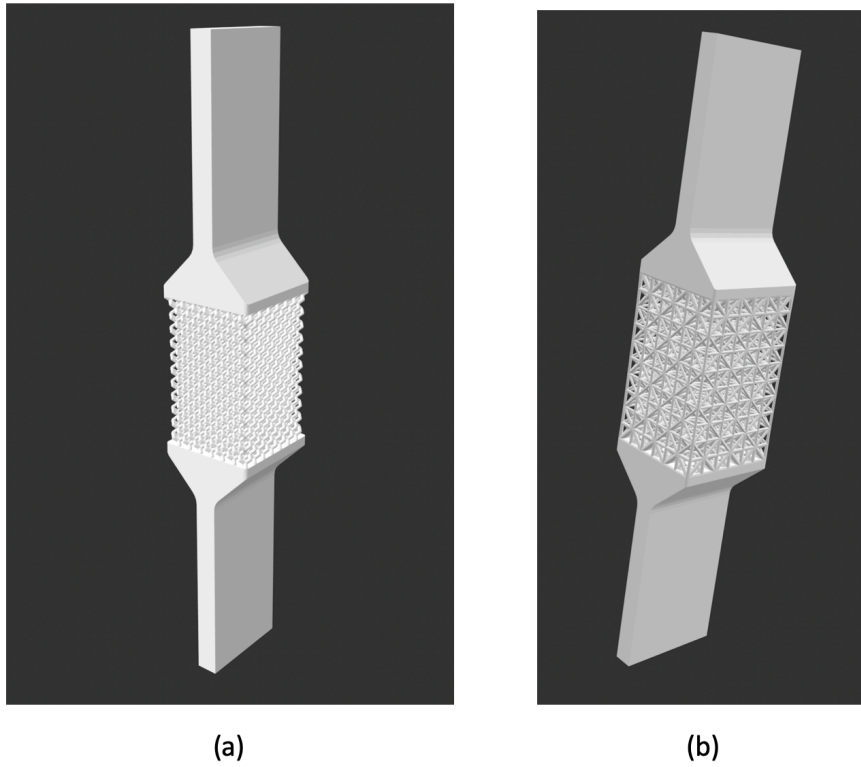


Figure 3-3: Ideal tension specimens: DIA (a) and TET (b).

Three samples for each structure will be tested in tension. Figure 3-4 shows an example of each real printed specimen.

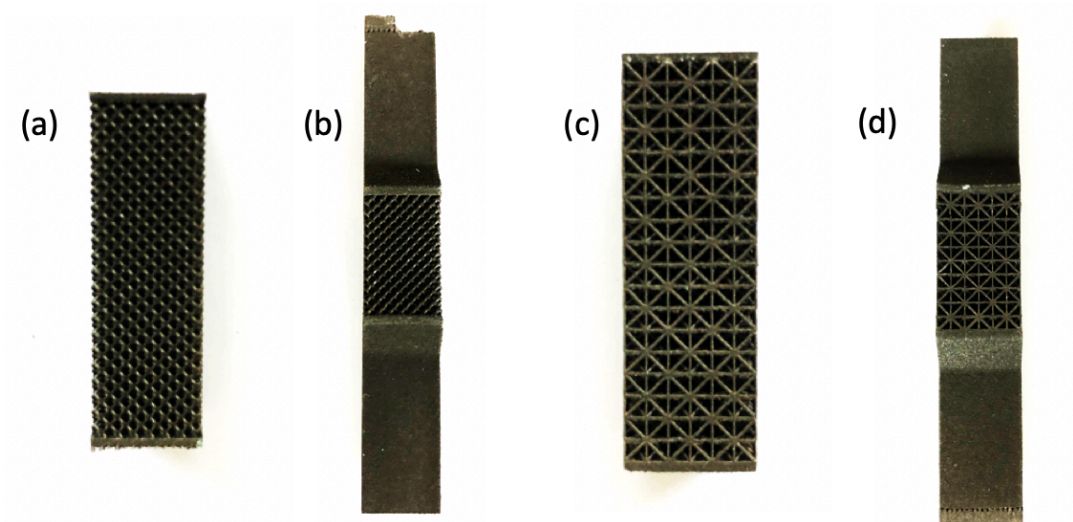


Figure 3-4: Real specimens: (a) Diamond compression, (b) Diamond tension, (c) TET compression, (d) TET tension

3.2 Mechanical testing: set-up, measurement method and procedure

Compression and tension tests have been conducted in the laboratories of Politecnico di Milano on Alliance RF/150, an electrodynamic testing machine with maximum load capacity of 150 KN. For compression, two plates have been mounted to place the micro-lattice; for tension, the machine has been provided with a suitable gripping system able to hold the two grasping plates of the specimens; the two configurations are reported in Figure 3-5.

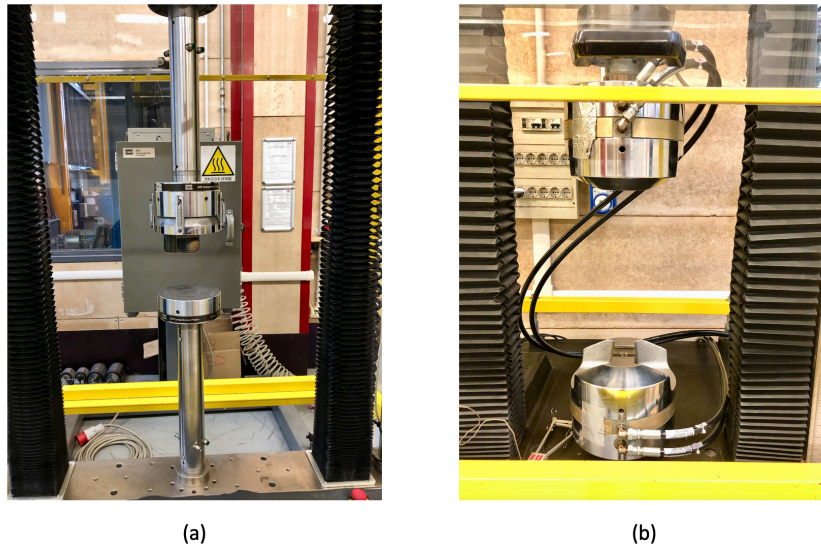


Figure 3-5: Set-up of the testing machine: (a) for compression, (b) for tension

The final output is the homogenised stress vs strain curve from which Young modulus, yield stress, UTS and UCS can be measured.

For both tests, Aramis image acquisition system able to perform DIC (Digital image correlation) has been placed in front of the machine to acquire images and measure stress and strains. DIC is a measurement method able to calculate stress and strains of a component, during its load history, by acquiring and processing a stack of subsequent images at high frequency. The algorithm which governs DIC starts from an image of the undeformed shape in which points, in randomly distributed grey scale, are present and recognize the way each point deforms thus computing localised strains. For this reason, every specimen has been painted as stated in paragraph 3.1. What is more, the image acquisition system is featured by two cameras able to build a 3D speckle and communicates with the control system of the load machine so that the sampling of images performed by Aramis is synchronized with the data (force vs displacement) acquired by the software of the test machine. In this way, each load corresponds to a specific image. A calibration process is needed for Aramis before conducting the tests in order to perform a correct 3D reconstruction of the speckle.

The tests have been conducted in displacement control ($v = 0.3 \frac{mm}{min}$) and the settled load path involves a load-unload cycle for the correct evaluation of the Young modulus.

As a matter of fact, especially for compression tests, the first part of the curve is highly non-linear due to the contact between plates and lattice surfaces. Figure 3-6 shows, as example, a focus of such non-linearity taken from one compressive Diamond homogenised stress vs strain curve.

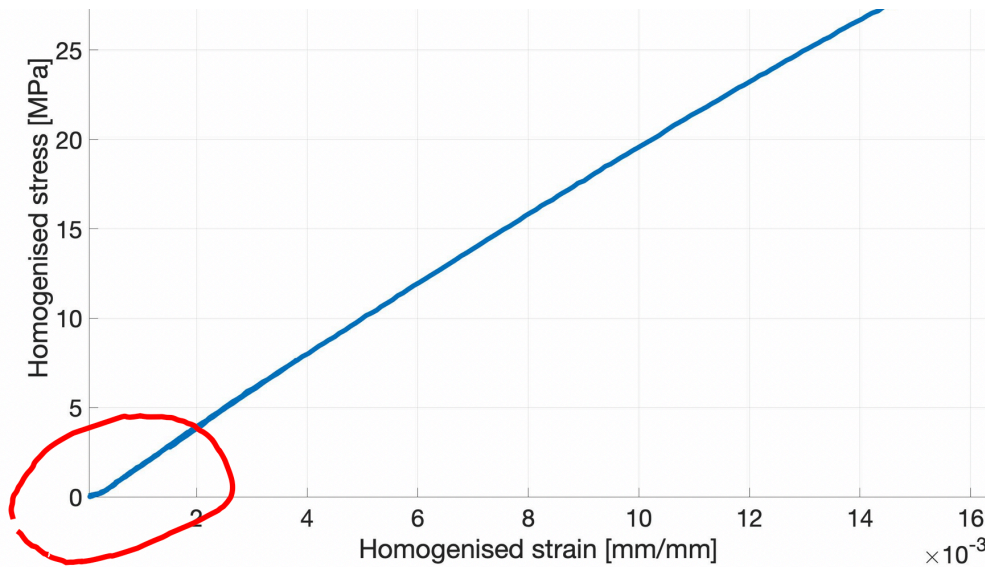


Figure 3-6: Example of initial non-linear trend of compressive homogenised stress vs strain curve

The same qualitative load path has been assigned also to tensile tests: in this case the initial non-linear trend is lower.

Table 9 and Table 10 summarise the load history settled for each test and each specimen.

Compression Absolute value [N]

structure	Load ↑	Unload ↓	Load ↑	Unload ↓	Load ↑
DIA	50 - 500	500 - 50	50 - 950	950 - 350	350 - failure
TET	50 - 500	500 - 50	50 - 3000	3000 - 1000	- failure

Table 9: load path of compression tests

Tension Absolute value [N]

structure	Load ↑	Unload ↓	Load ↑
DIA	0 - 1000	1000 - 500	50 - failure
TET	0 - 3000	3000 - 100	100 - failure

Table 10: load path of tension tests

As it can be seen from Table 9, in compression, an extra load-unload cycle is performed at the beginning for machine stabilisation. Different values have been chosen for load and unload starting points among the two structures because they have different expected numerical mechanical properties that are discussed in detail in chapters 4 and 5.

3.3 Results

For each specimen, loads and strains, thanks to the application of virtual strain gauges on the speckle, have been extracted from GOM software and put into arrays for post-processing.

Different strain gauges have been positioned from left to right on the speckle of every specimen to evaluate if some dependency exists between E and strain gauge position. Figure 3-7 visualises how different strain gauge has been placed on each specimen.

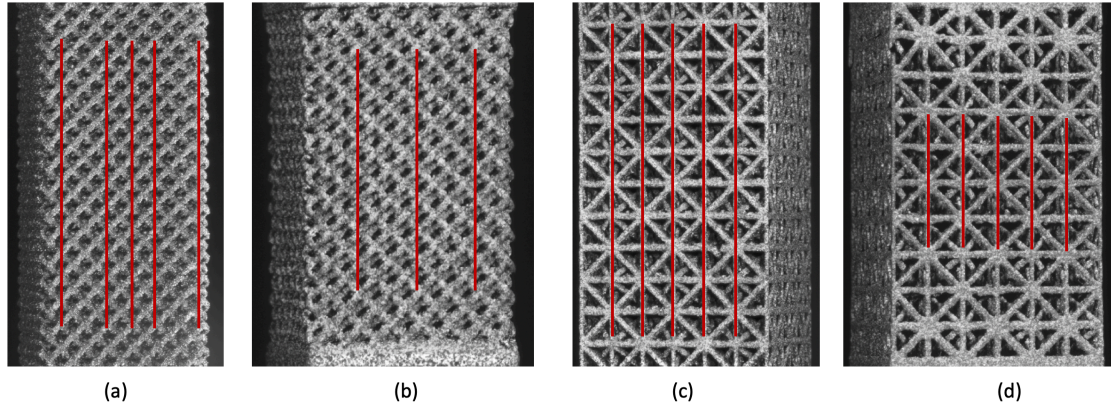


Figure 3-7: Positioning of every strain gauge. (a) compressive Diamond; (b) tensile Diamond; (c) compressive TET; (d) tensile TET

By means of a Matlab code, the homogenised stress-strain curves averaged between each strain gauge has been plotted and the values of Young modulus, yield stress and ultimate stress have been computed.

About the extraction of data from GOM, whereas strains are already provided in the homogenised form, it is necessary to divide the load times the cross section of the specimen to compute homogenised stress; in symbols:

$$\varepsilon = \frac{\Delta l}{l_{sg}}$$

$$\sigma = \frac{F}{A_{lattice}}$$

Where $A_{lattice}$ is the area of the projection of the lattice cross section and l_{sg} is the length of the virtual strain gauge. A Matlab code has been used for the processing of all experimental data. In order to perform a correct estimation of E, a linear interpolation has been made on the 60 % central part of the unloading branch appositely realised; with reference to Table 9, the unloading branches considered for compression are between 950 – 350 N for Diamond and between 3000 – 1000 N for TET.

Regarding the estimation of yield stress, the Rp02 definition has been adopted; the Matlab function 'intersections' has been used to evaluate the point of intersection between the Rp02 line and the homogenized stress strain curve.

UTS and UCS has been simply determined taking the highest value of each stress strain curve. Finally, images of the broken specimens extracted from GOM are described.

3.3.1 Diamond

Six specimens of Diamond type, three in tension and three in compression have been tested. Starting from compression, Figure 3-8 shows the average homogenised stress strain curves of the three compression tests. (exp 1, exp 2 and exp 3).

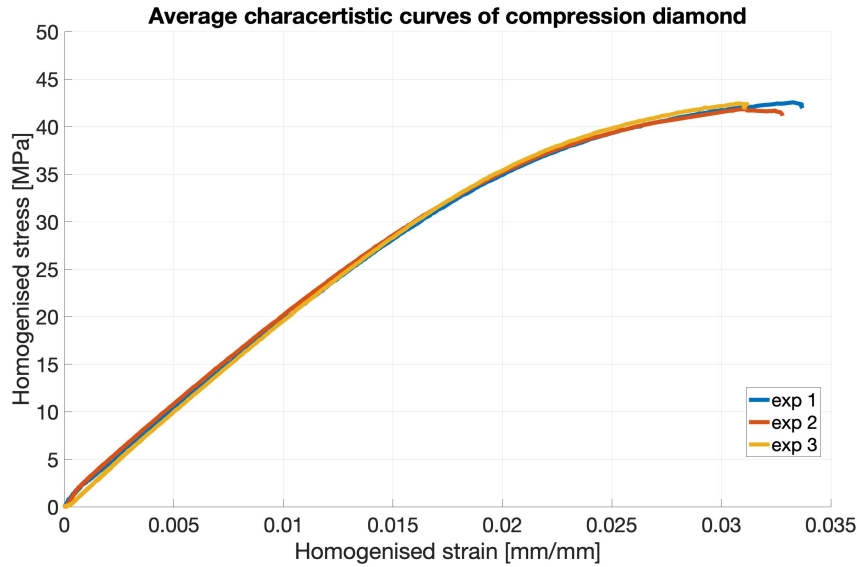


Figure 3-8: homogenised average stress strain curves of diamond for each compressive test

As can be seen from the picture, the three curves are very close to each other and so no important deviations in manufacturing quality nor in experimental deviation occurred.

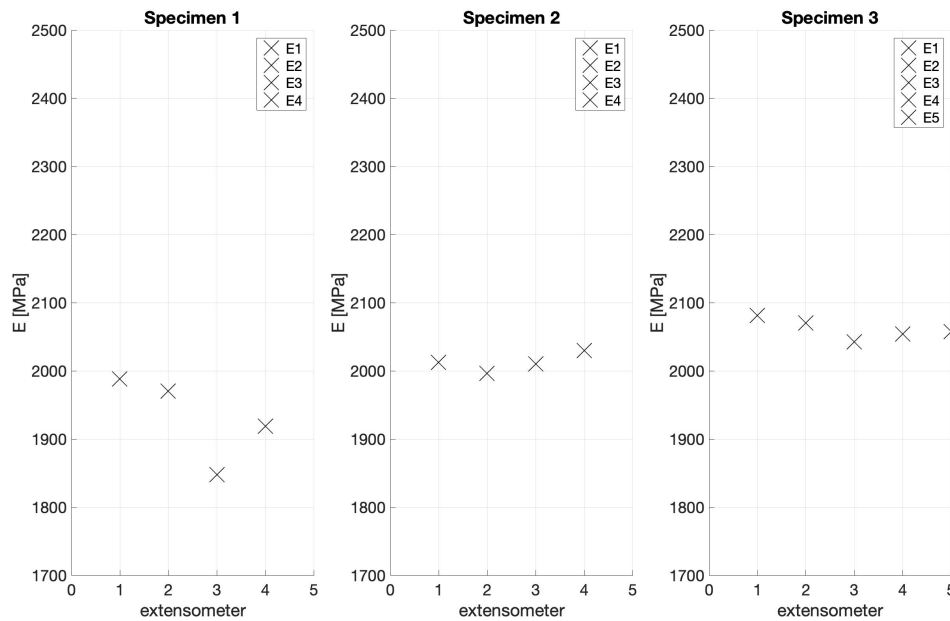


Figure 3-9: Trend of Young modulus in compression for strain gauge from left to right

Figure 3-9 depicts how the elastic stiffness changes from the left to the right of the speckle (E1 refers to left extremity and E4/E5 to right extremity). For the first two samples only four points could be evaluated because of an imperfect realisation of the speckle; it is worth pointing out that the realisation of a good quality speckle on Diamond structure is not easy since the latter does not possess a flat and smooth surface. Apart from E3 of the first sample, for which such a lower

value can be due to measurement noise or excessive imperfection of the speckle in that specific portion, the trend is substantially uniform.

Regarding tension tests, the same type of charts like the ones for compression have been obtained and extracted from Matlab. Figure 3-10 is about the homogenised tensile stress vs strain curves, again the scatter between the three tests is small, this confirms that the manufacturing has been successful and constant also for the tension specimens.

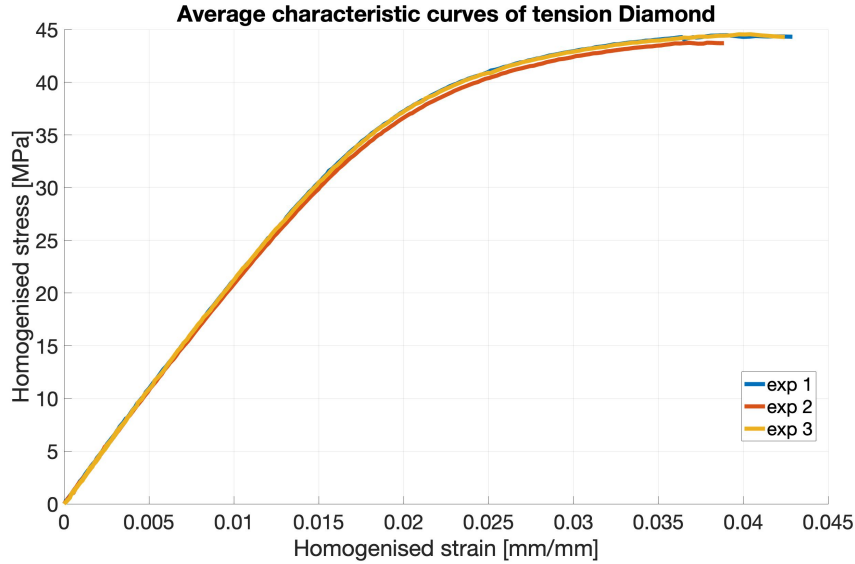


Figure 3-10: homogenised average stress strain curves of diamond for each tensile test

Only three virtual strain gauges have been positioned on the central part of speckle of the tensile specimens because of the same problems, already discussed, with its realisation. The trend is visualised in Figure 3-11. In this case the points are quite sparse and no significant dependency with the strain gauge position is observed.

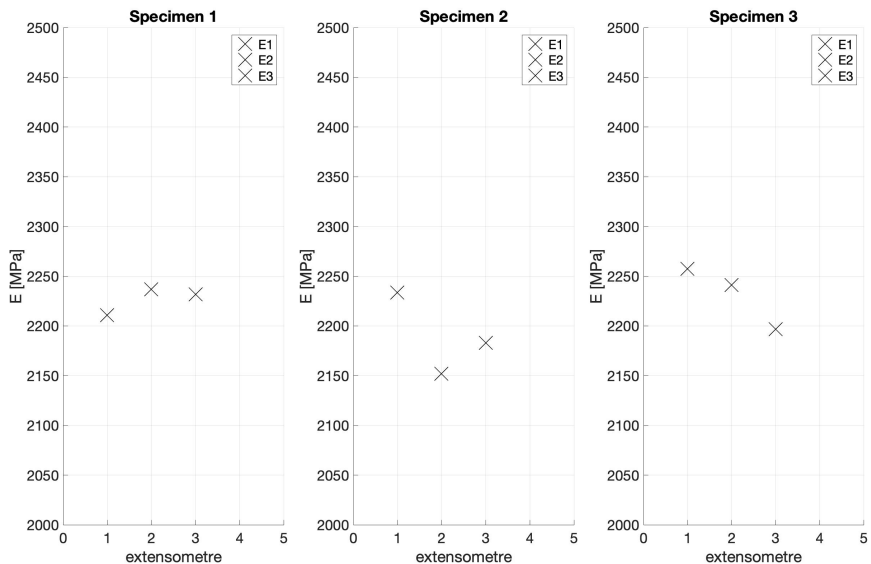


Figure 3-11: Trend of Young modulus in tension for strain gauge from left to right

In general terms, a higher number of tests and a higher effort in the obtainment of a better speckle could add information about the relation between strain gauge position and Young modulus; indeed, it is not purpose of this work to enter in detail of this topic.

The average values of E , σ_y and Ultimate stress for tensile and compression tests are inserted for comparison in Figure 3-12.

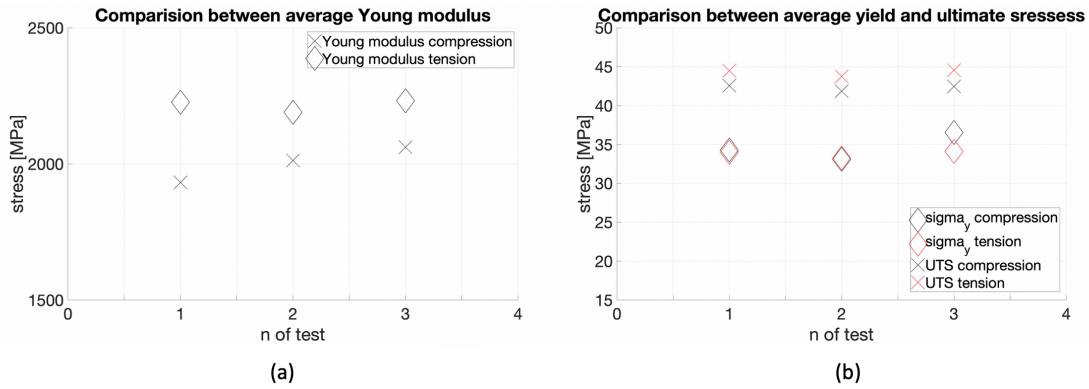


Figure 3-12: Comparison between tensile and compressive tests: left (a) average Young modulus and right (b) average yield stress and UTS

As far as Young modulus go, a difference of about 200 MPa is observed between compression and tension, this is generally due to non-perfect contact between skins and compression plates given by the fact that the polished surfaces of the skins are not perfectly plane, as a matter of fact, compressive and tensile elastic stiffness are generally expected to be equal on equal terms. The yield stress is substantially the same for the first two tests and slightly higher in compression than tension for the third, the discrepancy is small and might be due to measurement noise. Finally, ultimate tensile stresses are higher than compressive ones; such a difference might be caused by an earlier strain failure of compression specimens (around 0.035 mm/mm) respect to the one of tensile specimens (around 0.045 mm/mm). All the experimental results about Diamond are summarised in Table 11 and the average compression and tension curves are compared in Figure 3-13.

Test number	E tensile [MPa]	E compressive [MPa]	Compressive σ_y [MPa]	Tensile σ_y [MPa]	UCS [MPa]	UTS [MPa]
N° 1	2226	1931	34.2	34	42.55	44.46
N° 2	2189	2012	33.08	33.22	41.85	43.75
N° 3	2231	2061	36.54	34	42.43	44.55
Mean value (μ)	2216	2001	34.63	33.77	42.28	44.25
Standard deviation (σ)	65.54	23.06	1.75	0.47	0.38	0.44

Table 11: Resume of experimental values of Diamond averaged between each strain gauge.

Figure 3-14 visualises the fracture behaviour of Diamond specimens in compression. The failure is featured by a shear band with inclination smaller than 45° in the lower part of the structure; a similar failure behaviour was observed in the work of [15]. The image (b) of Figure 3-14 represents the frame at which the test was stopped. Red lines on frame (a) of all the pictures show where the five virtual strain gauges have been positioned (for test number one and two of Diamond compressive tests, the missing strain gauge is number four from left to right).

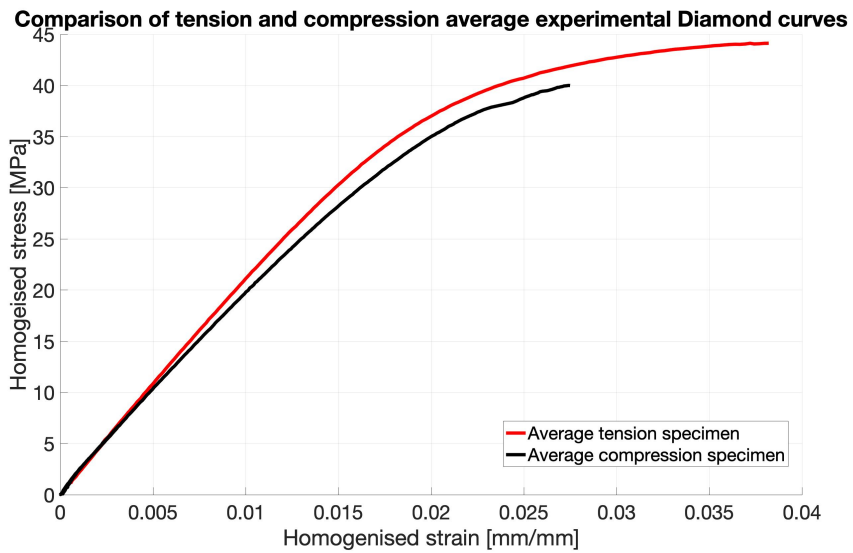


Figure 3-13: Average tension and compression Diamond curves

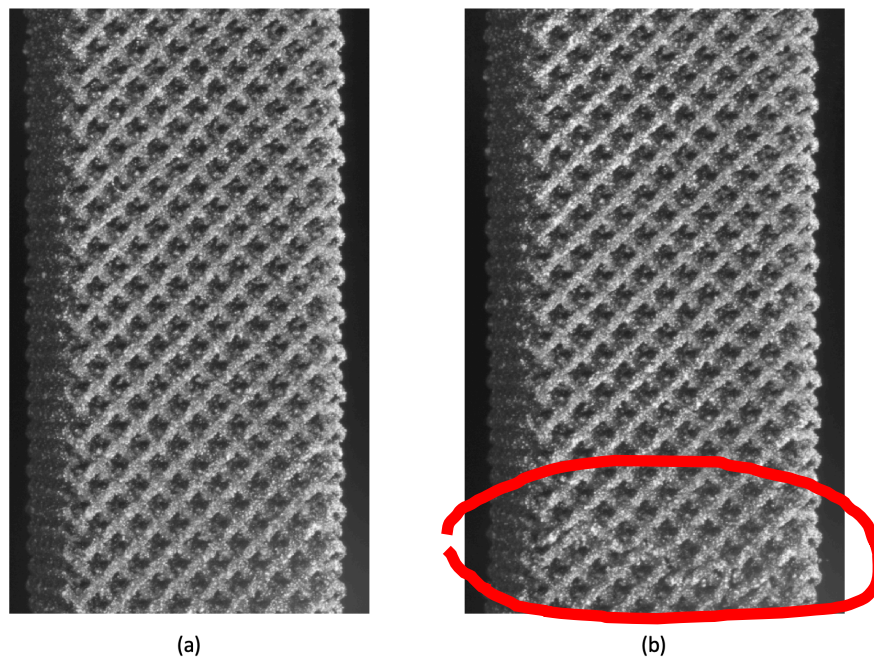


Figure 3-14: compressive deformation of Diamond: (a) is the undeformed shape, (b) the deformed shape

A Similar fracture behaviour is possessed by the specimens in tension; in this case the shear band has a higher inclination of 45° and a clear detachment can be noticed due to the nature of the test. The picture is shown in Figure 3-15, once again, frame (b) is the one at which the test was stopped.

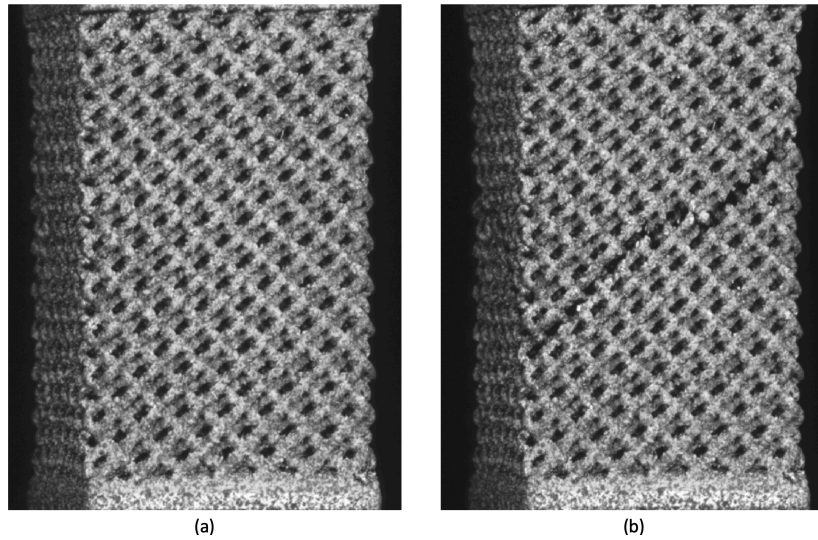


Figure 3-15: tensile deformation of Diamond: (a) is the undeformed shape, (b) the deformed shape

3.3.2 Tetrahedron

From a preliminary visual analysis, TET tension specimens came out of the manufacturing process with defects on some horizontal struts being these lasts already broken. Since this issue is expected to bring about an important underestimation of the mechanical properties, just an exemplary specimen has been tested in tension. With respect to compression, two experiments have been carried out.

The homogenised stress vs strain curve in tension is depicted in Figure 3-16.

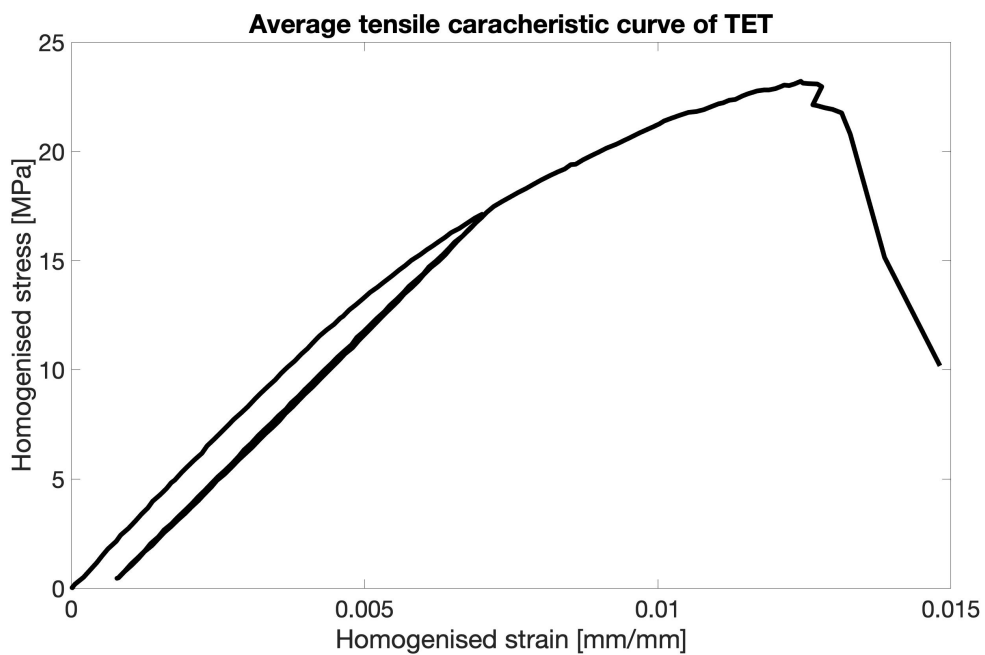


Figure 3-16: Tensile homogenised average stress vs strain curves of TET

It can be noticed from the chart that the strength of the specimen is lower than the as-designed one. As a matter of fact, the unload reload has been designed to be in the linear part of the curve based on the predicted ideal yield, in reality, it starts when the curve has already become non-linear. The analysis of the Tomography and the FE simulation of the real reconstructed cell developed in chapter 5 will provide some further explanations. Despite the specimen has been designed with struts of increasing diameter close to the grasping thus expecting failure in the central part of the specimen, failure occurs near the area of defected struts: this is the unequivocal hint that the failure properties (UTS and σ_y) of the specimen are lowered by the presence of the defects. This statement is visually demonstrated in Figure 3-18 where images from the DIC are shown: frame (a) refers to the beginning of the test and frame (b) to when the experiment was stopped. For this reason, yield stress and UTS are considered unreliable and not worth of further analysis. Nevertheless, being the strain gauge positioned in the central part of the specimen far from the defected area, the value of Young modulus could be valuable and is reported in Figure 3-17. The variation of E along the section is quite higher respect to the compression (Figure 3-20), the cause could be imputed to the initial defects or to measurement noise.

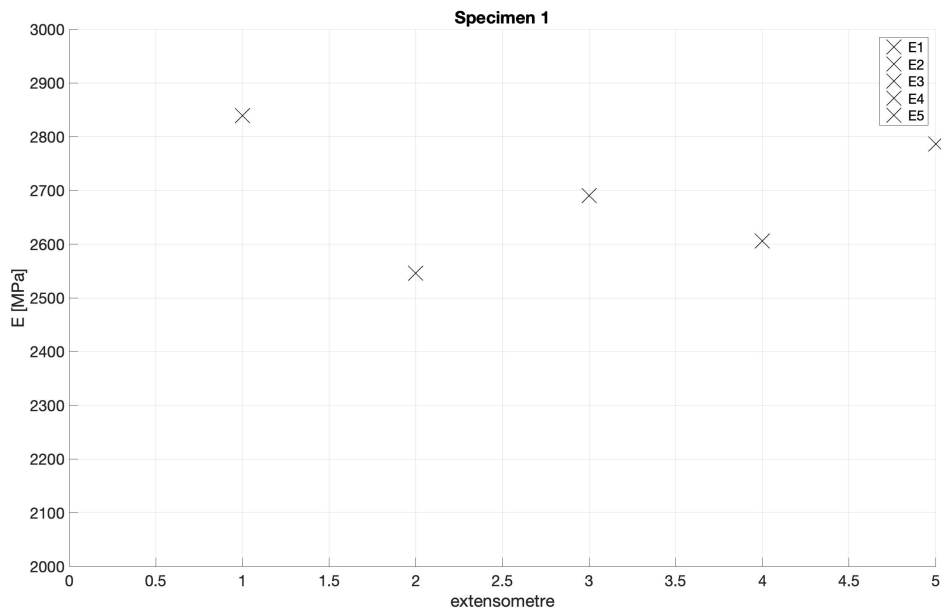


Figure 3-17: Trend of TET Young modulus in tension for strain gauge from left to right

Moving to the outcome of compressive tests, in Figure 3-19 the homogenised compressive stress vs strain curves are visualised.

A non-negligible difference in the strain at failure can be noticed between the two curves, as well as difference in Young modulus, this latter might be caused by a different contact between specimens and plates among the two tests.

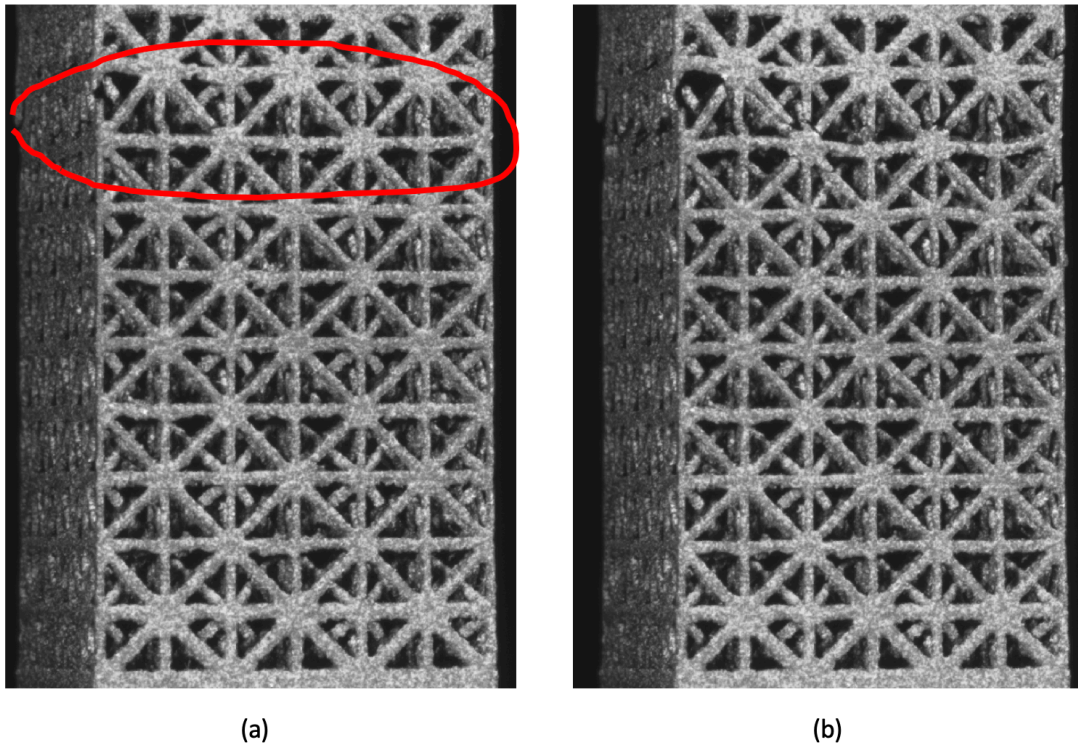


Figure 3-18: tensile deformation of TET: (a) is the undeformed shape, (b) the deformed shape. The red area highlights the defected struts.

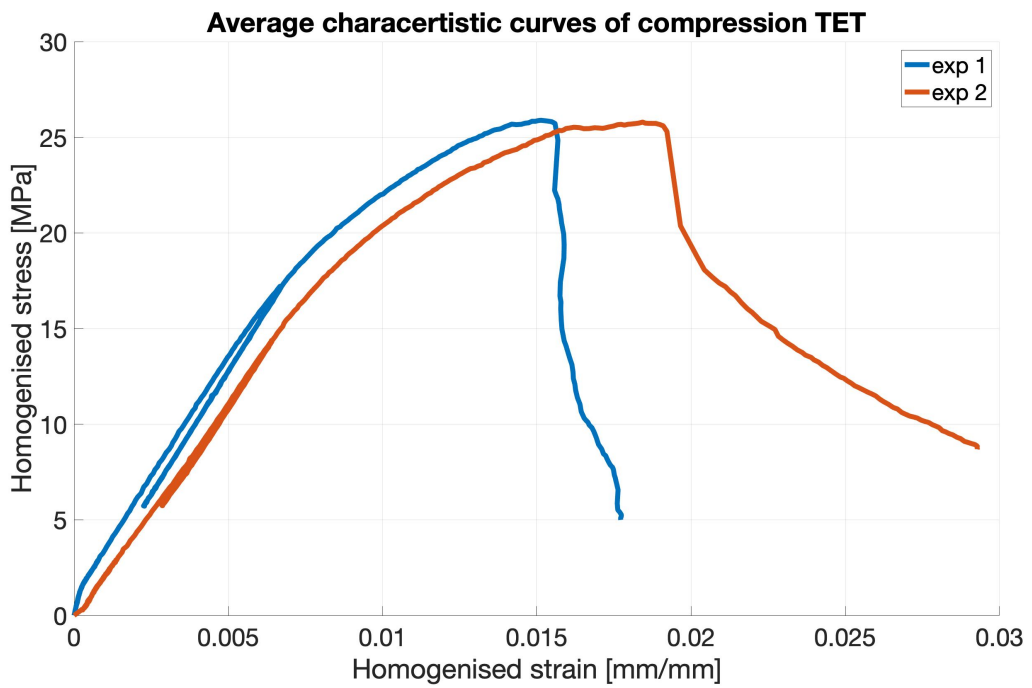


Figure 3-19: homogenised average stress strain curves of TET for each compressive test

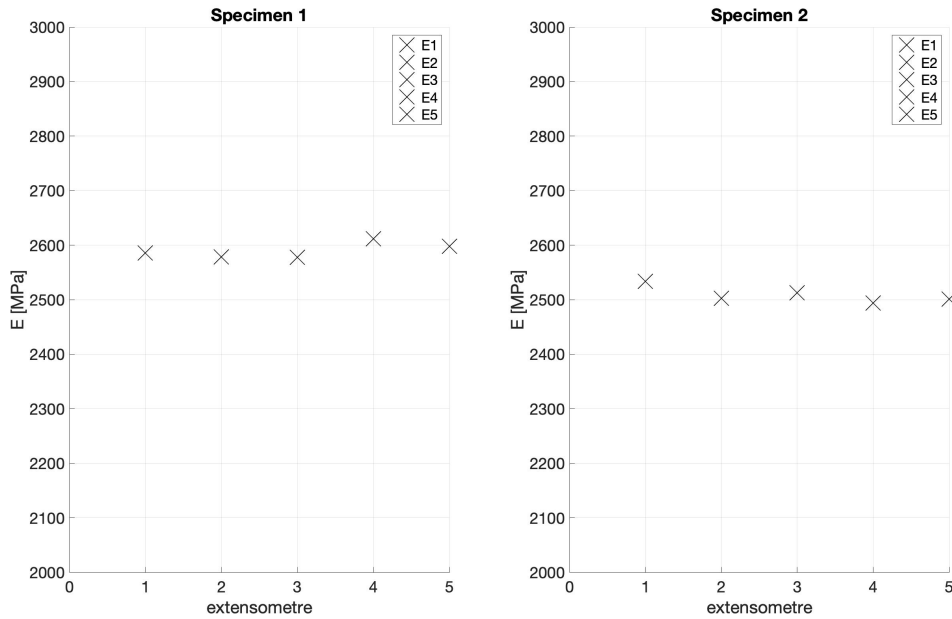


Figure 3-20: Trend of TET Young modulus in compression for strain gauge from left to right

Like it happened for Diamond structure, also for TET, different virtual strain gauges have been attached to the speckle from left to right with Aramis software to evaluate, from a preliminary point of view, the dependency of E with the strain gauge position. The results are shown in Figure 3-20; a uniform trend is observed for both specimen. Figure 3-21 depicts the two values of yield stress and UCS. Following the same dissimilarity already pointed out for Young modulus, the second specimen has a lower yield stress than the first.

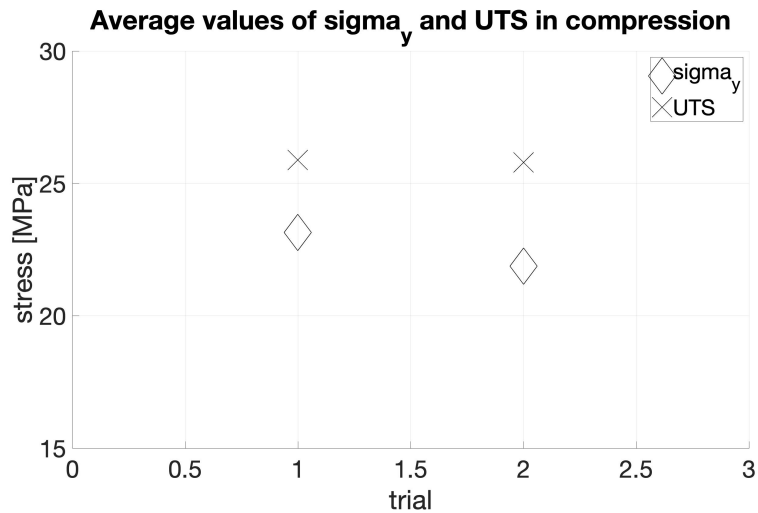


Figure 3-21: UCS and σ_y for TET compressive tests

The values of TET compressive and tensile tests are summarised in Table 12. The mechanical properties evaluated are much lower than the numerical ones: for example, looking at Young modulus, the experimental one is nearly 50% lower. This huge difference might be justified by a discrepancy between the densities of real and ideal specimens (being the latter lower) and by other geometrical details which demonstrates that the manufacturing tolerances are high; a focus on this aspect is carried out in chapter 5 where the tomography of the real structures is analysed.

Test number	E compressive [MPa]	E tensile [MPa]	Compressive σ_y [MPa]	UCS [MPa]
N° 1	2590	2693	23.15	25.89
N° 2	2509	-	21.88	25.8
Mean value (μ)	2549	-	22.51	25.84
Standard deviation (σ)	57.66	-	0.9	0.06

Table 12: Resume of experimental values averaged between each strain gauge of TET.

The average Young modulus of the tensile test is slightly higher than the ones of compression presented in Table 12, such aspect can be due to the non-perfect contact between compression plates and skins; for this reason, the tensile E is considered more reliable than the compressive one.

Even though the values of TET compressive tests result in lower properties than the as-designed ones, they are representative of the as-manufactured specimens. It is indeed interesting to look at the deformed shape of the samples to gain some qualitative information about their failure mode.

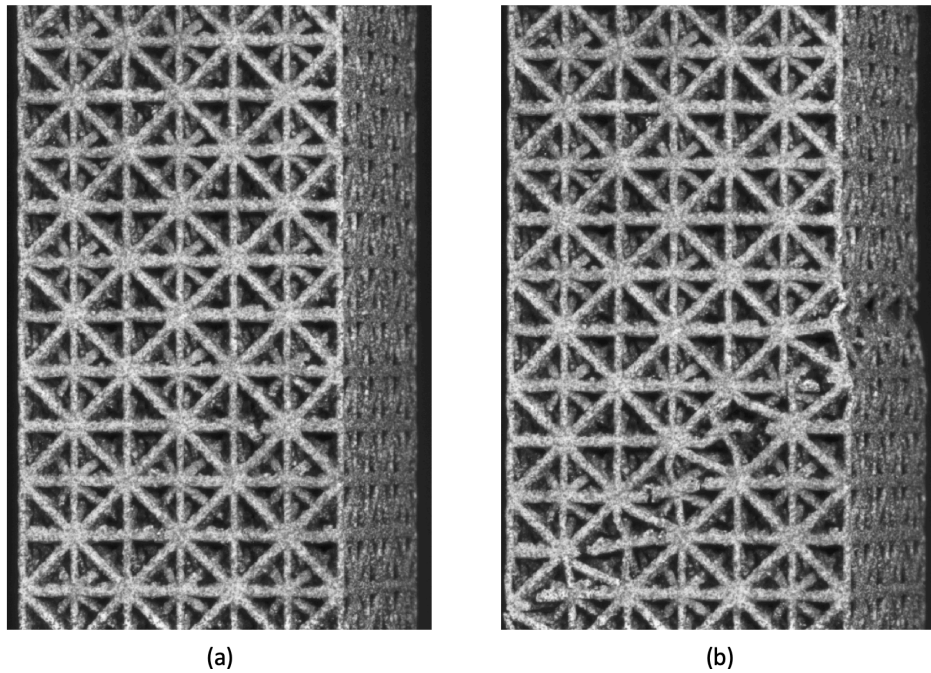


Figure 3-22: compressive deformation of TET: (a) is the undeformed shape, (b) the deformed shape

As Figure 3-22 reports, TET structure failed on a 45° plane and the struts along a horizontal row on the plane partially visible on the right of frame (b) collapsed with a buckling deformation mode.

4. Numerical elastic and elasto-plastic analysis on ideal selected structures

The aim of this chapter is to go deeper in the analysis of the RVE dimensions in linear elastic and non-linear elastoplastic regime and to investigate the difference between the Young modulus of specimens of increasing cross sectional size and RVE specifically to TET and Diamond following with the aspects pointed out in paragraph 1.1.6. What is more, in the definition of the FE models, an effort to substitute homogeneous solid elements with linear beam elements has been made in order to save computational time. The result of this approach as well as its drawbacks are part of the discussion of this chapter too. For all the elastoplastic simulations, a plastic model of 3D printed annealed Ti6Al4V according to the one used in [21] has been used; even if those values refer to tensile properties, they are used in this work also in compressive simulations since no relevant difference between tension and compression is expected for Titanium. The main values of the monotonic curve, extrapolated from the one of Figure 4-1, are in Table 13.

E [GPa]	σ_y [MPa]	ν
112	959	0.34

Table 13: Monotonic mechanical properties of annealed Ti6Al4V

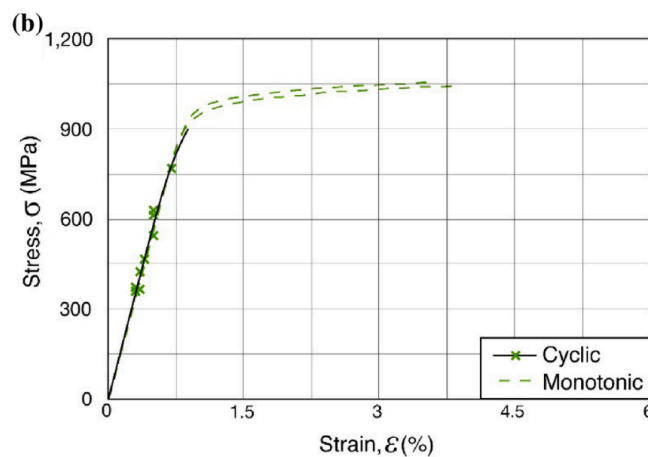


Figure 4-1: Monotonic curve for data extrapolation [21]

The parameters to define the RVE size in linear regime is Young modulus in the sense that the RVE is the one starting to which no difference in E is appreciated if the size of the periodic lattice volume is increased; the same role, in non-linear regime, is played by the trend of the stress vs strain curve and the presence or not of bifurcations. Before going on with the analysis, a short remind of the difference between solid and beam elements is presented.

3D Beam elements

Linear beam elements used in this work fall within the category of 3D line elements. They possess 2 nodes and 12 DOF, 6 for each node of the beam, namely: $u_1, v_1, k_1, \theta_{u1}, \theta_{v1}, \theta_{k1}$ for the first node and $u_2, v_2, k_2, \theta_{u2}, \theta_{v2}, \theta_{k2}$ for the second node, where u, v and k refer to $x, y,$ and z direction whereas $\theta_u, \theta_v, \theta_k$ are the rotations about each correspondent axis. The shape of the section must be defined among several option available in Abaqus. The advantage of using beam elements is that a much lower number of nodes is needed to mesh the same geometry respect to solid elements thus leading to important reduction of computational time. Among their drawbacks they don't account for shear force contribution which brings about an underestimation of the mechanical properties and lead more easily to numerical convergence problems for elastoplastic models. The scheme of the DOF of a beam element is shown in Figure 4-2. In the figure the section shape is not specified and left as the one of a wire, in reality the FE needs the definition of a section to recognize its geometric moments of inertia.

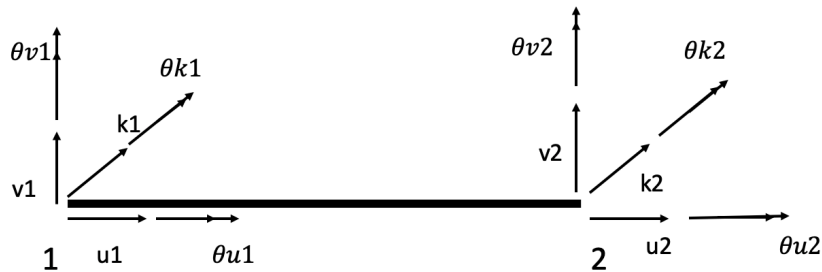


Figure 4-2: Scheme of DOF of a 3D linear beam element

Tetrahedral solid elements

Tetrahedral elements owe their name to their shape, as visualized in Figure 4-3. They are used to mesh any complex 3D geometry and possess a number of DOF which depends on their typology but generally higher than beam ones. The difference with respect to beams is that, each node owns only the three translational DOF and do not possess any rotations. What is more, that they can account to shear force enabling a better estimation of the mechanical properties of the real component. The price to pay is a much higher computational time for the simulations.

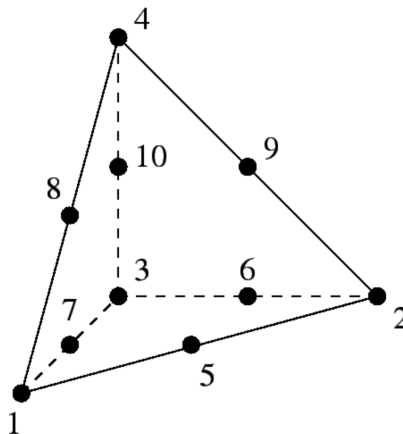


Figure 4-3: Ten node tetrahedral element

4.1 Linear regime

All the models realised to study the linear regime consider the assignment of linear elastic properties to the material and the only output is Young modulus.

4.1.1 Tetrahedron

Regarding the dependency between linear RVE size and Young modulus, no relation has been observed neither with solid nor with beam elements. Simulations have been run on 2x2x2 and 4x4x4 configuration with solid and on 2x2x2, 4x4x4 and 6x6x6 configuration with beam and the resulting Young modulus always remain equal to the base 2x2x2 size. It is therefore possible to conclude that the smallest RVE size in linear regime is the 2x2x2 periodic unit for TET.

Once the linear RVE size has been defined, the difference between E of specimen and of RVE has been investigated. To this extent, in Abaqus CAE, solid elements are used to compare the elasticity of the RVE with the one of the specimen used for compressive experiments. TET unit cell has dimension 2x2x2 (see paragraph 2.1) whereas a portion of the specimen equal to 1/8 has been modelled to reduce the computational time. As for loads and displacements, periodic BC for symmetric structures (see paragraph 2.2.1 for the BC description) has been assigned to the 2x2x2 unit and planarity has been imposed to the non-boundary faces of the 1/8 portion of specimen, namely the upper, the lower and two adjacent on the side. To impose planarity in Abaqus the x-symm, y-symm and z-symm constraints have been imposed on the faces normal to x, y and z respectively and with open struts. In doing so, the lattice behaves as if it was replied in the three directions thus leading to the complete specimen. Both simulations are carried out with compressive imposed displacement of 1 % of the vertical length and tetrahedral quadratic elements. In Figure 4-4 the 1/8 specimen is shown. The outcome of the analysis is such that:

$$E_{solid,specimen} = 4841 \text{ MPa}$$

$$E_{solid,RVE} = 4185 \text{ MPa}$$

$$\frac{E_{solid,specimen}}{E_{solid,RVE}} = R_{s,RVE} = 1.157$$

The parameter $R_{s,RVE}$ has been defined “ad hoc” for this study: ‘s’ stands for ‘specimen’. The difference among the two values can be imputed to the extra stiffness given by the two faces of the 1/8 specimen with closed struts, phenomenon known as “boundary effect”. In paragraph 4.1.2 a detailed explanation of this phenomenon is presented

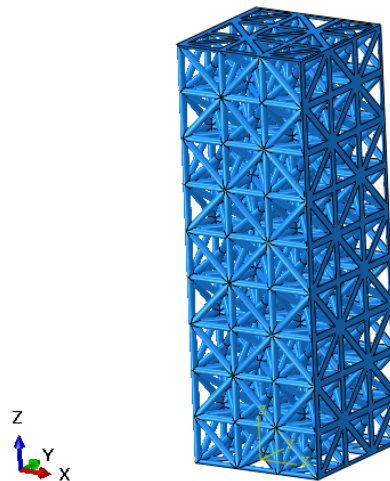


Figure 4-4: Picture of the 1/8 solid specimen for FE analysis

The overmentioned boundary effect can be reduced if the dimension of the specimen section increase adopting the same approach of [20]. In this work, to save computational time, the same type of analysis has been carried out with beam elements. Before doing this, in order to establish a parallelism between solid and beam elements and to evaluate if and how much $R_{s,RVE}$ changes, the two simulations described above have been reproduced with beams.

To this extent, the entire specimen (instead of 1/8) has been modelled since the expected computational time is lower. BC can be seen in Figure 4-5: encastre has been put to the lower face to simulate the presence of the skin which, with good approximation, possess infinite stiffness respect to the rest of the structure thus preventing lateral movements. Compressive load has been given with a reference point kinematically coupled with all the nodes of the upper face. What is more, because in real compressive test the rotation of the upper face is approximately null, the rotations of the reference point have been constrained too. A circular section has been assigned to every beam of the specimen.

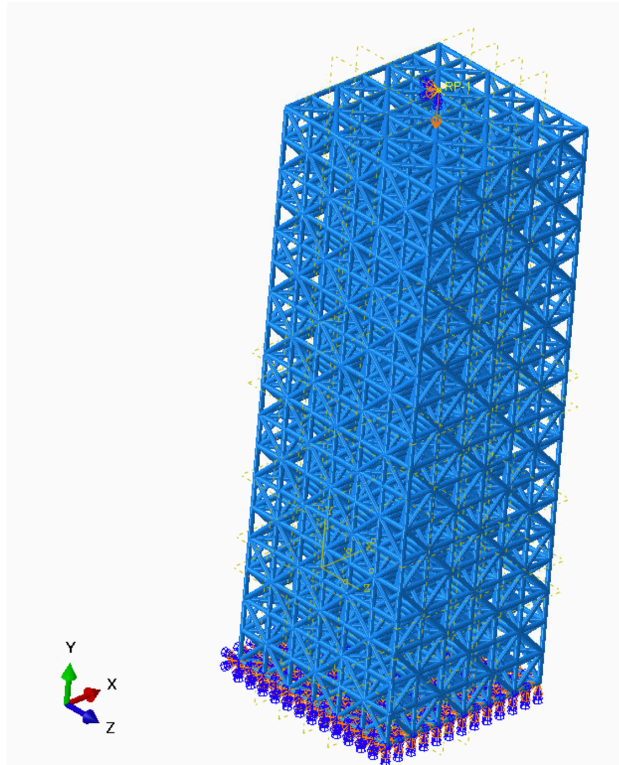


Figure 4-5: TET specimen with beam elements

Moving to the beam modelling of the RVE with open struts, it is possible to notice that the struts on the six faces have a semi-circular shape and the struts at the corners are $\frac{1}{4}$ of a circle but, because Abaqus does not allow to assign sections with semi-circular and $\frac{1}{4}$ circle shape, a specific strategy has been implemented as discussed below.

Bending and axial stiffness of a beam section depend on its area and on the two moments of inertia, therefore, it is possible to obtain the same stiffness with a different shape yet imposing the same area and same inertias.

In Figure 4-6 the RVE beam model with opportune sections is shown, the BC imposed are the same as the ones of the solid model. The only difference respect to solid elements, is that beams have rotations and it is therefore necessary to set the in-plane rotations of the upper surface null.

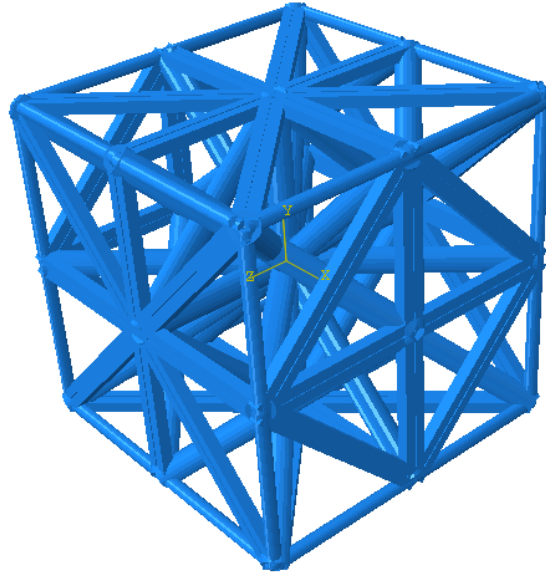


Figure 4-6: Tetrahedron 2x2x2 RVE with beam elements

The FE results are:

$$E_{beam,specimen} = 4246 \text{ MPa}$$

$$E_{beam,RVE} = 3550 \text{ MPa}$$

$$\frac{E_{beam,specimen}}{E_{beam,RVE}} = R_{s,RVE} = 1.18$$

According to $R_{s,RVE}$, the boundary effect is slightly more pronounced for beam than for solid elements. Another comparison between beam and solid regards the ratio of specimens and RVEs:

$$\frac{E_{solid,specimen}}{E_{beam,specimen}} = 1.14$$

$$\frac{E_{solid,RVE}}{E_{beam,RVE}} = 1.16$$

The outcome is that beam elements can be used to substitute solid elements for the specimen modelling with an error accounted by the ratio $\frac{E_{solid,specimen}}{E_{beam,specimen}} = 1.14$. Five different specimen configurations with one row and imposed vertical periodicity with PBC for symmetric structures on upper and lower faces only (to save computational time and memory) have been modelled: the cross section has been progressively increased with 4x4, 6x6, 8x8, 10x10 and 12x12 periodic units as depicted in Figure 4-7 to evaluate the trend between E and RVE size. Regarding the section assignment, each section reproduces the one of a specimen with closed struts on the lateral sides, therefore, the open strut configuration (with I shaped section) has been attached only to the surfaces normal to the vertical direction. The result of the investigation is resumed in Figure 4-8 and quantitative values in Table 14.

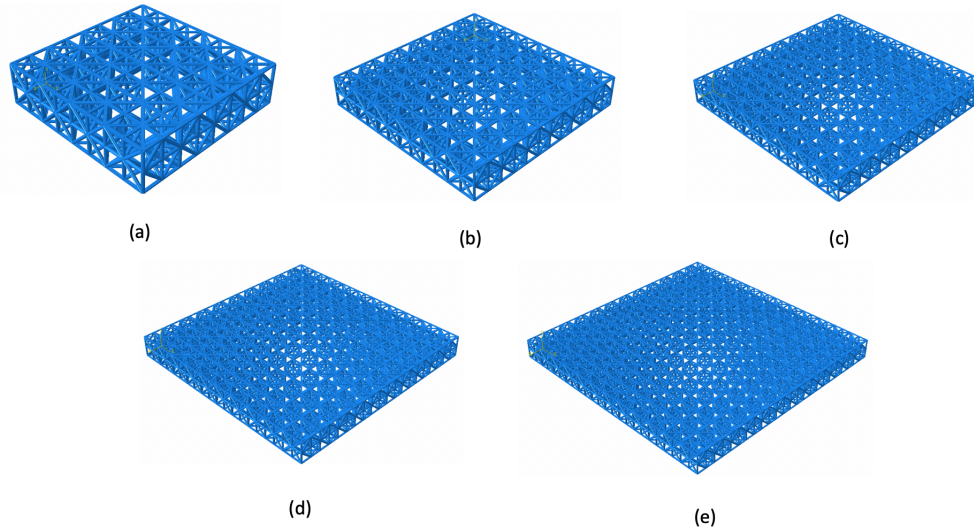


Figure 4-7: Specimen section of increasing dimensions: (a) 4x4, (b) 6x6, (c) 8x8, (d) 10x10, (e) 12x12

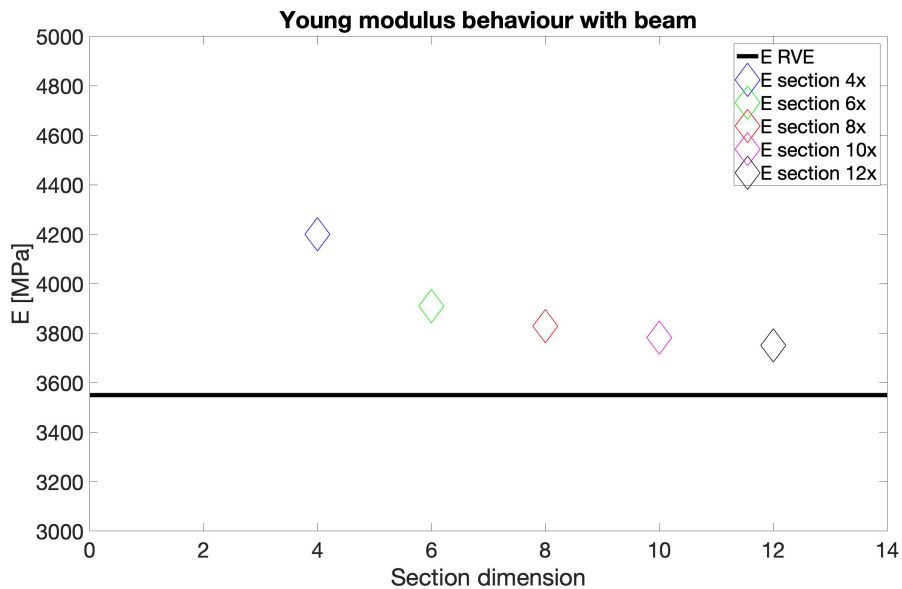


Figure 4-8: Young modulus behaviour with increasing TET specimen section

	Section 4x4	Section 6x6	Section 8x8	Section 10x10	Section 12x12	RVE
E [MPa]	4200	3909	3829	3782	3751	3550
Error %	15.4	9.1	7.3	6.1	5.3	-

Table 14: Boundary effect on TET modelled with beams

The points on the chart confirm that the boundary effect reduces as the size of the specimen increase and, with 12x12 section, still a deviation is present, and the reduction of E with the increase of section is very slow. Therefore, a certain gap between specimen and periodic unit cannot be covered unless the specimen is designed with very big dimensions. Since it is not feasible to print such big specimens because it would be expensive from manufacturing and experimental point of view (a huge compression machine capable of supply thousands of KN

would be needed), a certain error is accepted. In this case, with a 12x12 section, the error is 5.3 %.

4.1.2 Diamond

If compared to tetrahedron, Diamond has an important difference which affects the numerical modelling and the possibility of using beam elements the same way it has been done for TET. As discussed in paragraph 2.2, because Diamond does not have any planes of symmetry, general PBC with Homtools must be imposed to model the RVE and obtain the periodicity of the unit cell. Unfortunately, it has been noticed that Homtools commits mistakes, when this specific geometry is modelled with beams, in coupling the displacements of some nodes of opposite faces thus leading to non-reliable results. The problem is explained in detail with the help of Figure 4-9 on a couple of nodes taken as example; (also other nodes have the same problem).

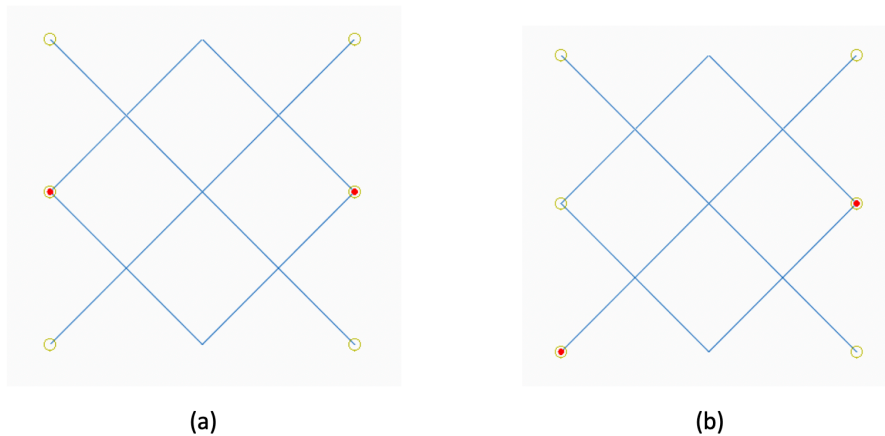


Figure 4-9: Mistake in the coupling of Diamond structure with Homtools

In picture (a), the two red points represent a pair of nodes whose displacements should be coupled to achieve periodicity; in reality, Homtools, couples the nodes highlighted in picture (b) thus bringing about wrong results. A possible way to bypass this mistake is to develop a Matlab code which performs the same work of Homtools making sure that the coupling of each node is correct. Because this procedure is not trivial and time consuming, it has not been implemented in this work and is suggested as future development. For all these reasons, the dependency of the RVE size with Young modulus and the impact of boundary effect is evaluated with solid elements only. Identically to TET, also for this structure it is confirmed that the linear RVE has the same dimension of the periodic unit which is 1x1x1.

Moving to the boundary effect, four reduced specimen models with 3x3, 4x4, 6x6 and 7x7 cross sections and 6 vertical cells have been considered. The nomenclature 'reduced' refers to the fact that every configuration is smaller than the 3D printed specimen which is 7x7x28. The motivation on top of this is merely to reduce the computational cost. Indeed, relevant deviations are not expected since strains are measured at mid height and the effect of the specimen's height is not so relevant. For each model encastre has been applied to the lower face and a compressive displacement of 1 % has been assigned to the upper face. Another way could be to model one single cell in vertical direction and couple the upper and lower face with equations from Homtools so to impose PBC conditions, this solution has been avoided because the enormous number of equations to set (3 for each node of the surface) would take a higher total computational time.

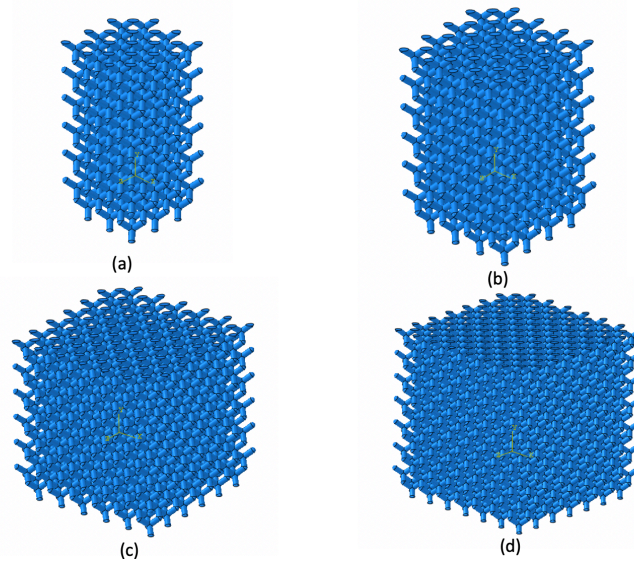


Figure 4-10: Ideal Diamond specimens of different section dimensions: (a) 3x3, (b) 4x4, (c) 6x6 and (d) 7x7

Figure 4-10 shows the four reduced specimens utilised to carry out the analysis. The outcome of Figure 4-11 represents the counterpart of Figure 4-8 specifically to Diamond. The curious aspect is that the boundary effect is opposite respect to TET meaning that the smallest is the section of the specimen and the lower is E. The reason why TET and Diamond show two opposite boundary effects can be explained as follows.

Two simultaneous aspects make the stiffness of the finite specimen different from the one of the RVE: the presence of closed struts on the periphery of the specimen and the fact that a finite specimen does not have any material that somehow provides support out of its boundary. The first contribution increases the stiffness of the specimen with respect to the one of the RVE whereas the second contribution makes it smaller. It follows that, TET possess many struts at the boundary of the cell and the first contribution dominates the second, on the contrary, Diamond does not possess struts at the periphery and the second contribution dominates the first. values of different E of Diamond are in Table 15.

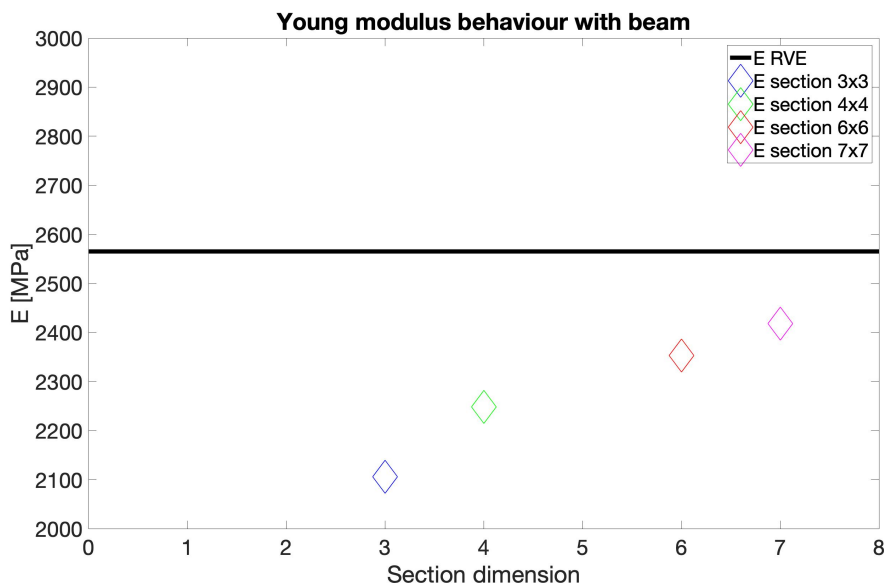


Figure 4-11: Young modulus behaviour with increasing Diamond specimen section

This result is attributed to the different type of geometries among TET and Diamond: the former with vertical closed struts at the periphery of the lattice scaffold that contribute in raising the

strength, the latter without any peripheric struts. In this case, the parameter error is 5.7 for the 7x7 section so the trend for convergence is faster and, therefore, the deviation between RVE and

	Section 3x3	Section 4x4	Section 6x6	Section 7x7	RVE
E [MPa]	2106	2248	2353	2418	2565
Error %	17.8	12.3	8.3	5.7	-

Table 15: Boundary effect on Diamond modelled with solids

specimen is expected to furtherly decrease with an acceptable section size. By the implementation of Diamond beam models, it would be possible to check rapidly and without excessive computational effort when and if periodic unit and specimen gain the same elastic stiffness for greater section sizes thus achieving zero error.

4.2 Non-linear regime

In non-linear regime an elasto-plastic model of Ti6Al4V extrapolated from Figure 4-1 has been assigned to the material properties with the aim of computing the yield stress and studying the shape of the homogenised stress vs strain curve after the yielding.

4.2.1 Tetrahedron

The same structures shown in Figure 4-4 and Figure 4-5 (the former is 1/8 specimen with solid elements and the latter the complete specimen with beam elements) have been simulated in Abaqus adding the elastoplastic model for Ti6Al4V. The outcomes of both deformed shapes confirm what it has been observed also from the DIC images of TET compression tests, namely that the structure undergoes buckling (see Figure 4-12). Moreover, looking at the figure, it can be assessed that the crush takes place on a 45° inclined plane the same as for compression specimen (Figure 3-22). Being buckling a non-linear periodic phenomenon, it is no longer possible to model the RVE with periodic BC for symmetric structures to correctly predict it, on the contrary, general PBC like the ones inserted by Homtools should be used. The motivation is that PBC for symmetric structures impose planarity of the boundary faces of the periodic units preventing them, for example, to have an out of plane buckling wave which could occur in reality as stated by Figure 4-13 where two TET periodic units (1x) have been simulated with either general PBC and symmetric PBC. For the same reason, the prediction of homogenised stress vs strain curve given by the 1/8 specimen with imposed planarity involves some error; as a matter of fact, the introduction of general PBC with homtools would be needed on the cut surfaces but this has been avoided for computational reasons. In general terms, when buckling occurs, several wave lengths featuring the deformation of the buckled system represent possible solutions from a mathematical point of view, but the real system tends to follow the one owing the lower amount of energy. Having said that, it follows that the periodic lattice geometry should be big enough to comprise, inside its domain, at least one period of the lowest energy deformation wave. According to the approach of [18], the minimum size owing the overmentioned property can be figured out by looking when the stress vs strain curves of increasing model dimensions become stable. Such strategy has been used also in this work to try to estimate the non-linear TET RVE size. Two solid TET structures, namely with 1x1x1 (1x) periodic units and 2x2x2 periodic units (2x) have been modelled with general PBC and an imposed displacement of 0.07 times the vertical height; the two homogenised stress vs strain curves have been compared with each other and with the one of the 1/8 specimen in Figure 4-14.

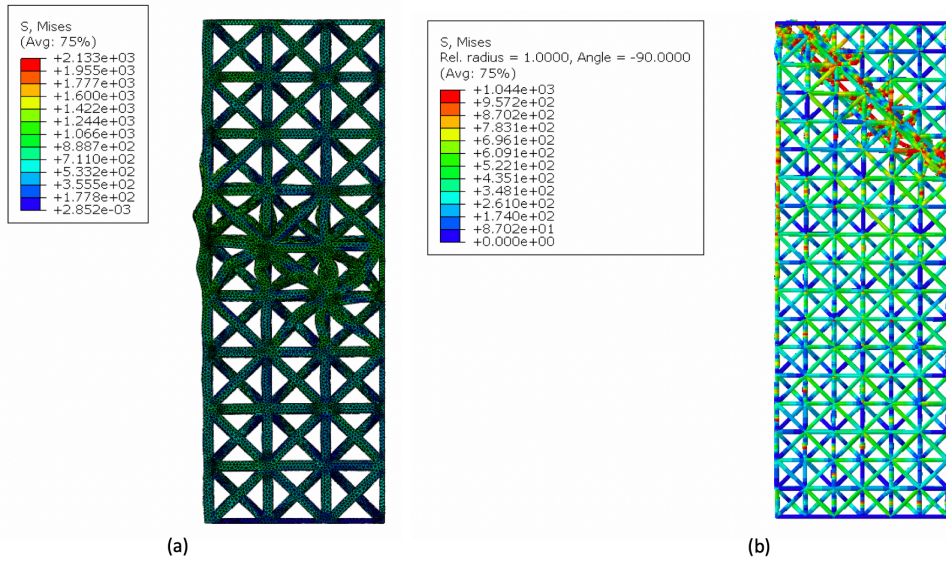


Figure 4-12: TET specimen undergoes buckling; (a) with solid elements, (b) with beam elements

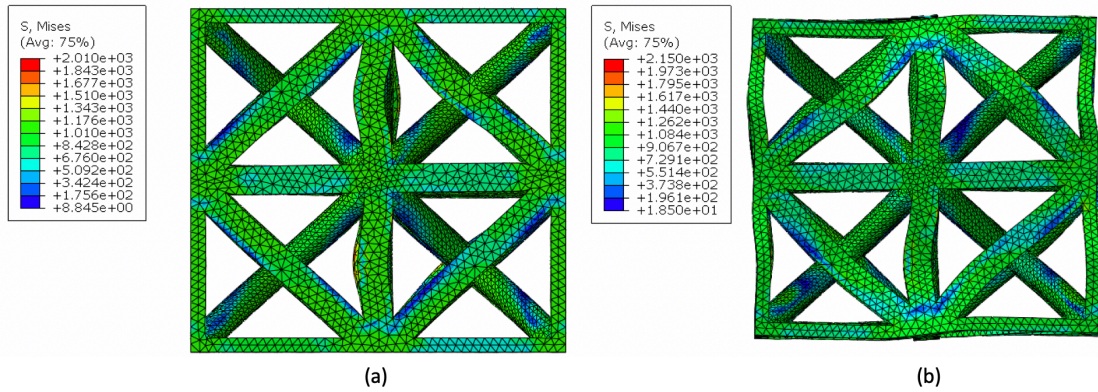


Figure 4-13: Different deformed TET shape between PBC for symmetric structures (a) and general PBC (b)

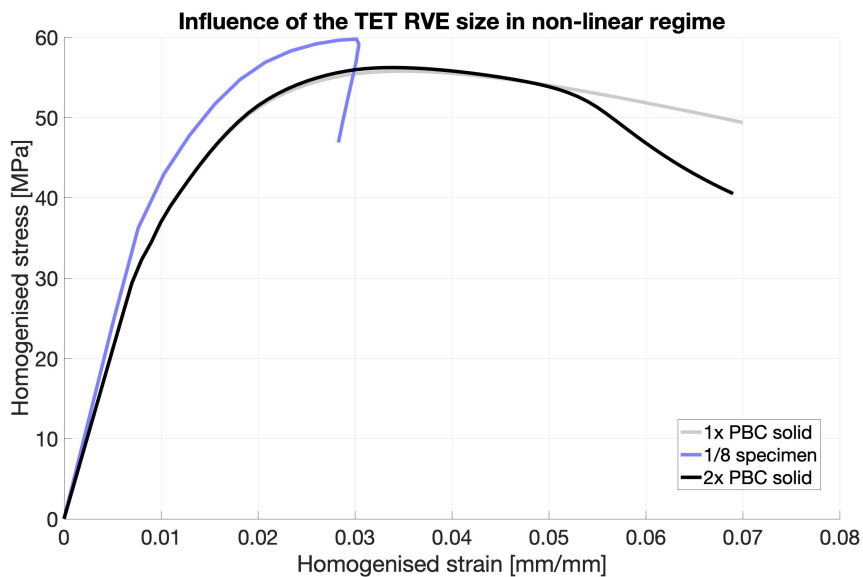


Figure 4-14: Effect of the RVE size on the non-linear part of TET homogenised stress vs strain curve

A bifurcation can be appreciated in correspondence of a strain of circa 0.05 mm/mm and, in line with the expectations, the 2x configuration stands below the 1x following the former a lower deformation energy path as soon as buckling begins. This result is, from a qualitative point of view, in fully agreement with the statements of [18]. The 1/8 specimen model returns a lower buckling strain (≈ 0.03 mm/mm) compared to the two periodic models, this is due to the fact that the former is not representative of the infinite lattice mean and an increased size would move the buckling starting point to the right and close to the 1x and 2x ones. Nevertheless, since neither a higher size specimen nor a higher size periodic model has been created with solid elements for computational cost reasons, an open question remains regarding the dimension of the TET non-linear RVE size. Indeed, the definition of a 3x (or higher) structure could reveal a lower deformation energy and, at the same time, its stress vs strain curve stand below the 2x one. In order to perform an exhaustive analysis and grow with the dimension of the models with reasonable computational cost, the adoption of beam elements could be a solution. Unfortunately, being Homtools ideated for solid elements, it does not bother about the coupling of rotations of correspondent nodes causing wrong results and numerical convergence problems for static general FE simulations with beam. One of the possible future developments of this topic, which has not been performed in this work, might be to add the coupling of rotations to Homtools via Matlab script.

As far as the numerical yield stress prediction goes, it has been demonstrated that PBC for symmetric structures and general PBC can be indiscriminately used to carry out a right prediction. This is demonstrated by Figure 4-15 in which the homogenised stress vs strain curves of 1x and 2x TET models with PBC for symmetric structures have been added to the curves already present in Figure 4-14 where it is possible to see that all the curves are identical up to the buckling activation strain.

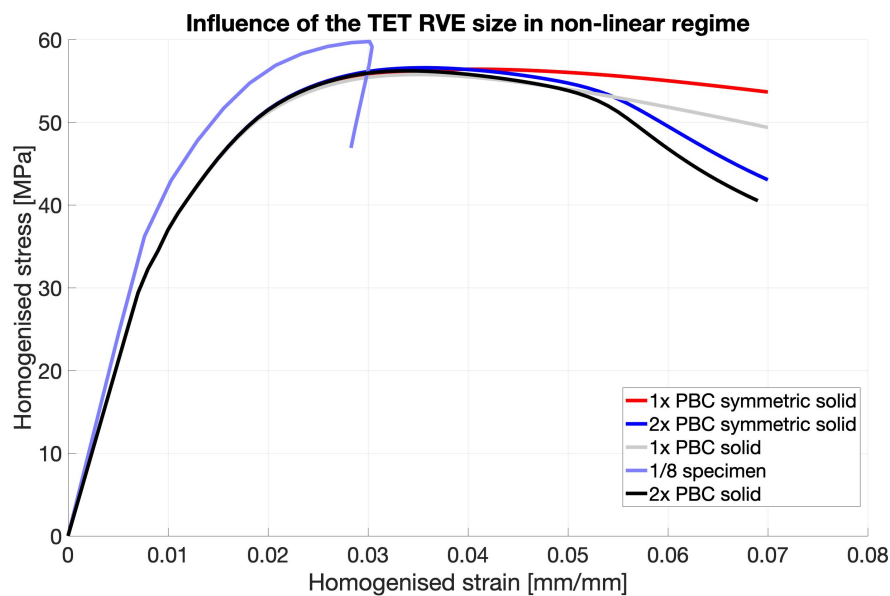


Figure 4-15: Comparison between general PBC and PBC for symmetric structures

4.2.2 Diamond

With reference to the compression tests, it can be assessed that Diamond fails because of a sudden crush of struts disposed on a 45° plane without undergoing buckling. This is not enough to conclude that Diamond as unit lattice shape never undergoes this failure mode, but it is indeed true for geometries with a relatively small non-dimensional strut length λ (known also as slenderness) like the one of this work which is $\lambda = 4.69$. On the basis of this consideration, the RVE size is expected to be equal to the smallest $1 \times 1 \times 1$ periodic unit. To have a confirmation of the overmentioned point, three Diamond models with $1 \times 1 \times 1$ (1x), $2 \times 2 \times 2$ (2x) and $3 \times 3 \times 3$ (3x) periodic units, solid elements and imposed displacement of 0.1 times the height have been simulated in Abaqus and their homogenised stress vs strain curves compared; the outcome is shown in Figure 4-16.

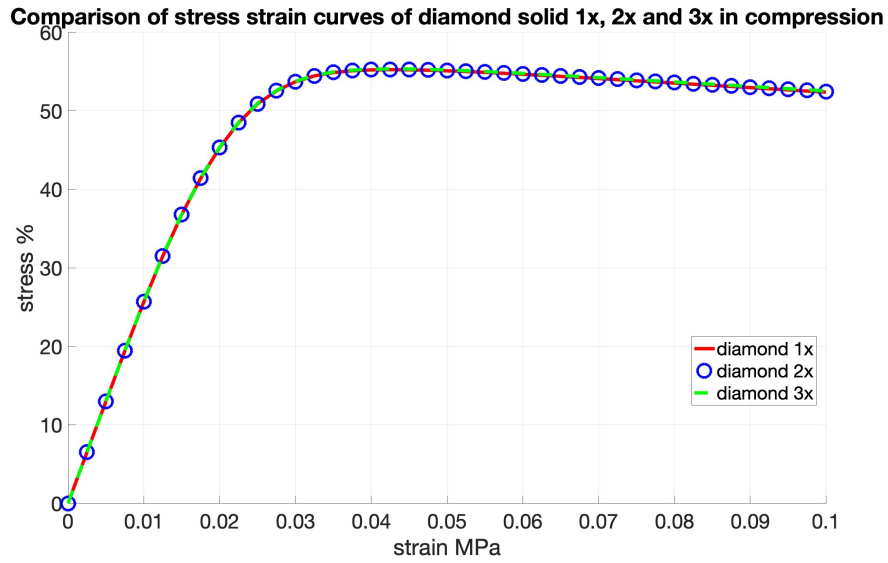


Figure 4-16: Effect of the RVE size on the non-linear part of Diamond homogenised stress vs strain curve

The three curves are perfectly superposed up to the strain of 0.1 (no buckling is expected for higher strains) thus an RVE of one 1x1x1 can be concluded.

A further evidence in favour of this conclusion is provided by the deformed shapes of the three simulations shown in Figure 4-17. As can be visually appreciated, no evidence of buckling is visible.

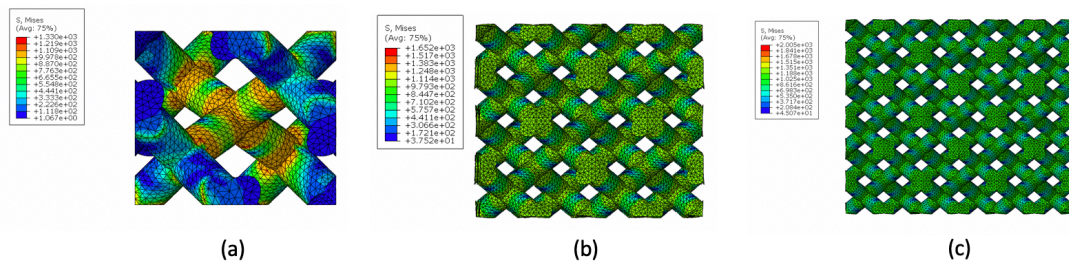


Figure 4-17: Deformed shape of Diamond 1x (a), 2x (b) and 3x (c) periodic

5. Analysis of the real geometry

The compression specimens of each structure have been CT scan and weighted. From the scanning, a stack of images has been obtained in order to reconstruct the real geometries and compare their real pore size and mechanical properties with the ideal ones and with the properties of the real specimens as well as evaluate the real strut dimensions. From the weighting, the real relative density ρ_{real}^* has been estimated. For the computation of the real relative density the contribution of skins has been removed. The chapter will be divided in two parts: the discussion of how the CT scanned images are processed to compute the morphological parameters such as pore size, relative density and strut dimensions at first and, secondly, real TET and Diamond structures have been reconstructed and numerical elasto-plastic simulations have been carried out.

5.1 Real morphological properties

As far as the weighting goes, since it is known that a considerable amount of powder is stuck inside each probe, the weight values which has been selected to obtain ρ_{real}^* are the lowest based on the fact that they are more accurate being associated to specimen containing a smaller amount of residual powder. The values of real relative densities are reported in Table 16 and compared to the ideal ones.

Structure	Real relative density ρ_{real}^*	Ideal relative density ρ^*	Difference %
Diamond	18.6 %	2 %	7
TET	14.5 %	16.6 %	12

Table 16: Real relative density for compression specimens

The file of the CT scan has been opened with myVGL 3.3 and the stack of images exported in PNG format so that they can be read and processed with ImageJ. Once imported in ImageJ, the unit of length has been changed from pixel to mm and the pixel resolution defined equal to the resolution of the CT scan: 0.016 mm for TET and 0.008 mm for Diamond. These two values are not arbitrary but fixed by the resolution of the image acquisition process.

The most important action to carry out in ImageJ is the setting of the threshold, namely the parameter that adjusts the percentage of black and white pixel associated to full material and void. (black pixel = full material, white pixel = void). The threshold has been set in order to achieve the real relative densities of the periodic unit. As a matter of fact, according to the investigation performed on TET ideal specimen, it has been noticed that its relative density is different: 17.5 % for the for the periodic unit and 16.6 % for the specimen. The deviation can be attributed to the extra volume given by the closed struts at the contour, namely the boundary effect. With reference to Table 16, ρ_{real}^* of TET specimen is equal to 14.5 % thus, taking the assumption that said deviation remains identical also for real structures, the target value of ρ_{real}^* for the periodic unit is approximately 13.5 %. No differences can be notified for Diamond for which the relative densities are identical. A sensitivity analysis has been performed setting different values of

thresholds (T is the variable that governs the threshold in ImageJ) and computing the correspondent ρ_{real}^* up to reaching the target. Regarding the measurement of real pore size, four unit cells at different positions (highlighted by the red squares) of the complete sections have been analysed with the Matlab code described in paragraph 2.1 to account for possible deviations; a focus on the selection is visualised in Figure 5-1.

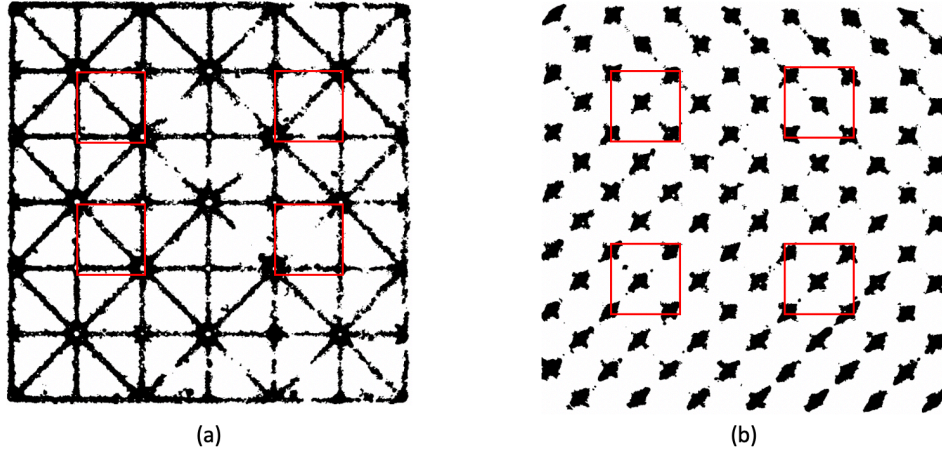


Figure 5-1: Selected unit cells for real pore size computation from the complete section of TET (a) and Diamond (b)

In Figure 5-1, only the first frame of each cubic cell is shown, the number of pictures selected in the out-of-plane direction has been determined in the following way: $4.29/0.016 = 269$ images for TET and $1.55/0.008 = 194$ images for Diamond to be consistent with the pixel resolution and obtain the entire cubic cell.

The results of real pore size and relative density are reported in Table 17. In line with the expectations, real pore sizes are smaller than ideal ones: this is justified by local material agglomerations and roughness of real geometries.

structure	Real pore size p [μm]	p Mean value [μm]	p Standard deviation [μm]	Ideal pore size p [μm]	p difference %
Diamond	$p_1 = 832$	808	27.72	920	12.2 %
	$p_2 = 784$				
	$p_3 = 832$				
	$p_4 = 784$				
TET	$p_1 = 896$	873	15.35	980	10.9 %
	$p_2 = 864$				
	$p_3 = 869$				
	$p_4 = 864$				

Table 17: comparison between ideal and real morphological properties of TET and Diamond RVE

Looking at the tomography of TET, something that can be easily noticed from a qualitative point of view is that d (strut diameter) decreases moving from vertical to horizontal struts passing from inclined ones. The difference is attributed to the printing process and to the fact that the printing angle has been set to 90° (the printing angle is defined as the angle among the building inclination

and the horizontal plane). In line with observations of previous studies like the one of [24], a smaller and smaller intersection between subsequent layers occurs as the printing angle of a strut approaches 0° , the latter being null for horizontal struts with the settled printing angle of 90° . This condition could lead to bad tolerances and excessive local accumulation of melted powder. The overmentioned statements are verified by Figure 5-2 which shows a frontal (a) and an upper (b) view of two TET frames. From the quantitative side, it can be observed that the dimensions of the real vertical struts are homogeneously distributed and with a value of approximately $d_{real} = 0.26$ (lower than the as-designed one of $d = 0.33$).

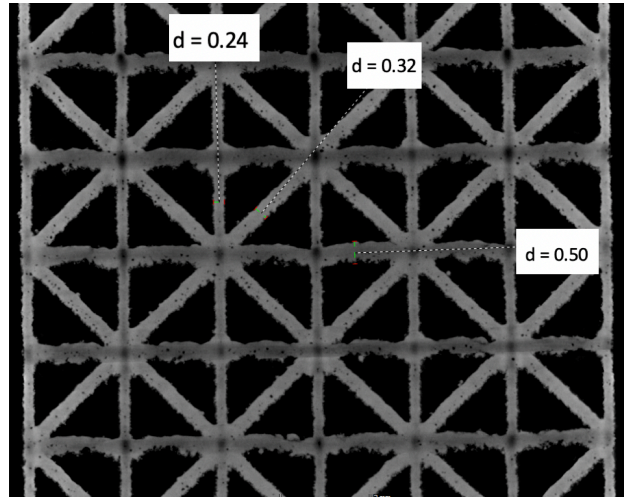


Figure 5-2: Tomography detail of TET compression specimen

Relevant differences between ideal and real values of d have not been observed for Diamond as testified by the strut dimensions measurements shown in Figure 5-3. Whereas TET has horizontal struts which are more problematic from a printing point of view and a higher value of $\lambda = 6.5$, Diamond possess inclined struts and a lower value of $\lambda = 4.69$ and this is, in general terms, better from the manufacturing quality point of view. A future analysis on the relationships between strut dimensions and printing angle is suggested especially for TET to gain more information about the optimal angle able to reduce the geometric tolerances.

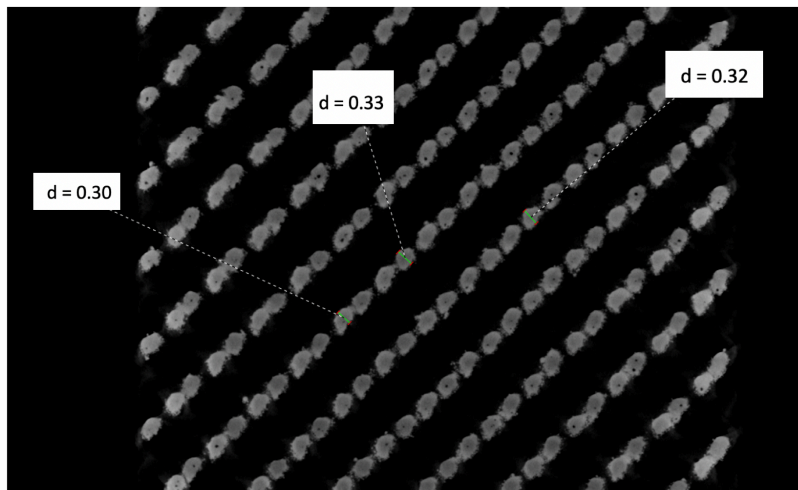


Figure 5-3: Tomography detail of Diamond compression specimen

5.2 Real elasto-plastic mechanical properties

5.2.1 Tetrahedron

Starting from the stack of images processed in ImageJ as described in 5.1, a 2x2x2 TET cell has been extracted to reconstruct the real periodic unit and evaluate the compressive mechanical properties for comparison with experimental tests. To begin, with the 'isosurface' option of the BoneJ plug-in, the STL format of the selected frames has been built; the process is summarised in Figure 5-4.

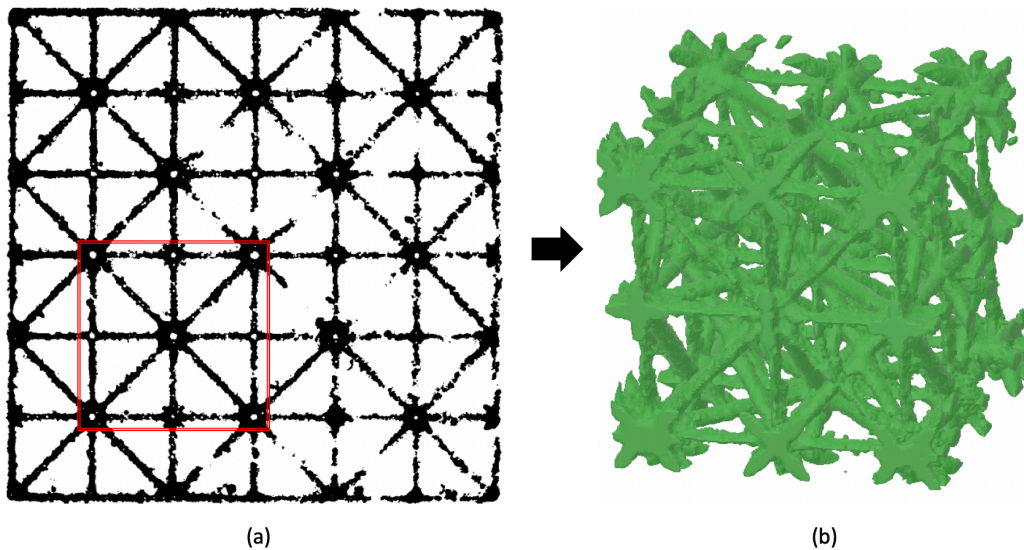


Figure 5-4: From the PNG (a) to the STL (b) of real TET

The STL file is imported into Mimics and, after a series of operations, an INP format of the real RVE is generated for FE modelling. The operations can be summarised as follows:

Application of the mesh (0.085 has been chosen).

Fixing of any geometrical issues like: removal of intersecting and overlapping mesh triangles, removal of noise shells, setting the correct normal orientations, removal of bad contours, bad edges, planar holes and so on.

Rotation of the structure so that it is normal to a x-y-z reference system.

Cutting of extra material so to obtain an RVE delimited by a cube of a specific strut length $L = 4.29$ mm.

The final INP file ready for FE modelling is shown in Figure 5-5. A numerical model involving PBC for symmetric structures has been defined with the aim of evaluating E and σ_y and the homogenised stress vs strain curve has been extracted. A compressive displacement of 5 % has been applied. By implementing this type of PBC and not the ones using Homtools (which is mandatory because no mesh manipulation can be performed on an orphan mesh like the one generated in Mimics), it is known a priori that buckling cannot be predicted by the homogenised stress vs strain curve.

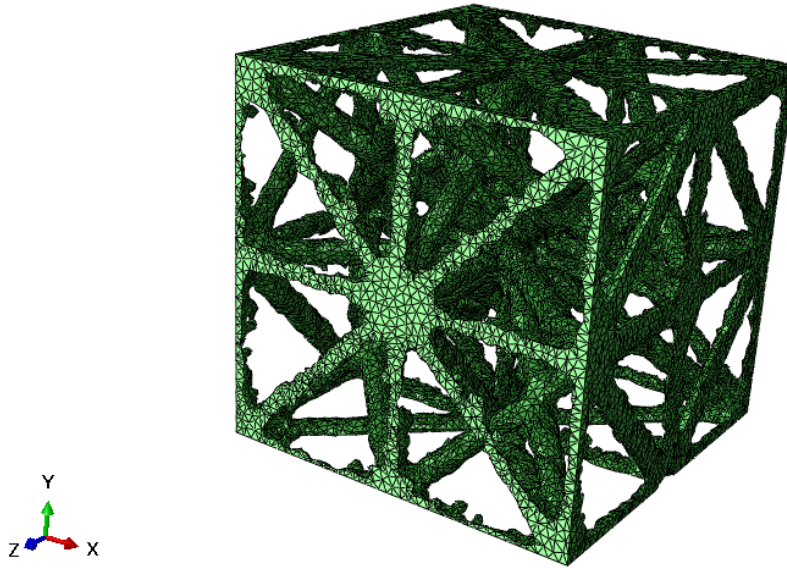


Figure 5-5: Real reconstructed TET 2x2x2 periodic unit

Figure 5-6 shows the comparison between the homogenised stress vs strain curves of real reconstructed cell, compression experimental tests averaged between the two compression specimens, ideal 2x2x2 periodic unit and the 1/8 numerical specimen. The ideal periodic unit stands, by far, above the real curves; this remarkable difference between as-designed and as-built micro-lattice would not be justified by the reduced ρ_{real}^* of 12% respect to ρ^* only, but it is also due to the smaller vertical struts as discussed and shown in paragraph 5.1, this latter effect having the greatest impact on such a wide discrepancy. Moreover, by implementing PBC for symmetric structures and not the ones using Homtools (which is mandatory because no mesh manipulation can be performed on an orphan mesh like the one generated in Mimics), that buckling cannot be predicted by the homogenised stress vs strain curve remaining the latter flat at high strain levels. Apart from this, it is worth noticing that the curve of the compression tests is slightly above the one of the real periodic unit mainly because of the boundary effect which not only interests the linear, but also the non-linear part of the curve. What is more, the boundary effect between real periodic unit and real specimen has been compared to the one between ideal unit and ideal specimen: the result is 7 % vs 13.5 % if Young modulus of compressive tests is considered and 11.5 % vs 13.5 % if Young modulus of tension tests is adopted. It has already been explained in chapter 3 that, because of non-perfect contact between skins and plates in compression, it is better to refer to the Young modulus and yield stress of tension tests. The conclusion is that, being the two boundary effects close to each other, the real reconstructed 2x2x2 cell represents a good prediction for the as-manufactured compression specimens.

A resume of all the results of TET structure are presented in Table 18 where the value of Young modulus out of the real test is the tensile one being the latter more reliable.

	Real periodic unit	Real average compression specimen	Ideal periodic unit	Ideal 1/8 compression specimen
E [MPa]	2355	2693	4198	4840
σ_y [MPa]	17.34	22.51	39.8	44.62

Table 18: Resume of TET results

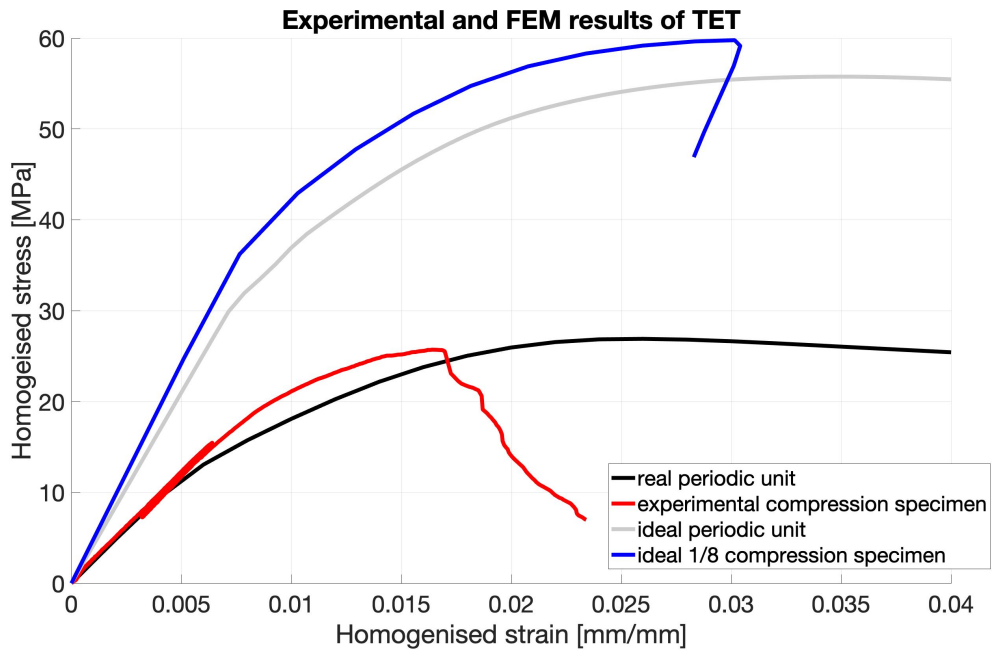


Figure 5-6: Numerical homogenised stress vs strain curve of the reconstructed real TET 2x2x2 RVE compared with compressive tests, ideal 2x2x2 RVE and ideal 1/8 compression specimen

5.2.2 Diamond

For what concerns real Diamond structure, the reconstruction of the periodic unit has not been performed because the mesh which is set in Mimics is an orphan mesh that cannot be modified in Abaqus and, since Diamond needs the application of general PBC with Homtools, a direct modification of the mesh to make it identical for each pair of opposite faces would be needed. An alternative way could be, once again, to develop a Matlab code in communication with Abaqus which redistributes the position of the nodes thus obtaining periodicity. This is suggested as a future development. Anyway, the numerical prediction of the as-manufactured Diamond specimen has been performed by reconstructing a real 7x7x7 reduced specimen (see Figure 5-7). The operations to get the INP file for FE modelling are qualitatively identical to the one already explained for TET and will not be repeated.

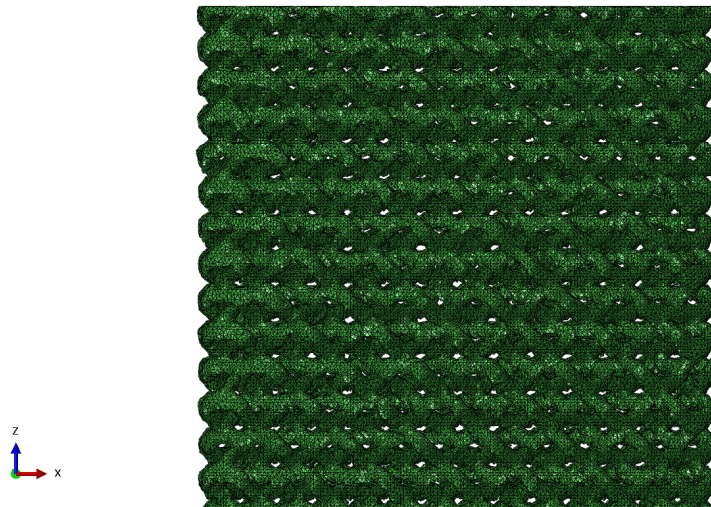


Figure 5-7: Real reconstructed Diamond 'reduced' 7x7x7 specimen

In Figure 5-8 the homogenised stress vs strain curves of 7x7x7 reduced reconstructed specimens, the real compression specimen and the numerical RVE are compared. Values are in Table 19. Once again, the reported value of experimental Young modulus refers to the tensile test since it is more reliable even if the experimental curve of Figure 5-8 is the compressive one.

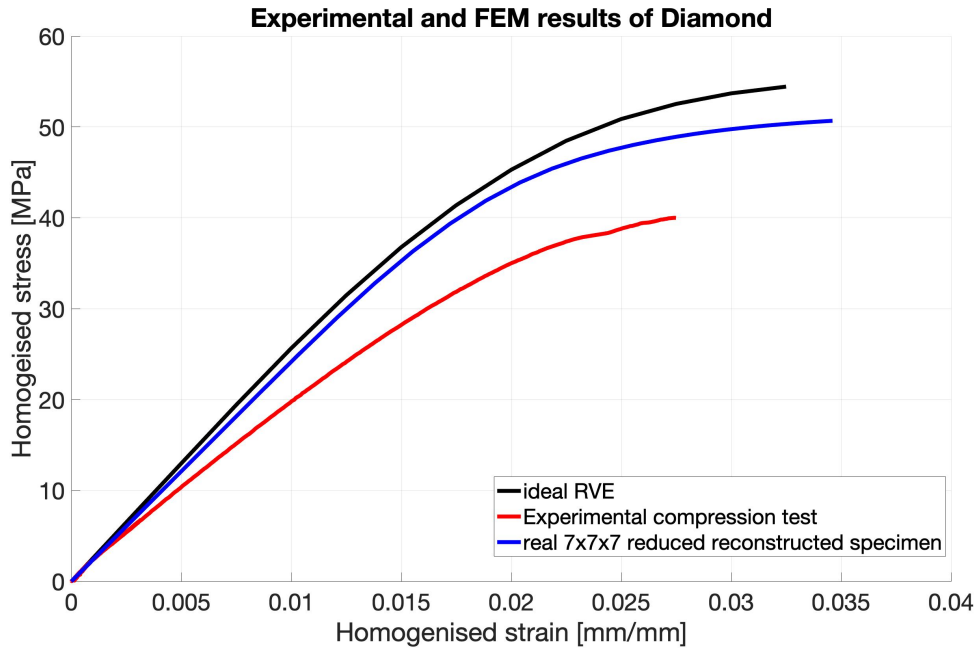


Figure 5-8: Comparison between experimental compression Diamond with RVE and reconstructed 7x7x7 reduced specimen

Based on the outcome of Table 19, a quite wide difference is observed among reconstructed 7x7x7 specimen and experimental compression test. Since the relative density of the reconstructed specimen has been set to be equal to the real weighted one, such a wide deviation might be due to the effect caused by the smaller height (7 vertical cells of the real reconstructed reduced specimen vs 21 vertical cells of the manufactured one) other than measurement dispersion.

	Real average compression specimen	Ideal periodic unit	Reconstructed 7x7x7 specimen
E [MPa]	2216	2565	2380
σ_y [MPa]	33.77	43	43.1

Table 19: Resume of Diamond results

6. Conclusions and future developments

This thesis represented an initial attempt to transfer the knowledge and competences of this research group about the mechanical assessment of micro-lattice structures in the biomedical field for the design of new generation orthopaedic implants which is one of the main current and future applications of lattice structures. The work has been divided in two main parts. In the first part a state of the art of the main features required by lattice in biomedical field has been realized and two promising unit lattice shapes capable of matching the specifications on Young modulus and pores size to avoid stress shielding and promote bone ingrowth and vascularization has been selected, 3D printed, CT scan and experimentally tested in tension and compression. For the computation of pore size, a Matlab code has been developed. In the second part, an experimental and mechanical characterization of the selected structures has been performed and, with respect to the homogenized stress vs strain curves, experimental and numerical real and ideal Young modulus and yield stress have been compared. What is more, the dependency between specimen and RVE elastic modulus as well as the RVE size in linear and non-linear regime have been studied.

The results of the work are resumed, in detail, by the following points:

1. Based on the definition according to which pore size 'p' is the maximum inscribed sphere inside a lattice volume, a Matlab script has been developed. The code is able to return the value of 'p' for any input geometry of any complexity and it is flexible respect to the target resolution one wants to achieve. Thank to this tool, the comparison between ideal and real pore size has been simply performed.
2. To avoid carrying out many different simulations to map the trend between Young modulus and pore size, upon observing that Young modulus and slenderness (λ) of a certain cell geometry are linearly correlated, a non-dimensionalisation has been performed with the parameters $\phi = p/d$ and $\lambda = L/d$ and a liner relation has been assumed. The two variables are able, a priori, to predict numerical Young modulus and pore size of a specific unit cell of defined L and d. It is worth saying that the goodness of linear hypothesis is function of the cell type. (much better form Diamond than TET in this work). Out of this process, design spaces have been created and intersected with areas of biomedical constraints and admissible solutions have been found.

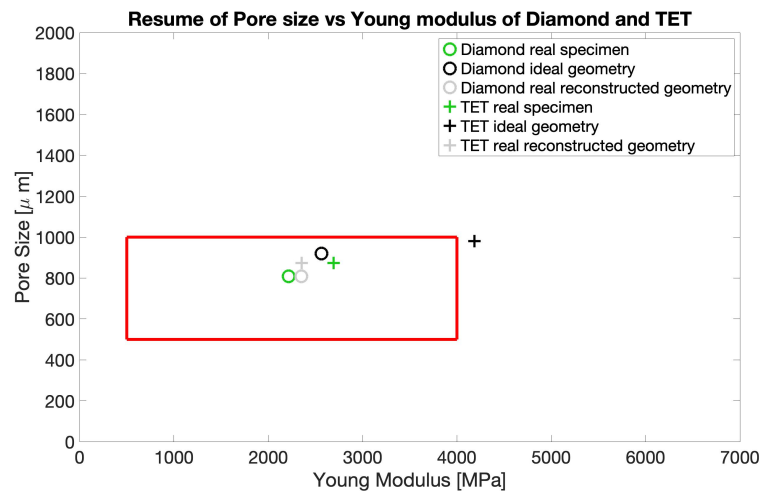


Figure 6-1: Resume of the values of Young modulus and Pore size

3. The comparison between as-designed and as-manufactured Young modulus and pore size has been performed showing that the as-manufactured values still match the biomedical constraints on 'E' (Young modulus) and 'p' (pore size). This is testified by Figure 6-1. A correlation between mechanical properties and relative density has been confirmed: if the former decreases so does the latter and, specifically to TET, a strong contribution of the vertical struts real dimension on Young modulus and yield stress has been observed.
4. The study of suitable PBC to be imposed on a small representative micro-lattice volume to reproduce the infinite medium has been carried out distinguishing those structures whose periodic unit cells are symmetric and those who are not. For the first family, the imposition of planarity of each pair of opposite face is sufficient to gain periodicity, for the second family it is necessary to have a periodic mesh and couple the DOF of every correspondent node on opposite faces; this has been obtained with the Abaqus plug-in Homtools. The two geometries considered, Diamond and TET, belong, by chance, to the two families each. Moreover, the size of the RVE which said PBC are applied to has been investigated either in linear and non-linear regime concluding that it corresponds to one periodic unit in linear regime no matter which the unit cell shape is, and it can be higher than one periodic unit in non-linear regime if buckling occurs. Buckling has been observed both experimentally and numerically for TET and, in non-linear field, the RVE size of Diamond has been concluded to be one, higher than one the RVE of TET.
5. The investigation of the specimen size so that its Young modulus is representative of the infinite homogenized mean simulated with PBC has been carried out and the presence of a residual difference, due to the boundary effect, has been observed. TET still preserves a positive error of 5.3 % (positive means that specimen is stiffer than periodic unit) with a 12x12 periodic units specimen section estimated with beam elements; whereas Diamond features a negative error of 5.7 % (negative means that periodic unit is stiffer than the specimen) with 7x7 periodic specimen section estimated with solid elements. Among the two structures, a lower sensitivity to the boundary effect of Diamond has been assessed.

Out of the state of the art research performed in this thesis, for the micro-lattice design, the focus has been put on two parameters E (Young modulus) and p (Pore size) relevant from a biomedical point of view. Indeed, a further and deeper research about bone properties and crucial implant topological variables is needed to widen the knowledge from the biomedical side. The 3D printing of one of the two structures, namely TET, proved to be not so successful and a big difference between as-designed and as-manufactured mechanical properties has occurred; therefore, a more careful study of the optimal printing angle could improve the struts quality as well as a review on the manufacturability constraints 'd' and ' λ ' is suggested since the settled upper value of $\lambda = 6.5$ is probably too high. As far as the study of mechanical properties goes, fatigue experimental tests and fatigue study in general are needed to estimate the fatigue strength of the micro-lattice specimens that is a relevant for the orthopedic implant design.

In the attempt to define how many periodic units are needed to form the RVE in non-linear regime, a question has been left for TET because of a too high computational cost to increase the model size with solid elements. The use of beams with the opportune imposition of PBC which couples also the rotational DOF will enable to find the size of the RVE. Moreover, for the FE modelling of real reconstructed periodic units of non-symmetric geometries (like Diamond), a solution to manipulate the mesh and make it periodic on each couple of opposite faces still needs to be developed. Finally, the implementation of a numerical damage model for Titanium is suggested to numerically predict ultimate stresses in tension and compression and better study the buckling failure. In literature, with reference to two subsequent works of Ahmadi et al. [25], [26] the Johnson and Cook damage model has been used for Ti6Al4V.

Bibliography

- [1] X. Wang *et al.*, "Topological design and additive manufacturing of porous metals for bone scaffolds and orthopaedic implants: A review," *Biomaterials*, vol. 83, pp. 127–141, 2016.
- [2] X. Z. Zhang, M. Leary, H. P. Tang, T. Song, and M. Qian, "Selective electron beam manufactured Ti-6Al-4V lattice structures for orthopedic implant applications: Current status and outstanding challenges," *Curr. Opin. Solid State Mater. Sci.*, vol. 22, no. 3, pp. 75–99, 2018.
- [3] L. E. Murr, "Open-cellular metal implant design and fabrication for biomechanical compatibility with bone using electron beam melting. Journal of the Mechanical Behavior of Biomedical Materials, 76(Janu," *J. Mech. Behav. Biomed. Mater.*, vol. 76, no. January, pp. 164–177, 2017.
- [4] G. H. Billström, A. W. Blom, S. Larsson, and A. D. Beswick, "Application of scaffolds for bone regeneration strategies: Current trends and future directions," *Injury*, vol. 44, no. SUPPL.1, pp. S28–S33, 2013.
- [5] S. Arabnejad, R. Burnett Johnston, J. A. Pura, B. Singh, M. Tanzer, and D. Pasini, "High-strength porous biomaterials for bone replacement: A strategy to assess the interplay between cell morphology, mechanical properties, bone ingrowth and manufacturing constraints," *Acta Biomater.*, vol. 30, pp. 345–356, 2016.
- [6] M. A. Surmeneva *et al.*, "Fabrication of multiple-layered gradient cellular metal scaffold via electron beam melting for segmental bone reconstruction," *Mater. Des.*, vol. 133, pp. 195–204, 2017.
- [7] F. S. L. Bobbert *et al.*, "Additively manufactured metallic porous biomaterials based on minimal surfaces: A unique combination of topological, mechanical, and mass transport properties," *Acta Biomater.*, vol. 53, pp. 572–584, 2017.
- [8] A. du Plessis, I. Yadroitsava, I. Yadroitsev, S. G. le Roux, and D. C. Blaine, "Numerical comparison of lattice unit cell designs for medical implants by additive manufacturing," *Virtual Phys. Prototyp.*, vol. 13, no. 4, pp. 266–281, 2018.
- [9] H. Dong and M. J. Blunt, "Pore-network extraction from micro-computerized-tomography images," *Phys. Rev. E - Stat. Nonlinear, Soft Matter Phys.*, vol. 80, no. 3, pp. 1–11, 2009.
- [10] E. Onal, J. E. Frith, M. Jurg, X. Wu, and A. Molotnikov, "Mechanical properties and in vitro behavior of additively manufactured and functionally graded Ti6Al4V porous scaffolds," *Metals (Basel)*, vol. 8, no. 4, 2018.
- [11] X. Y. Zhang, G. Fang, and J. Zhou, "Additively manufactured scaffolds for bone tissue engineering and the prediction of their mechanical behavior: A review," *Materials (Basel)*, vol. 10, no. 1, 2017.
- [12] A. du Plessis, I. Yadroitsava, and I. Yadroitsev, "Ti6Al4V lightweight lattice structures manufactured by laser powder bed fusion for load-bearing applications," *Opt. Laser Technol.*, vol. 108, pp. 521–528, 2018.
- [13] C. Maxwell, "Prof . Maxwell on Reciprocal Figures XLV . On Reciprocal Figures and Diagrams of Forces . JBy J . CLERK MAXWELL , F . R . S . , Professor of Natural Philosophy in King ' s College , London ~ . and Diagrams of Forces . On Reciprocal Plane Figures . Definiti," vol. xxv, pp. 250–261.
- [14] S. Drücker, S. Inman, and B. Fiedler, "Simulation and Optimization of the Load Introduction Geometry of Additively Manufactured Lattice Structure Specimens," no. June, pp. 24–28, 2018.
- [15] F. Liu, D. Z. Zhang, P. Zhang, M. Zhao, and S. Jafar, "Mechanical properties of optimized diamond lattice structure for bone scaffolds fabricated via selective laser melting," *Materials (Basel)*, vol. 11, no. 3, 2018.
- [16] S. Amin Yavari *et al.*, "Relationship between unit cell type and porosity and the fatigue behavior of selective laser melted meta-biomaterials," *J. Mech. Behav. Biomed. Mater.*, vol. 43, pp. 91–100, 2015.
- [17] D. Melancon, Z. S. Bagheri, R. B. Johnston, L. Liu, M. Tanzer, and D. Pasini, "Mechanical characterization of structurally porous biomaterials built via additive manufacturing: experiments, predictive models, and design maps for load-bearing bone replacement implants," *Acta Biomater.*, vol. 63, pp. 350–368, 2017.
- [18] A. Vigliotti, V. S. Deshpande, and D. Pasini, "Non linear constitutive models for lattice materials," *J. Mech. Phys. Solids*, vol. 64, no. 1, pp. 44–60, 2014.

- [19] G. Dong, Y. Tang, and Y. F. Zhao, "A 149 Line Homogenization Code for Three-Dimensional Cellular Materials Written in MATLAB," *J. Eng. Mater. Technol. Trans. ASME*, vol. 141, no. 1, pp. 1–11, 2019.
- [20] M. Gavazzoni, L. Boniotti, and S. Foletti, "Influence of specimen size on the mechanical properties of microlattices obtained by selective laser melting," *Proc. Inst. Mech. Eng. Part C J. Mech. Eng. Sci.*, vol. 0, no. 0, p. 095440621986974, 2019.
- [21] A. J. Sterling, B. Torries, N. Shamsaei, S. M. Thompson, and D. W. Seely, "Fatigue behavior and failure mechanisms of direct laser deposited Ti-6Al-4V," *Mater. Sci. Eng. A*, vol. 655, pp. 100–112, 2016.
- [22] S. B. Stéphane Lejeunes, "Une Toolbox Abaqus pour le calcul de propri ´ et ´ es effectives de milieux h ´ et ´ erog ` enes St ´ To cite this version ;," 2011.
- [23] Gvazzoni, "Experimental characterization and modeling of failure of micro-lattice structures obtained by SLM," 2018.
- [24] O. Cansizoglu, O. Harrysson, D. Cormier, H. West, and T. Mahale, "Properties of Ti-6Al-4V non-stochastic lattice structures fabricated via electron beam melting," *Mater. Sci. Eng. A*, vol. 492, no. 1–2, pp. 468–474, 2008.
- [25] J. Kadkhodapour *et al.*, "Failure mechanisms of additively manufactured porous biomaterials: Effects of porosity and type of unit cell," *J. Mech. Behav. Biomed. Mater.*, vol. 50, pp. 180–191, 2015.
- [26] J. Kadkhodapour, H. Montazerian, A. C. Darabi, A. Zargarian, and S. Schmauder, "The relationships between deformation mechanisms and mechanical properties of additively manufactured porous biomaterials," *J. Mech. Behav. Biomed. Mater.*, vol. 70, pp. 28–42, 2017.